

# DISSERTATION

submitted to the  
Combined Faculty of Natural Sciences and Mathematics  
of the Ruperto Carola University Heidelberg, Germany  
for the degree of  
Doctor of Natural Sciences

Presented by  
**Michael Fuchs**  
Born in Waldbröl, Germany

Oral examination: \_\_\_\_\_



**Quantitative approaches towards understanding cell-to-cell  
mobility of the homeodomain transcription factor WUSCHEL  
(WUS) in the *Arabidopsis thaliana* shoot apical meristem**

Referees:

Prof. Dr. Jan Lohmann

Prof. Dr. Thomas Greb



für Vanessa



## Acknowledgements

Zuerst möchte ich mich bei Jan bedanken: Danke, dass du mir diese Reise in deinem Labor ermöglicht hast. Danke, dass du mir die Freiheit gegeben hast meinen eigenen Weg – mit dem einen oder anderen Irrweg – zu finden und einzuschlagen. Danke, dass du mir geholfen hast, trotzdem nicht zu weit abzuschweifen und da warst, wenn der Wald mal wieder zu viele Bäume hatte. Ich hatte in all den Jahren das Gefühl, dass ich mich im Notfall immer auf dich verlassen kann. Danke dafür!

Vielen Dank auch an die Mitglieder meiner TAC: Thomas Greb, Alexander Aulehla und Jochen Wittbrodt. Ich danke euch für konstruktives Feedback und hilfreiche Diskussionen in all den Jahren.

Ebenso gilt mein Dank der Schmeil Stiftung, die mich zum Ende meiner Promotion mit einem Thesis Extension Award finanziell unterstützt hat.

Ich bedanke mich bei allen Personen im COS, die mir in meiner Zeit hier zur Seite gestanden haben. Sei es in wissenschaftlicher Hinsicht, mit tatkräftiger Unterstützung oder auch rein moralisch!

Insbesondere möchte ich hier Joachim danken, der mich schon im Bachelor unter seine Fittiche genommen hat und für einen Großteil meiner ‚wissenschaftlich-frühkindlichen Erziehung‘ verantwortlich war. Danke hierfür, danke für unzählige Stunden inspirierender wissenschaftlicher Diskussionen und ebenso danke für viele Stunden bekloppter Spinnereien beim Mittagessen in der Mensa – zusammen mit Zoran und Alex.

Vielen Dank an dich, Katja, dass du mir in der letzten Phase meiner Doktorarbeit so stark unter die Arme gegriffen hast und dass man sich bei dir so wunderbar auskotzen konnte, wenn die Dinge nicht so gut liefen.

Danke Lukas, dass du mir dein ‚unrolling‘ gezeigt hast und mir geholfen hast, daraus meine eigene Analyse zu entwickeln.

Mein Dank gilt auch all meinen Studentinnen und Studenten und allen HiWis, insbesondere Helena, die mir viel Arbeit abgenommen haben und von denen ich mindestens ebenso viel gelernt habe, wie sie hoffentlich von mir.

Ein besonderer Dank gilt meinen Eltern: Danke, dass ihr mich immer unterstützt habt und mir vermittelt habt, wie wichtig es ist etwas zu finden, das man leidenschaftlich gerne macht. Danke, dass ihr mir ermöglicht habt diesen Weg zu verfolgen!

Zu guter Letzt – aber am Allerwichtigsten – gilt mein Dank dir, Frau Fuchs, formerly known as Frau Schmidt! Danke, dass ich den Großteil meiner Promotionszeit mit dir erleben durfte. Danke, dass ich alle meine Sorgen und Nöte mit dir teilen kann. Danke, dass du immer hinter mir, neben mir und vor mir stehst – je nachdem was gerade nötig ist. Ich freue mich auf alles was noch kommt und darauf auch in Zukunft jeden Weg nur gemeinsam mit dir zu gehen! Ich liebe dich!

## Table of Content

Acknowledgements	7
Table of Content	9
Zusammenfassung	11
Summary	13
<b>1. Introduction</b>	<b>15</b>
1.1. The shoot apical meristem (SAM)	15
1.2. Arabidopsis WUSCHEL (WUS)	16
1.3. The WUSCHEL HOMEODOMAIN (WOX) gene family	18
1.4. Genetic basis of apical stem cell regulation	18
1.5. Integration of environmental stimuli in WUS feedback regulation	21
1.6. WUS protein mobility	22
1.7. Cell-to-cell mobility of plant transcription factors	23
1.8. Aim of this thesis	25
<b>2. Results</b>	<b>27</b>
2.1. Imagine Fancy Name Here (IFNH): An analysis pipeline for quantification of vertical distribution of WUS protein in the shoot meristem	28
2.2. Comparison of different WUS-tagging strategies for wus-mutant rescue lines	36
2.3. Analysis of interdependence between WUS protein mobility and tissue specific cellular environment	43
2.4. Comparison of downwards mobility between the OC and the periphery	52
2.5. The role of conserved protein motifs for WUS mobility	55
2.6. The influence of NLS-tagging on WUS mobility	57
2.7. Linker-Scanning to identify regulatory sequence in the WUS protein	59
2.8. Analysis of proteins conferring the WUS function in other species	61
2.9. Approaches towards deciphering the (temporal) dynamics of WUS mobility	64
<b>3. Discussion</b>	<b>69</b>
3.1. Comparison of differently tagged WUS alleles in wus mutant rescue lines	71
3.2. WUS cell-to-cell movement is an active, bi-directional, WUS-specific process	75
3.3. WUS specificity of active transport might be mediated via the WUS homeodomain	77
3.4. Regulation of WUS mobility via protein retention in the L3	80
3.5. Is WUS mobility CLV3-dependent?	81
3.6. Beyond this thesis: Modelling protein mobility in the SAM based on quantitative data	82

<b>4. Materials and Methods</b>	<b>85</b>
4.1. Molecular Cloning	85
4.1.1 GG entry vector design	85
4.1.2 Creation of an entry vector insert via PCR amplification	86
4.1.3 Creation of an entry vector insert via combination of multiple PCR fragments	86
4.1.4 Purification of DNA fragments from agarose gel	87
4.1.5 Endonuclease digestion of ‘empty’ entry vector (and insert)	88
4.1.6 Purification of DNA from endonuclease digestion reaction	88
4.1.7 Assembly of a ‘filled’ entry vector	88
4.1.8 Creation of an entry vector insert via oligo-annealing, digestion and ligation	89
4.1.9 Transformation of chemically competent E. coli	89
4.1.10 Isolation of plasmid DNA from bacterial culture	90
4.1.11 Validation of cloned entry vector via sequencing	91
4.2. GG destination vector design	91
4.2.1 Assembly of a destination vector via a one-step digestion-ligation reaction	92
4.2.2 Validation of assembled destination vectors via test-digestion	92
4.2.3 Transformation of electrocompetent Agrobacteria	93
4.2.4 Plasmid validation after transformation in Agrobacteria	94
4.3. Genotyping	94
4.3.1 DNA-extraction from plants	94
4.3.2 Genotyping via PCR amplification	95
4.4. Plant Cultivation	96
4.4.1 General growth conditions	96
4.4.2 Plant transformation via floral dip	96
4.4.3 Selection for transgenic plants	97
4.4.4 Basta selection on soil	97
4.4.5 Hygromycin selection on plate	97
4.4.6 Creation of homozygous single-insertion transgenic plant lines	98
4.4.7 WUS rescue assay	98
4.5. Imaging	99
4.5.1 Top-view imaging	99
4.5.2 Side-view imaging	99
4.5.3 Imaging conditions	100
4.6. Data analysis and visualization	100
<b>5. Bibliography</b>	<b>103</b>
<b>6. Appendix</b>	<b>107</b>
6.1. List of figures	107
6.2. List of all entry vectors	111
6.3. List of destination vectors	115

## Zusammenfassung

Die Fähigkeit einer Pflanze, kontinuierlich neue Organe und Gewebe zu generieren wird ermöglicht durch das Vorhandensein pluripotenter Stammzellen innerhalb spezialisierter Stammzellnischen (Meristemen), die die Notwendigkeit für Zellproliferation, aber auch für Zelldifferenzierung, abstimmen und regulieren. Im Sprossapikalmeristem von *Arabidopsis thaliana* ist diese Regulierung der Stammzellpopulation zu einem großen Teil abhängig von der Aktivität des Homeodomänen Transkriptionsfaktors *WUSCHEL* (*WUS*).

*WUS* mRNA wird im Sprossmeristem im sogenannten organisierenden Zentrum, einem Bereich in tiefer liegenden Zellschichten (L3), exprimiert. Von dort bewegt sich das *WUS* Protein mehrere Zellen nach oben, in die Stammzellen innerhalb der darüber liegenden Zellschichten L2 und L1. Auch wenn wir wissen, dass diese Zell-zu-Zell Bewegung, mittels zytoplasmatischer Verbindungen (Plasmodesmata), essentiell für die Funktion von *WUS* und die Aufrechterhaltung der Stammzellpopulation ist, sind der genau Mechanismus und dessen Regulierung, weitgehend ungeklärt oder werden kontrovers diskutiert.

In dieser Arbeit, habe ich quantitative Ansätze zur Charakterisierung der *WUS* Mobilität verfolgt: Hierfür habe ich eine teilautomatisierte Analyse zur Quantifizierung von Fluoreszenzintensität entlang der apikal-basal-Achse des Sprossmeristems, unter Berücksichtigung der Gewebekrümmung, entwickelt. In Kombination mit hochauflösender Fluoreszenzmikroskopie habe ich so die Bewegung unterschiedlicher *WUS* Fusionsproteine im Kontext von Komplementierungslinien und im Wildtyp Hintergrund charakterisiert. Basierend darauf schlage ich vor, dass *WUS* Mobilität eine aktive, nicht-direktionale Komponente beinhaltet, die ihre Spezifität durch die *WUS* Homeodomäne erhält. Meine Daten lassen vermuten, dass dieser Transportmechanismus durch Protein-Protein Interaktionen in der L3 reguliert wird, für die innerhalb des *WUS* Proteins, zusätzlich zu bereits beschriebenen Proteinsequenzen, der N- und C-Terminus wichtig sind.



## Summary

A plant's capacity to continuously generate new organs and tissues is fueled by pluripotent stem cells, embedded in specialized niche tissues, called meristems, which provide strict regulation of stem cell fate to balance the need for cell proliferation and cell differentiation. In the *Arabidopsis* shoot apical meristem (SAM), maintenance of a stable stem cell population largely depends on the non-cell autonomous activity of the homeodomain transcription factor *WUSCHEL* (*WUS*).

*WUS* mRNA is expressed in the organizing center (OC) within the L3 of the shoot meristem. From here, *WUS* protein moves several cell layers upwards towards the overlying L2 and L1 and into the stem cells in the central zone (CZ). While it has been shown that short-ranged cell-to-cell movement of the *WUS* protein, via cytoplasmic bridges called plasmodesmata, is essential for *WUS* function and shoot stem cell maintenance, many aspects of *WUS* mobility, including its mechanism and regulation, remain unclear or under debate.

Here, I chose a quantitative approach to characterize *WUS* mobility: For this, I have developed a semi-automated analysis pipeline for layer-specific quantification of fluorescence intensity along the apical-basal axis of the SAM, taking into account meristem curvature. I have then used this analysis in combination with high-resolution live-cell imaging on dissected, unfixed shoot apices to systematically characterize the mobility of differently tagged *WUS* fusion proteins in complementation lines as well as transcriptionally inactivated mutant alleles in wildtype meristems. From these data, I hypothesize that the mechanism for *WUS* mobility in the SAM involves a component of active transport that is not directional but regulated via protein retention in the L3. Considering previous studies, my data further indicates that specificity of active *WUS* movement may be mediated by the *WUS* homeodomain (HD) and suggests the presence of regulatory sequences not only in the unstructured region between *WUS* HD and *WUS* box, but also at the N- and C-terminus.



## 1. Introduction

Plants retain the life-long capacity to generate new organs and tissues – as part of their regular developmental progress, but also in response to injury and changing environmental conditions. This form of adaptive development, called post-embryonic development, can result in remarkable phenotypic plasticity, even between genetically identical individuals, and allows to compensate for the many disadvantages that follow from a sessile life style. To facilitate continuous growth and development, plants maintain pools of pluripotent stem cells, which divide and differentiate into all necessary cell types. These stem cells are embedded in specialized niche tissues, called meristems, which provide strict regulation of stem cell fate to balance cell proliferation and cell differentiation and, as a result, ensure tissue-level homeostasis.

### 1.1. The shoot apical meristem (SAM)

The shoot apical meristem (SAM) is the apical stem cell niche, located at the very tip of the shoot apex. It contains pluripotent stem cells that directly or indirectly are the source of all aerial tissue – except for the hypocotyl and the cotyledons, which are formed during embryogenesis.

The SAM is a dome shaped structure, consisting of several molecularly and functionally distinct subdomains (Figure 1 A): The epidermal L1 and sub-epidermal L2 are single-cell layers, whose cells usually perform only anticlinal cell divisions, meaning their division planes are oriented perpendicular to the outer surface. The subjacent L3 makes up all inner cells of the plant, which can divide in anticlinal and periclinal direction, that means perpendicular or parallel to the outer surface (Figure 1 B). All three cell layers contain their own stem cells (Satina et al., 1940; Stewart and Burk, 1970), located within the center of each layer, called central zone (CZ), and marked by the expression of the *CLAVATA3* (*CLV3*) gene (Fletcher, 1999). Stem cells in the CZ divide infrequently (Reddy et al., 2004) and upon

division displace their surrounding cells, which are passively pushed to the peripheral zone (PZ), in case of anticlinal cell divisions, or towards the underlying rib meristem, in case of periclinal cell divisions. Cells in the periphery, marked by expression of *CLAVATA3 / ESR-RELATED 40 (CLE40)* (Schlegel et al., 2021), divide more frequently (Reddy et al., 2004), further displacing other cells, and gradually differentiate as their own distance from the center increases, until they are incorporated into organ primordia upon reaching the meristem boundary. Just below the CZ and with slight overlap, is the organizing center (OC), which has been named for the expression of the essential, non-cell-autonomous organizer of stem cell identity *WUSCHEL (WUS)* (Mayer et al., 1998).

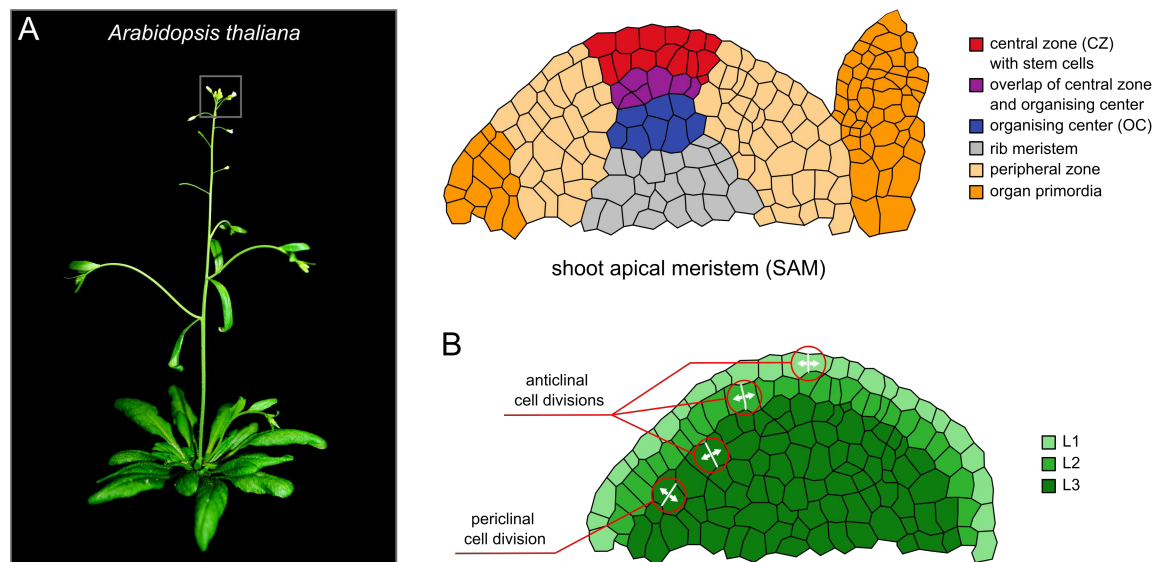


**Figure 1: The shoot apical meristem (SAM) of *Arabidopsis thaliana*.** (Figure modified from my own review article (Fuchs and Lohmann, 2020); original figure concept, design and creation were done by myself.) **(A)** Schematic representation of the shoot apical meristem at the tip of the *Arabidopsis* shoot and of functional domains within the SAM. **(B)** Schematic representation of clonally distinct cell layers in the SAM. L1 and L2 originate from anticlinal cell divisions while cells in the L3 arise from anticlinal and periclinal divisions.

## 1.2. *Arabidopsis WUSCHEL (WUS)*

*WUS* is an essential stem cell maintenance factor, initially described following a forward genetic screen to identify shoot meristem defective mutants in *Arabidopsis thaliana* (Laux et al., 1996). Plants carrying a loss-of-function mutation in the *WUS* gene (*wus* mutant plants) are unable to maintain a functional population of apical stem cells for a prolonged period of time. Instead, stem cells initiate repetitively, but are not protected from

differentiation and get used up in organ formation, leading to meristem termination and arrest of development until a new stem cell population is re-initiated. As a result, *wus* mutant plants display a delayed ‘stop-and-go’ mode of growth and development, with the formation of large, disorganized clusters of rosette leaves, that were inspirational for the mutant name (compare: German ‘wuschelig’ = English ‘disheveled’) (Laux et al., 1996). Inflorescences, once formed, grow similarly disorganized clusters of cauline leaves, while flowers develop only rarely and, lacking reproductive organs except a single, central stamen, are generally infertile (Laux et al., 1996). Interestingly, neither the root meristem nor root development are affected in *wus* mutant plants, underlining the shoot specific function of *WUS* (Laux et al., 1996).

*Arabidopsis WUS* has been mapped to chromosome 2 of the *Arabidopsis* genome. The gene codes for a homeodomain transcription factor with an atypical, 66 amino acid (aa) long homeodomain (HD) (Mayer et al., 1998) with unique structural features that differ from other eukaryotic homeodomains (Sloan et al., 2020; Gehring et al., 1994). The *WUS* protein further contains a stretch of acidic amino acids, implied to be relevant for transcriptional activation (Ptashne, 1988), and an EAR-like domain (Kieffer et al., 2006; Stuurman et al., 2002), which is generally associated with transcriptional repression (Hiratsu et al., 2004; Ohta et al., 2001; Tiwari et al., 2004) and indeed it was found that *WUS* acts as transcriptional activator and transcriptional repressor, depending on the tissue context (Leibfried et al., 2005; Lohmann et al., 2001). Comparison between *WUS* orthologs from different species revealed the presence of another conserved domain, called *WUS* box (Haecker et al., 2004; Stuurman et al., 2002). The *WUS* box has a strong repressive function (Ikeda et al., 2009) and interacts with the co-repressor *TOPLESS* (*TPL*) (Kieffer et al., 2006; Long et al., 2006), however, it is additionally essential for all biological *WUS* functions as the mutation of the *WUS* box (*WUS* $\Delta$ box) renders the protein transcriptionally inactive and

unable to rescue the *wus* mutant phenotype (Ikeda et al., 2009). Additionally, the WUS protein forms homodimers, via sequence stretches in the homeodomain and in the unstructured region between the homeodomain and the WUS box (Busch et al., 2010; Daum et al., 2014; Rodriguez et al., 2016) and interacts with HAIRY MERISTEM (HAM) proteins via a sequence stretch adjacent to the acidic stretch (Zhou et al., 2015).

### 1.3. The *WUSCHEL HOMEobox* (WOX) gene family

The *WUSCHEL HOMEobox* (WOX) gene family, consisting of 14 genes, was identified via sequence similarity search for the *WUS* homeodomain within Arabidopsis genomic data (Haecker et al., 2004). *WOX* genes contain an atypical, 65 aa long homeodomain, which, depending on the individual *WOX* gene, has 38-67% identical and 62-87% similar amino acids, compared to the 66 aa long *WUS* homeodomain, and, similar to the *WUS* HD, is distinctly different from typical (60 aa long) homeodomains (Haecker et al., 2004; Gehring et al., 1994). All *WOX* family members, except for *WOX13*, share the WUS box and three *WOX* genes, *WOX1*, *WOX4* and *WOX5*, also, like *WUS* itself, contain a stretch of acidic amino acids upstream of the WUS box (Haecker et al., 2004).

Interestingly, paralogs of (*Arabidopsis thaliana*) *WOX13*, which is considered to be an ancient, evolutionary basal *WOX* gene, are required for stem cell formation in the moss *Physcomitrella patens* (Sakakibara et al., 2014).

### 1.4. Genetic basis of apical stem cell regulation

*WUS* is a central element of two negative feedback loops, which together robustly define the size of the shoot stem cell domain in all three dimensions.

The *WUS* gene is expressed in the organizing center and *WUS* mRNA is found exclusively in this domain (Mayer et al., 1998) (Figure 2 A, B). *WUS* protein however, moves several cell layers upwards, via plasmodesmata, towards the stem cells in the central zone (Daum et

al., 2014; Yadav et al., 2011) (Figure 2 C, D). Here, it promotes synthesis of the *CLV3* peptide, which is secreted from the stem cells and, via the apoplast, moves towards the subjacent OC, where it is perceived by extracellular receptors, most prominently *CLAVATA1* (*CLV1*), triggering a signaling cascade that leads to downregulation of *WUS* expression (Clark et al., 1995, 1993; Fletcher, 1999; Rojo et al., 2002; Brand et al., 2000; Schoof et al., 2000; Brand et al., 2002). As a result, *WUS* and *CLV3* form a spatially separated negative feedback loop along the apical-basal axis, where high levels of *WUS* result in strong expression of *CLV3*, which in turn decreases *WUS* expression. Lower levels of *WUS* then result in low expression of *CLV3*, which allows *WUS* levels to increase again. Genetic perturbation of this feedback mechanism has strong effects on the stem cell system and thus overall meristem architecture: In *clv* mutants, expression of *WUS* is not limited and the *WUS* expression domain expands upwards and to the sides, resulting in over-proliferation of stem cells and enlarged, fasciated meristems (Brand et al., 2000; Clark et al., 1995; Fletcher, 1999; Schoof et al., 2000). In *wus* mutants, *CLV3* expression fails to initiate in the embryo, but is repeatedly initiated at later developmental stages by the activity of the partially *WUS*-redundant homeodomain transcription factor *SHOOT MERISTEMLESS* (*STM*) (Brand et al., 2002; Lenhard et al., 2002). Overexpression of *WUS* from the *CLV1* promoter on the other hand, which disrupts the spatial separation of *WUS* and *CLV3* expression and at the same time uncouples *WUS* levels from feedback regulation by *CLV3*, leads to similar over-proliferation phenotypes as have been observed for *clv* mutant plants (Schoof et al., 2000). Conversely, strong overexpression of *CLV3* in the shoot meristem, ectopically or from its native promoter, results in loss of *WUS* expression and stem cell termination (Brand et al., 2000; Müller et al., 2006). In summary, the *WUS-CLV3-CLV1* feedback system is geared towards maintaining a small, stable pool of apical stem cells by

constantly balancing the levels of WUS protein to promote proliferation of stem cells while preventing over-proliferation.

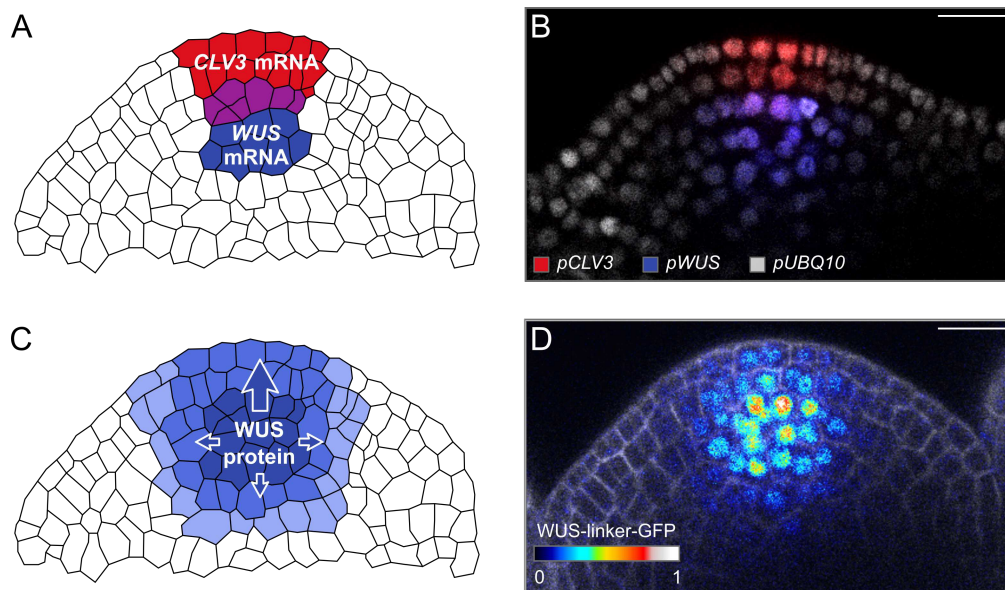


**Figure 2: Localization of key stem cell regulators in the SAM.** (Figure modified from my own review article (Fuchs and Lohmann, 2020); original figure concept, design and creation were done by myself.) (A) Schematic representation of the *CLV3* (red) and *WUS* (blue) mRNA expression domains. Note the overlap in the L3 (purple). (B) Confocal slice through the center of a *pCLV3* (red), *pWUS* (blue) and *pUBQ10* (gray) triple reporter SAM. The scale bar represents a length of 15  $\mu\text{m}$ . (C) Schematic representation of WUS protein localization (intensity coded in blue). (D) Confocal slice through the center of a *pWUS::WUS-linker-GFP* (GD44) rescue SAM. GFP was color coded on a linear scale. The scale bar represents a length of 15  $\mu\text{m}$ .

A recent publication has described another negative feedback loop (Schlegel et al., 2021), involving *CLE40*, a signaling peptide related to the *CLV3* peptide and previously known for its role in the regulation of stem cells in the root apical meristem (Stahl et al., 2013, 2009; Hobe et al., 2003; Berckmans et al., 2020). In the shoot apical meristem, *CLE40* is expressed in the periphery and interacts with its receptor BARELY ANY MERISTEM 1 (BAM1) to promote *WUS* expression via activation of a yet unknown, mobile downstream factor that moves from the periphery to the OC (Schlegel et al., 2021). In turn, WUS protein, which forms a protein gradient along the apical-basal axis in the SAM, from the OC towards the stem cells in the central zone, represses *CLE40*, limiting its expression to the periphery (Schlegel et al., 2021). As a result, *CLE40* signaling integrates information on the size of the

periphery and conveys the demand for new cells to replenish those that have been incorporated into organ primordia.

Laterally, the size of the *CLV3* and *WUS* domains, and therefore the extent of the WUS-*CLV3*-*CLV1* and WUS-*CLE40* feedback systems, is limited by *ERECTA* family signaling via inhibiting expression of *WUS* and *CLV3* in the PZ (Zhang et al., 2021). Similarly, WUS-dependent activation of *CLV3* in the OC, where WUS protein is abundantly present due to the OC being its expression domain, is prevented via the interaction of WUS with HAM proteins, limiting the vertical size of the *CLV3* expression domain (Zhou et al., 2018).

#### 1.5. Integration of environmental stimuli in *WUS* feedback regulation

Besides being a core component of feedback regulation in the SAM, it has become increasingly evident that *WUS* additionally serves as a central integrator for systemic, environmental signaling. A recent examples highlights the regulation of *WUS* activity in response to nitrogen availability in the root (Landrein et al., 2018).

Availability of nutrients in the soil was shown to affect plant growth, shoot development and, more specifically, the size of the shoot apical meristem: Plants grown on soil with nutrient limiting conditions developed smaller meristems than plants grown on non-limiting conditions (Landrein et al., 2018). SAM size correlated with the size of the *WUS* expression domain and the WUS protein domain as well as increased fluorescence intensity of the respective reporters in both cases, indicating higher expression levels. In contrast, for *CLV3* only the domain size, but not fluorescence intensity of a transcriptional reporter, was weakly correlated with meristem size (Landrein et al., 2018). Interestingly, the expression domain and fluorescence intensity of a reporter for cytokinin response (*pTCSn::GFP*) was also increased, indicating higher cytokinin signaling in meristems grown on non-limiting conditions (Landrein et al., 2018). Analysis of cytokinin synthesis mutants confirmed the link between cytokinin signaling, nutrient limiting growth conditions and stem cell

regulation via *WUS*, while grafting experiments showed that cytokinin acts as a long-range signal originating from the root (Landrein et al., 2018). Further experiments with plants grown under nutrient deficiency conditions, but with exogenous supplementation of nitrate, showed that integration of nitrate-responsive cytokinin signaling with shoot development occurred rapidly and was dosage-dependent (Landrein et al., 2018).

### 1.6. WUS protein mobility

While *WUS* function is essential for stem cell maintenance, its expression is limited to the OC and *WUS* mRNA is not found in *CLV3*- positive (stem) cells in L1 and L2 (Mayer et al., 1998). Therefore, *WUS* was suggested to act non-cell autonomously, via the action of an unknown mobile factor (Mayer et al., 1998). The identity of this mobile factor however, remained elusive for another roughly 10 years, until Yadav and colleagues could show that fluorescently tagged *WUS* protein, used to rescue the *wus* mutation in a mutant complementation line, moved from the OC to the CZ, revealing that the *WUS* protein itself facilitates the non-cell autonomous function of the *WUS* gene (Yadav et al., 2011). This finding was later confirmed by another lab using a second fluorescently tagged *wus* rescue line, but more importantly also by using antibody staining for endogenous *WUS* protein in wildtype plants (Daum et al., 2014). Interestingly, Daum and colleagues could additionally show that mobility of the *WUS* protein occurs via plasmodesmata, cytoplasmic bridges connecting neighboring cells in plants, and that this mobility was essential for protein function in stem cells (Daum et al., 2014). For this, they blocked plasmodesmata specifically in the *CLV3* domain, either constitutively or inducibly, using a constitutively active variant of *CALLOSE SYNTHASE 3* (*CalS3m*), which reduces plasmodesmata size via cell wall thickening by callose deposition (Vatén et al., 2011). Constitutive expression of *CalS3m* led to phenotypes reminiscent of the originally described *wus* mutant phenotype, while after inducible expression of *CalS3m* in a rescue line containing fluorescently tagged *WUS*, 8

hours after induction no WUS protein could be observed in L2 and L1 anymore, which in the following led to stem cell depletion and meristem termination (Daum et al., 2014). In the same paper, Daum and colleagues suggested a mobility promoting role of the WUS homeodomain and from their description of the so called MiniMe protein, a super-mobile version of the WUS protein that accumulates massively in L2 and L1, leading to dramatic over-proliferation phenotypes, they concluded the presence of regulatory sequences in the unstructured region between the WUS homeodomain and the WUS box (Daum et al., 2014). In addition, they were able to show that WUS homodimerization was reduced in the MiniMe protein compared to the full length WUS protein, which led them to speculate about dimerization as a potential regulatory mechanism for WUS mobility (Daum et al., 2014). Later studies continued to explore the role of homodimerization for WUS mobility and function (Rodriguez et al., 2016; Perales et al., 2016), but also suggested other potential mechanisms for establishment and maintenance of the WUS protein gradient, including *CLV3*-dependent nuclear-cytoplasmic partitioning and protein destabilization (Plong et al., 2021; Rodriguez et al., 2016; Snipes et al., 2018) as well as protein-protein interactions (Han et al., 2020; Zhou et al., 2018, 2015). However, despite this elaborate body of evidence (for a more detailed discussion, see (Fuchs and Lohmann, 2020)), the exact mechanism behind the formation and maintenance of the WUS L3-to-L1 protein gradient remains elusive, leaving the questions of how WUS mobility from the OC to the CZ is facilitated and, maybe even more importantly, how this process is regulated and integrated with input from environmental stimuli, largely unanswered to date.

### 1.7. Cell-to-cell mobility of plant transcription factors

Proteins that move beyond their mRNA expression domain occur commonly in plants. And while such mobility might not in all cases be necessary for protein function, but instead

might result from passive diffusion through plasmodesmata, a number of proteins have been described whose function relies on short- or long-ranged movement.

For instance, KNOTTED1 (KN1), which is a homeodomain transcription factor like WUS, moves from the L2 to the L1 in the maize shoot meristem (Jackson et al., 1994; Lucas et al., 1995). KN1 cell-to-cell mobility, which occurs via plasmodesmata and requires unfolding of the protein (Kragler et al., 1998), is conserved in Arabidopsis KNOTTED 1-like homeobox (KNOX) proteins, including KNAT1/BREVIPEDICELLUS (BP) and SHOOT MERISTEMLESS (STM). Furthermore, the KN1 homeodomain is both necessary and sufficient for its mobility (Kim et al., 2005). Unfolding and trafficking of KN1 and STM is mediated by physical interaction with the CCT8 subunit of the type II chaperonin complex and cell-to-cell mobility of KN1 (in maize) and STM (in Arabidopsis) is abolished in *cct8* mutants (Xu et al., 2011). Cell-to-cell mobility of WUS, however, is not affected by the same *cct8* mutation, suggesting that the mechanisms for KN1/STM mobility and WUS mobility are not shared (Daum et al., 2014).

SHORT-ROOT (SHR), a transcription factor of the GRAS family, shows cellular trafficking in the Arabidopsis root, moving from stele cells to epidermis cells, initial cells and cells of the quiescent center (Gallagher et al., 2004; Nakajima et al., 2001). SHR mobility is essential for root development and patterning and, similar to KN1/STM, requires its DNA binding domain (GRAS domain) (Gallagher and Benfey, 2009; Nakajima et al., 2001). Additionally, nuclear localization of SHR is necessary but not sufficient for SHR mobility and nuclear trapping of SHR, via interaction with SCARECROW (SCR), has been suggested to negatively regulate SHR mobility (Gallagher et al., 2004; Cui et al., 2007). Therefore, it was proposed that SHR movement is regulated via nuclear-cytoplasmic partitioning, which, interestingly, has similarly been suggested for WUS mobility (Gallagher and Benfey, 2009; Rodriguez et al., 2016). Mobility of the SHR protein was later found to be facilitated by

SHORT-ROOT INTERACTING EMBRYONIC LETHAL (SIEL), which also interacts with TARGET OF MONOPTEROUS 7 (TMO7) (Koizumi et al., 2011). TMO7 is another root mobile transcription factor, showing regulated, unidirectional mobility towards the root tip, which can be influenced by adding additional nuclear localization or nuclear export signals, similarly suggesting a potential role for nuclear-cytoplasmic partitioning in this case. It seems that while cell-to-cell mobility of plant transcription factors represents a reoccurring developmental principle, the mobility of these proteins cannot be traced to one shared universal movement mechanism. Therefore, it remains an interesting question, which mechanistic components might be shared between proteins of different phylogenetic origin, active in different tissues and at different stages of development.

#### 1.8. Aim of this thesis

In this thesis, I aimed to gain a mechanistic understanding of WUS protein mobility and its regulation. Since previous studies, describing conflicting observations and postulating various different mechanisms, have relied on a mostly qualitative analysis of mobility via the visual inspection of few fluorescence images or on simple image quantifications, I instead chose a large-scale, quantitative approach for the layer-specific analysis of (WUS) protein distribution along the apical-basal axis in the shoot meristem, combining high-resolution live-cell imaging of dissected, unfixed shoot meristems with semi-automated image analysis.

First, I have systematically compared different tagging strategies for the WUS protein, regarding rescue efficiency in *wus* complementation lines as well as protein mobility and have found that the two WUS tagging strategies mostly used in the community are both equally suited for the analysis of WUS mobility. I have then used my analysis pipeline to characterize the mobility of various WUS alleles as well as other proteins, expressed from the *WUS* promoter (upwards mobility from the stem cells), but also from the epidermal *MLI*

promoter (downwards mobility). Here, I found evidence for a WUS-specific, partially bi-directional mechanism of active transport. My data further suggested that this transport is regulated via protein retention in the L3 and that specificity might be mediated via the WUS homeodomain. I was further able to identify potential regulatory sequences (for WUS mobility) in the N- and C-terminus of the WUS protein.

## 2. Results

Fluorescent tagging of a protein of interest, especially in combination with live-cell imaging and subsequent quantification of fluorescence signal has become a powerful tool in modern molecular biology. Large scale quantitative analysis, in particular, allows the identification of small differences between samples, hidden within heterogenous populations, that would not be intuitively visible to the human eye. In the shoot apical meristem (SAM), the quantification of functional domains spanning several cells is further complicated by the three-dimensional structure of the tissue itself: a half-sphere, with the central zone (CZ) at its apex and a downwards curvature towards the periphery. As a result, cells, even though they belong to the same clonal layer (L1, L2 or L3), do not necessarily align and, unless every cell is regarded individually, larger functional domains within the tissue, including the protein domain of the stem cell maintenance factor WUSCHEL (WUS), cannot be quantified easily (Figure 3).

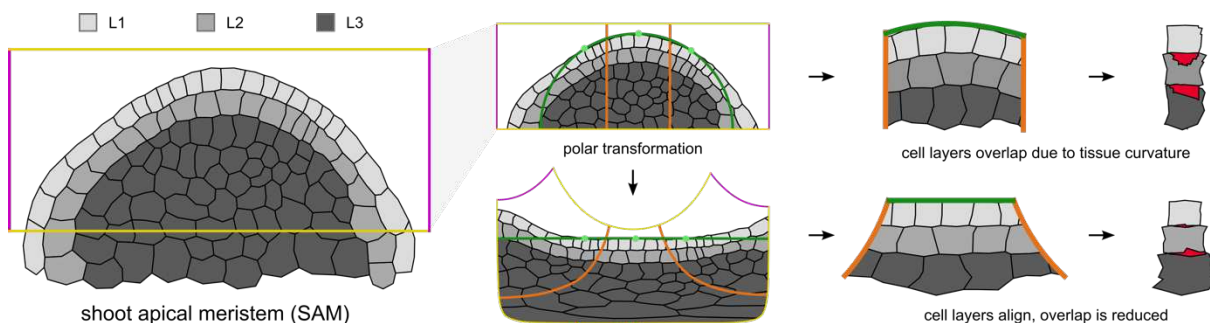


**Figure 3: Tissue curvature of the SAM complicates quantitative analysis.** Schematic representation of the shoot apical meristem (SAM) with distinct cell layers (L1, L2, L3) highlighted. Quantification of fluorescence intensity from micrographs in the SAM is complicated by the overlap between individual cell layers due to tissue curvature. Polar transformation of images, based on circle points recapitulating meristem curvature, can align cell that belong to the same cell layer and reduce overlap.

To overcome this limitation and to reliably quantify the vertical distribution of GFP-tagged WUS protein within upper cell layers in the SAM, I have developed the “Imagine Fancy Name Here” (IFNH) analysis pipeline, which is based on functions within the open-source image analysis platform Fiji (ImageJ version 1.52p) (Schindelin et al., 2012) and is implemented as a Fiji-plugin. In brief, the IFNH tool facilitates fluorescence signal

quantification within a cylindrical column in the meristem center, along its apical-basal axis, via a number of subsequent semi-automated image transformation and dimension reduction steps. Meristem curvature is compensated via individual polar transformations in each image of the z-stack, based on three circle-points per image, and the vertical alignment of all transformed images. As a consequence, cells that belong to the same clonal layer are aligned, signal overlap between adjacent layers is reduced and layer-specific intensity can be quantified (Figure 3).

### 2.1. Imagine Fancy Name Here (IFNH): An analysis pipeline for quantification of vertical distribution of WUS protein in the shoot meristem

The IFNH plugin requires a three-dimensional image stack of the SAM in top-view or side-view perspective (Fuchs and Lohmann, 2022). If the meristem has been imaged from a side-view perspective, the image stack may need to be reoriented correctly before execution of the plugin: with the epidermis and the apex point of the sphere that represents the meristem shape facing upwards and with the rib meristem and inner cell layers of the L3 facing downwards (Figure 4 A). Image stacks for analysis with the IFNH plugin may consist of one channel for measurement of layer specific fluorescence intensity or of two channels, where the second channel is a support channel (with, for instance, DAPI staining or a nuclear reporter) for the identification and assignment of cell layers after polar transformation.

Upon initiation of the IFNH plugin, the ‘Analysis Setup’ menu for specification of the image acquisition parameters of the input image stack and for definition of analysis parameters is opened. Subsequent analysis can use semi-automated, threshold-based assignment of the circle defining the cylindrical analysis domain or manual selection of the circle center-point. The ‘Advanced Options’ menu allows to include additional analysis of a peripheral domain in the shape of a hollow cylinder (donut) around the main analysis domain, only if manual definition of the analysis domain has been selected, and allows further modifications of other

analysis parameters. Following specification of general image analysis parameters, the user is asked to select a save-directory: All data generated during subsequent analysis is saved within a new folder, created at the specified directory and automatically titled according to the input image name. In case, a folder with identical name already exists at the specified directory, the name of the new folder will be automatically extended with ascending numbers.

First, the ‘royal’ lookup table is applied to the input image stack, which is then saved as a ‘.tif’ file. Image stacks containing two channels are split, the individual channels are named as either ‘main-channel’ or ‘support-channel’, according to previous user input, and are saved as separate ‘.tif’ files for subsequent individual processing. Image stacks that have been acquired with the SAM in a native side-view orientation are processed to create a computed top-view stack (using the “TransformJ Turn” plugin (Meijering et al., 2001)), which is required for definition of the analysis domain in the following step.

For semi-automated assignment of the circle defining the cylindrical analysis domain, a threshold is applied to the top-view main-channel image stack and the value of every pixel with an intensity value below the ‘lower threshold’ – defined as a given percentage of the ‘upper threshold’ (which both can be changed in the ‘Advanced Options’ in the initial ‘Analysis Setup’ menu) – is set to zero. To reduce the impact of single bright pixels created by unspecific noise, the image stack is processed with a 3D median filter (whose radius is set to 1.0 by default, but can also be modified in the ‘Advanced Options’ in the initial ‘Analysis Setup’ menu) and is then subjected to maximum intensity projection followed by another thresholding. This allows the use of the built-in Fiji ‘Analyze Particles’ plugin to extract regions of interest (ROIs), from which the user is then asked to select one or multiple ROIs, best representing the whole domain of interest. If the ROIs extracted seem insufficient to describe the whole domain of interest, the process of automated domain identification can

be repeated by selecting 'Threshold' and entering a new percentage for the 'lower threshold' (setting the percentage for the 'lower threshold' at a smaller value will make the thresholding less stringent, resulting in potentially larger ROIs; increasing the percentage will make the thresholding more stringent, resulting in potentially smaller ROIs). Selected ROIs are combined into a singular ROI, the geometric center (centroid) of this ROI is calculated and will serve as the center-point for the circle defining the cylindrical domain of interest in subsequent analysis.

For manual definition of the circle center-point, the top-view main-channel image stack is subjected to maximum intensity projection. The user is then asked to select the circle center-point by clicking at a position within the maximum projection image canvas.

In both cases, a circular ROI (whose diameter can be modified in the 'Advanced Options' in the initial 'Analysis Setup' menu) is defined around the center-point and temporarily saved in the ROI manager for future reference. This ROI represents the XY-dimensions of the cylindrical analysis domain. If peripheral analysis has been enabled during initial setup, an additional circular ROI, based on the same center-point but with a larger radius, is defined and saved. The combination of both ROIs specifies a donut shape (the width of which can be modified in the 'Advanced Options' in the initial 'Analysis Setup' menu), which represents the XY-dimensions of the hollow cylinder that is the peripheral analysis domain. The center-point, the XY-dimensions of the analysis domain as well as the peripheral analysis domain, if applicable, are drawn in a maximum intensity projection of the main-channel top-view image stack and the image is saved for visualization purposes (Figure 4 B).

Subsequent analysis of the vertical distribution of fluorescence intensity takes place only within the analysis domain (and the peripheral domain), that is the three-dimensional column(s) defined by the previously determined ROI(s). Therefore, the top-view main-

channel image stack is duplicated and all pixels outside the analysis domain ROI are set to a pixel value of zero. If peripheral analysis has been enabled, similarly all pixels outside the peripheral domain ROI as well as all pixels within the analysis domain ROI are set to zero in a second duplicate of the top-view stack. If the original image stack has been a two-channel image, containing a secondary support-channel for the assignment of cell layers, duplicate(s) of the top-view support-channel image stack are treated the same way as the corresponding main-channel counterpart. All modified stacks are then rotated and processed to create side-view image stacks, whose depth corresponds with the diameter of the peripheral domain ROI or with the diameter of the analysis domain ROI, if peripheral analysis is not enabled.

The alignment of cells of the same cell layer, compensating for the tissue curvature of the meristem, is accomplished by subjecting the image stack to a polar transformation. For this, the center-point of the circle that best describes the surface of the SAM, within each slide, is chosen as the reference point of the polar coordinate system. Each such circle is specified by three circle-points, manually selected by the user within each image canvas. Definition of circle-points takes place in a side-view image stack which is identical in stack size (depth) with the previously modified image stacks, but still contains all pixels outside the domain(s) of interest in XY-dimension to allow for a better assessment of the curvature of the whole meristem. If the original stack has been a two-channel image, circle-point definition is done in the support-channel rather than the main-channel. A circle-point is defined when the status of the left mouse button is registered as 'pressed', either through a regular 'mouse click' or by holding down the mouse button, within the image canvas of the circle-point selection window. A retention time between selection of successive points, the circle point selection delay (the duration of which can be modified in the 'Advanced Options' in the initial 'Analysis Setup' menu), allows for adjusting the position of the cursor even when selecting

circle-points by pressing the mouse button continuously. For user convenience, the three circle-points necessary within each single slide of the stack are not defined in direct succession. Instead, after selection of one circle-point (e.g., the leftmost point) within a slide, the stack progresses to the consecutive slide, allowing the user to select circle-point(s) with minimal mouse movement. When all corresponding points (e.g., all leftmost points) have been defined in the whole stack, the starting slide is selected again and the user is asked to define the next array of points (e.g., all center-points). Point coordinates are saved and the circle points are drawn in the (circle-point definition) side-view image stack, which is saved for visualization purposes (Figure 4 C).

Circle-points are used to calculate the center-point of the corresponding circle within each individual slide. All pixels below the horizontal line through the center point, which would result in unspecific artifacts after polar transformation, are deleted within all previously modified side-view image stacks. Likewise, all pixels above the horizontal line through the point ten pixels above the highest circle-point are deleted as well, to reduce the impact of unspecific noise or out-of-focus light. The resulting image stacks are saved with the affix ‘\_not-unrolled’ (Figure 4 D).

From this point on, the analysis workflow between the main analysis domain and the peripheral domain is identical. If peripheral analysis has been enabled, subsequent analysis is simply repeated for the periphery and all files are saved with the additional affix ‘\_periphery’. For simplicity and brevity of description, I will from now on assume that peripheral analysis has not been enabled.

Modified side-view image stacks, both main-channel and support-channel, if present, are subjected to polar transformation (Figure 4 E): For every pixel with an intensity value other than zero in the ‘\_not-unrolled’ image stack, a new position is calculated, using the previously determined center-points within each individual slide as the pole (reference point

of the polar coordinate system). The pixel corresponding to this position within an empty (all pixel values equal zero) stack, the smallest necessary size of which is automatically calculated, is then set to the intensity value of the ‘transformed’ pixel. As a result, information on absolute distance within the tissue is lost, as the meristem gets compressed at the surface and is pulled apart in deeper layers, even introducing gaps between pixels, but tissue curvature is compensated for and cells of the same cell layer align in XY-dimension as well as in Z-direction. In case two pixels from the original ‘\_not-unrolled’ image are calculated to occupy the same position after polar transformation, the pixel at the corresponding position in the empty stack is set to the sum of both pixel values, preserving all information on total signal intensity.

Transformed image stacks (containing X-, Y-, Z-axes), both main-channel and support-channel, if present, are processed to create sum-intensity-projections (XY) (Figure 4 F), effectively reducing image dimensions from 3D to 2D. These planar projections are then turned by 90 degrees around their Y-axis and the resulting image stacks (YZ), which have a width of only one pixel, are processed to create sum-intensity-projections (Y) again, condensing all information on signal intensity from the (analysis domain column in the) original stack within a single line (Figure 4 G). All three image types, the transformed image stacks (3D), the planar projection images (2D) as well as the linear projection images (1D), are saved.

Intensity values are extracted from the linear projection image and are temporarily saved in an array, to be plotted in a line plot (Figure 4 G): From left to right, this line plot depicts the fluorescence intensity within the three-dimensional cylindrical column defined by the circular analysis domain, from the surface going into the tissue, along the apical-basal axis of the shoot apical meristem. Graphical representation of fluorescence is crucial, since the identification of the different cell layers and the assignment of borders between nuclei, is

performed based on the line plot and via manual user selection. For protein fusions that are strongly nuclear localized, including non-mutated, tagged WUS variants, this can be done in the main-channel line plot. In general, however, the use of a support-channel with a nuclear reporter or a cell wall staining is highly recommended.

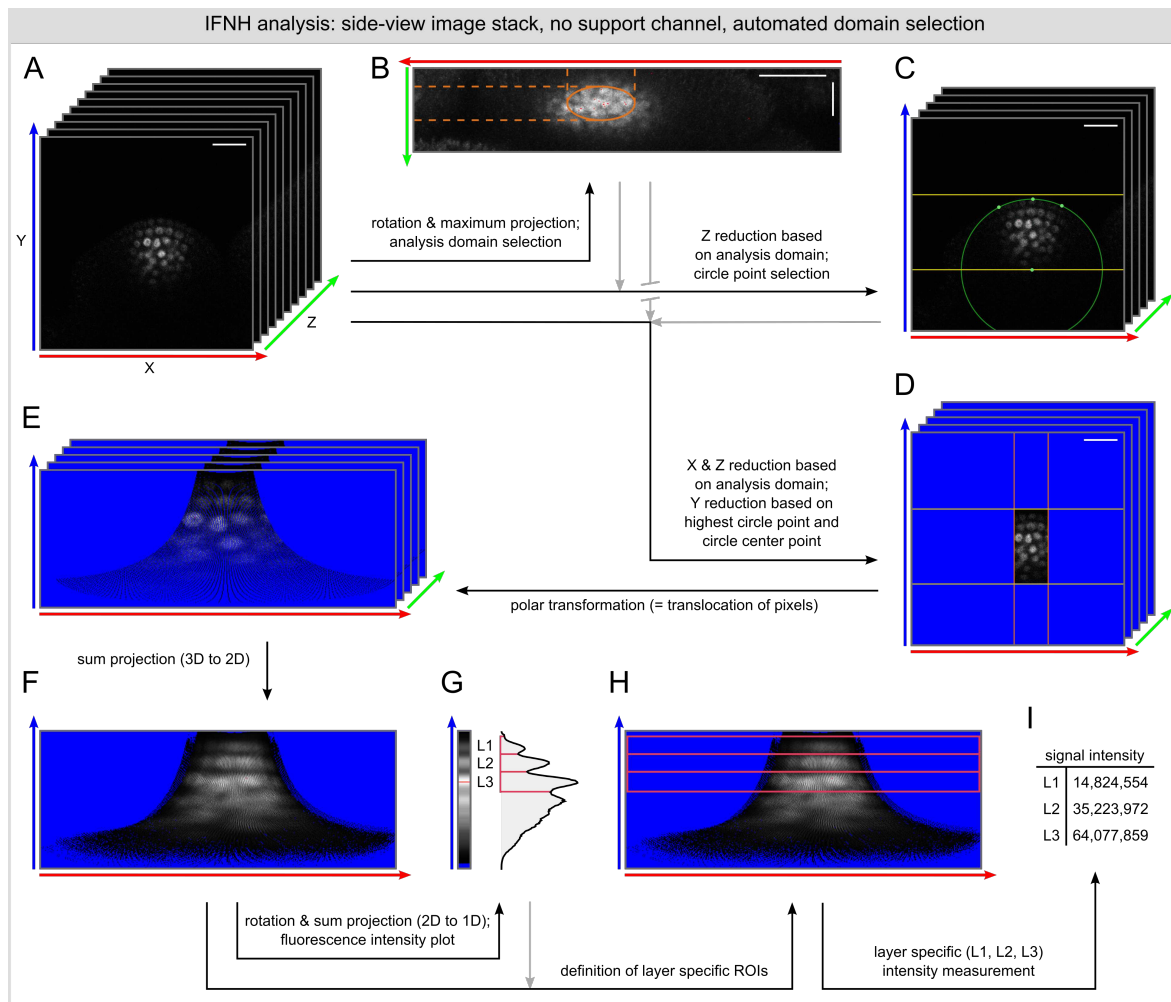


**Figure 4: The IFNH tool performs semi-automated alignment of meristematic cell layers, followed by layer specific intensity measurement.** Images in this workflow example are real data: The meristem depicted was imaged from a side-view perspective, did not contain a nuclear support channel and automated, threshold-based selection of the analysis domain was used. Horizontal and vertical scale bars represent a length of 15  $\mu\text{m}$ . All images use the ‘HiLo’ LUT, where blue color represents pixels with a value of zero. **(A)** Image stack of a SAM, imaged from a side-view perspective, with the curved outer surface of the meristem oriented upwards. **(B)** Maximum projection of (A) after rotation of the stack. This image is used for automated, threshold-based selection of the analysis domain. **(C)** Side-view image stack with reduced stack depth (Z-dimension), based on (B) to encompass only the analysis domain. This image stack is used for the selection of circle points later used for polar transformation. **(D)** Side-view image stack with reduced stack depth (Z-dimension), based on (B). Additionally, pixels outside the analysis domain in X-dimension, based on (B) have been set to 0. Y-dimension has been reduced by setting pixels to 0, based on circle points and the circle center point (C). **(E)** Side-view image stack, based on (D) after polar transformation using the center point of the circle defined in (C) as a pole. **(F)** Sum projection of (E). This image contains all information on signal intensity from (D) and (E), but represents a reduction from 3D to 2D. **(G)** 1D representation of (F) after rotation and sum projection. All information on signal intensity (within a specified analysis domain, along the apical-basal axis of the SAM) has been compressed from 3D to 1D and can be plotted in a line plot. The line plot is then used to define the borders between adjacent cell layers. **(H)** 2D representation, equivalent to (E), containing layer specific ROIs for intensity measurement, based on (G). **(I)** Layer specific intensity (for L1, L2, L3) within a specific analysis domain. Fluorescence intensity was measure in (H), based on the borders defined in (G).

For the identification of cell layers, the user is first asked to define the ‘border between L1 and L2’ by clicking at the respective point within the line plot image canvas. If the signal depicted in the line plot originates from a nuclear reporter, this is signified by the first local minimum from the left. If the signal depicted in the line plot originates from a cell wall staining or similar, the L1-L2 border is signified by the second local maximum from the left. Successively, the user is asked to define the ‘border between L2 and L3’ as well as the ‘right border of the first cell layer of L3’, while the left border of the L1 is selected automatically by being set to the same width as the L2. Vertical lines are drawn through the selected border points for visualization purposes and the line plot is saved as an image file. If the original image has contained a support-channel, both line plots, of the main-channel and the support-channel, are combined and saved in the same image. Additionally, all data of the line plots, including the information which data points have been selected as border points, are saved within a ‘.csv’ file.

Once, the first three monolayers in the SAM have been identified and the borders between them assigned, measurement of layer-specific fluorescence intensity is performed within the planar projection (‘\_unrolled-2D’) of the main-channel. To this end, a rectangular ROI, with its height defined by the previously selected border points and its width covering the full width of the image, is created for each cell layer. Total signal intensity within each ROI is measured, the ROIs are saved for later reference and a duplicate of the planar projection with the ROIs drawn into is saved for visualization purposes (Figure 4 H).

From the fluorescence intensities within the three cell layers (L1, L2, L3) (Figure 4 I), the percental distribution of signal across these layers as well as layer-to-layer ratios are calculated. The percental distribution allows for a quick, intuitive overview of protein distribution within the upper meristematic layers, while layer ratios are especially suited to assess mobility between individual (adjacent) cell layers. Both methods allow for large-scale

comparison of individual plants with the same genetic background as well as different lines carrying the same fusion protein, regardless of expression strength and laser-power applied during image acquisition. All data on total intensity, the percental distribution and the layer-to-layer ratios are saved in a '.csv' file.

Finally, the line plot image, including the main-channel plot as well as the support-channel plot, if applicable, and the selected border points, is opened again for a final visual inspection by the user. All images are closed and execution of the plugin is ended upon user input.

### 2.2. Comparison of different WUS-tagging strategies for *wus*-mutant rescue lines

WUS is a non-cell autonomous regulator of stem cell maintenance (Mayer et al., 1998). In this capacity, WUS protein moves, via plasmodesmata, from the organizing center (OC) in the L3 towards the stem cells in the L1 (Yadav et al., 2011; Daum et al., 2014). Since its initial characterization as a mobile protein, different tagged variants, following slightly different design principles, have been used to study WUS *in-vivo* behavior and protein distribution. Most prominently, these include WUS tagged with green fluorescent protein (GFP) at its N-terminus (GFP-WUS) under the control of a 5.6 kb promoter fragment and 1.2 kb terminator fragment (Yadav et al., 2011) and WUS tagged with a flexible serine-glycine linker and GFP at its C-terminus (WUS-linker-GFP) under the control of a 4.4 kb promoter fragment and 2.8 kb terminator fragment (Daum et al., 2014). While both WUS-tagging strategies have initially resulted in qualitatively similar descriptions of WUS distribution (Yadav et al., 2011; Daum et al., 2014), later studies showed contradictory results using either N- or C-terminal WUS fusions and mostly visual analysis of WUS distribution (Daum et al., 2014; Rodriguez et al., 2016; Snipes et al., 2018; Plong et al., 2021). However, to date, no systematic comparison of the influence of different WUS-tagging strategies on *in-vivo* protein distribution or mutant rescue efficiency has been performed.

To address this, I created four different *wus*-rescue constructs carrying WUS tagged with GFP at its N- or C-terminus, with or without the addition of a flexible serine-glycine linker (Figure 5). I used the same 4.4 kb and 2.8 kb fragments of the endogenous *WUS* promoter and terminator, respectively, that have been published previously (Daum et al., 2014), but used the GreenGate cloning system (Lampropoulos et al., 2013), which causes only minimal cloning scars in vector assembly, instead of the Gateway system. I then transformed these constructs in heterozygous *wus*-mutant plants and established single-insertion, homozygous *wus*-complementation lines in a homozygous *wus*-mutant background (pMF111: GFP-WUS; pMF112: WUS-GFP; pMF113: GFP-linker-WUS; pMF114: WUS-linker-GFP) for comparison with a previously published rescue line employing a C-terminal fusion with a flexible linker (GD44: WUS-linker-GFP (Daum et al., 2014)). The comparison with a previously published *wus*-rescue line using an N-terminal fusion without a linker (GFP-WUS (Yadav et al., 2011)) was not possible, since the line has not been made available to our lab by the authors of the original study.

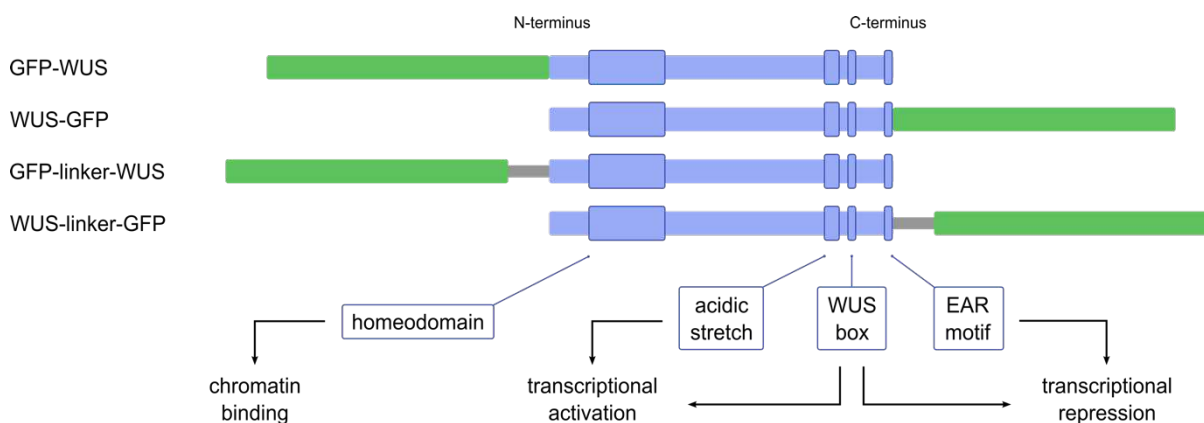


**Figure 5: Different tagging strategies for WUSCHEL (WUS).** Schematic representation of the different tagging strategies for WUS, tested in this thesis. WUS was tagged with green fluorescent protein (GFP) at the N-terminus or C-terminus, with and without the addition of a flexible serine-glycine linker. Known protein domains important for WUS transcriptional activity, their relative position in the WUS protein and their main function are highlighted.

To characterize *in-vivo* distribution of WUS, all *wus*-complementation lines were analyzed using confocal live-cell imaging on dissected shoot apices, as we have described previously (Fuchs and Lohmann, 2022). Image stacks were acquired from a native side-view

## Results

perspective, that is perpendicular to the apical-basal axis of the meristem, to increase spatio-temporal resolution within the plane of WUS movement. Visual analysis confirmed the presence of fluorescently tagged WUS protein in all newly created rescue lines. The distribution of WUS protein closely resembled the distribution of tagged WUS protein described in earlier studies (Yadav et al., 2011; Daum et al., 2014) as well as the distribution of untagged, endogenous WUS protein (Daum et al., 2014): with the majority of protein present in the OC, where *WUS* is expressed, a decreasing protein gradient from the L3 to the L1, and predominantly nuclear localization of the WUS fusion protein (Figure 6). All lines, containing differently tagged WUS variants, appeared highly similar, except for pMF113 (GFP-linker-WUS), which was less nuclear and showed an increased relative amount of fusion protein in L2 and L1, compared to the other rescue lines.

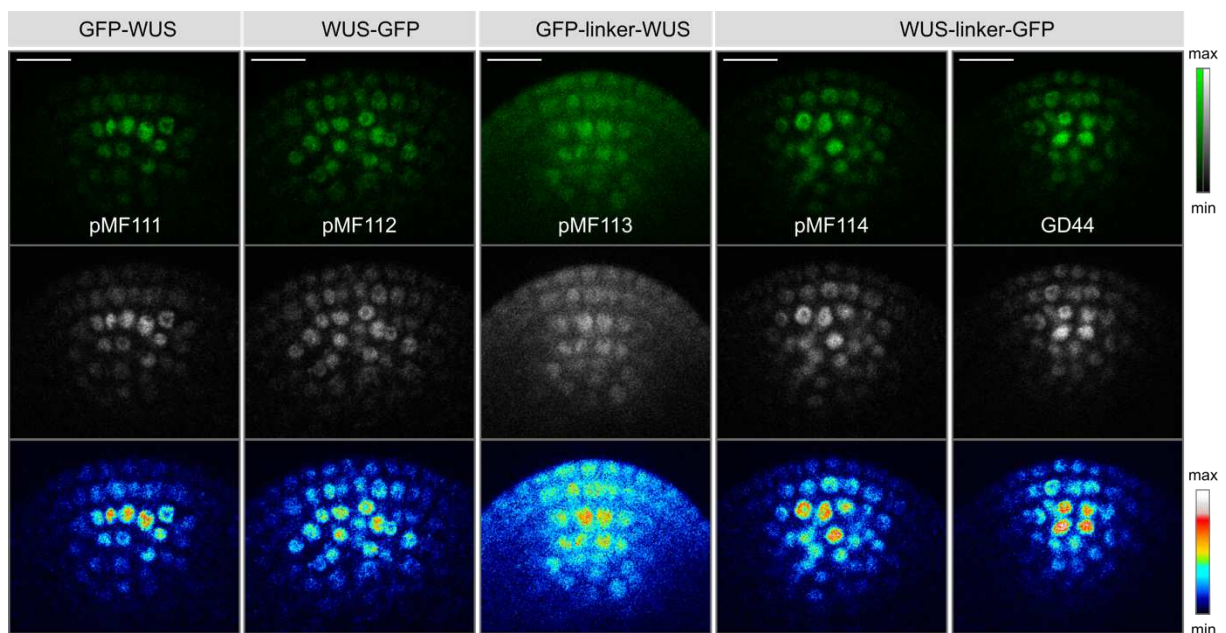


**Figure 6: Live-cell imaging of *WUS* rescue lines to compare different *WUS* tagging strategies.** Micrographs of single-insertion homozygous *WUS* rescue lines (T3 or higher). Images have been acquired from a side-view perspective to increase imaging resolution along the apical-basal axis. Scale bars are valid in horizontal and vertical dimension and represent a length of 15  $\mu\text{m}$ .

To characterize the vertical distribution of WUS protein in detail, I analyzed all imaging data using the IFNH analysis pipeline and quantified the vertical distribution of fluorescent signal within a cylindrical column of 20  $\mu\text{m}$ , along the apical-basal axis within the center of the

SAM. I focused my analysis on the direct comparison of adjacent cell layers by calculating layer specific fluorescence intensity ratios. This allowed me to compare individual plants with the same genetic background, but also plants originating from different transgenic lines, while minimizing potential effects of expression strength of the transgene as well as the specific imaging conditions. For the *WUS* promoter, which is expressed in the OC (L3 and below), I analyzed the L2/L3 ratio and the L1/L2 ratio: A low L2/L3 ratio, with a value lesser than one ( $<1$ ), indicated that the amount of (fluorescent) fusion protein in the L2 was lower than in the L3; a high L2/L3 ratio, with a value larger than one ( $>1$ ), indicated the reverse, while a L2/L3 ratio of exactly one ( $=1$ ) would suggest that the amount of protein in the L2 was the same as in the L3. Similarly, a L1/L2 ratio smaller than one ( $<1$ ), indicated that the amount of fusion protein in the L1 was lower than in the L2; a L1/L2 ratio larger than one ( $>1$ ) indicated the reverse, while a L1/L2 ratio of one ( $=1$ ) would suggest that the amount of protein in the L1 was the same as in the L2. Relative differences in layer ratios, that is relative differences in protein amount for adjacent cell layers, between individual plants but also between plant populations representing different lines, were regarded as a measure for the capacity of the fusion protein to move from one cell layer to the next.

Interestingly, even though all *wus*-complementation lines were stable homozygous single-insertion lines ( $> T3$  generation), variability in layer ratios, which was high in general, was higher for the L2/L3 ratio than for the L1/L2 ratio. I could, however, not observe qualitative differences in variability between the different lines. Of all rescue lines, pMF114 (WUS-linker-GFP) showed the lowest L2/L3 ratio (L2/L3 median ratio 0.634,  $n = 24$ ), followed by GD44 (WUS-linker-GFP) (L2/L3 median ratio 0.716,  $n = 23$ ), pMF111 (GFP-WUS) (L2/L3 median ratio 0.746,  $n = 22$ ), pMF112 (WUS-GFP) (L2/L3 median ratio 0.760,  $n = 20$ ) and pMF113 (GFP-linker-WUS) with the highest ratio (L2/L3 median ratio 0.829,  $n = 22$ ). Differences between lines were not statistically significant, according to the results of an

## Results

ANOVA-TukeyHSD test (significance value = 0.01), except for the direct comparison of pMF114 (WUS-linker-GFP) and pMF113 (GFP-linker-WUS). For the L1/L2 ratio, I observed the lowest ratio for pMF111 (GFP-WUS) (L1/L2 median ratio 0.434, n = 22), followed by pMF114 (WUS-linker-GFP) (L1/L2 median ratio 0.464, n = 24), which was not significantly different from pMF111. GD44 (WUS-linker-GFP) (L1/L2 median ratio 0.491, n = 23) and pMF112 (WUS-GFP) (L1/L2 median ratio 0.493, n = 20) were not significantly different from each other as well as from pMF114, but were different from pMF111. pMF113 (GFP-linker-WUS), again, showed the highest ratio (L1/L2 median ratio 0.539, n = 22), suggesting increased protein mobility, and was also statistically different from all other rescue lines (Figure 7).

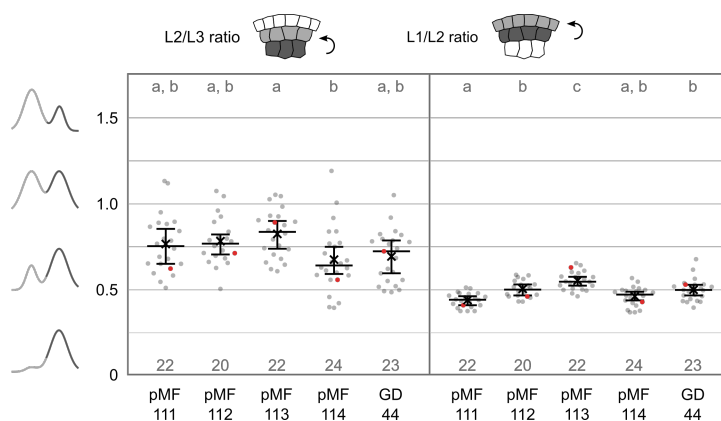


**Figure 7: Quantitative analysis of vertical protein distribution of fluorescently tagged WUS protein in WUS rescue lines.** Vertical distribution in the SAM is displayed as the ratio between L2 and L3, signifying mobility from L3 to L2, and as the ratio between L1 and L2, signifying mobility from L2 to L1. Individual data points represent individual plants. The red data points represent the individuals shown in Figure 6. The median of each population is indicated by a black bar, together with the 95% confidence interval. The mean of each population is indicated by a black X. The sample size is indicated in gray numbers below each population. The results of an ANOVA-Tukey HSD statistical test (significance value = 0.01; same letters indicate no statistically significant difference) are shown above each population.

Having identified small differences in vertical distribution of the different fusion proteins, I wondered whether these changes would have functional relevance and performed a more detailed phenotypic analysis. In Arabidopsis, homozygous *wus* mutant plants are unable to maintain a stable pool of stem cells. Instead, plants suffer repetitive initiation, loss and re-initiation of stem cells, resulting in delayed, discontinuous and disorganized development. *wus* mutant plants generate small numbers of flowers eventually, but these lack central

organs and are infertile (Laux et al., 1996). Given that I had been able to establish all lines as homozygous, single-insertion lines and propagate them further, it was clear that all WUS fusion proteins largely complemented the infertility phenotype. But while the majority of plants looked similar to (Col-0) wildtype plants for all *wus* rescue lines, I was able to observe meristem termination at the vegetative or reproductive stage (Figure 8 A, B), which occurred at different frequencies within the different lines.

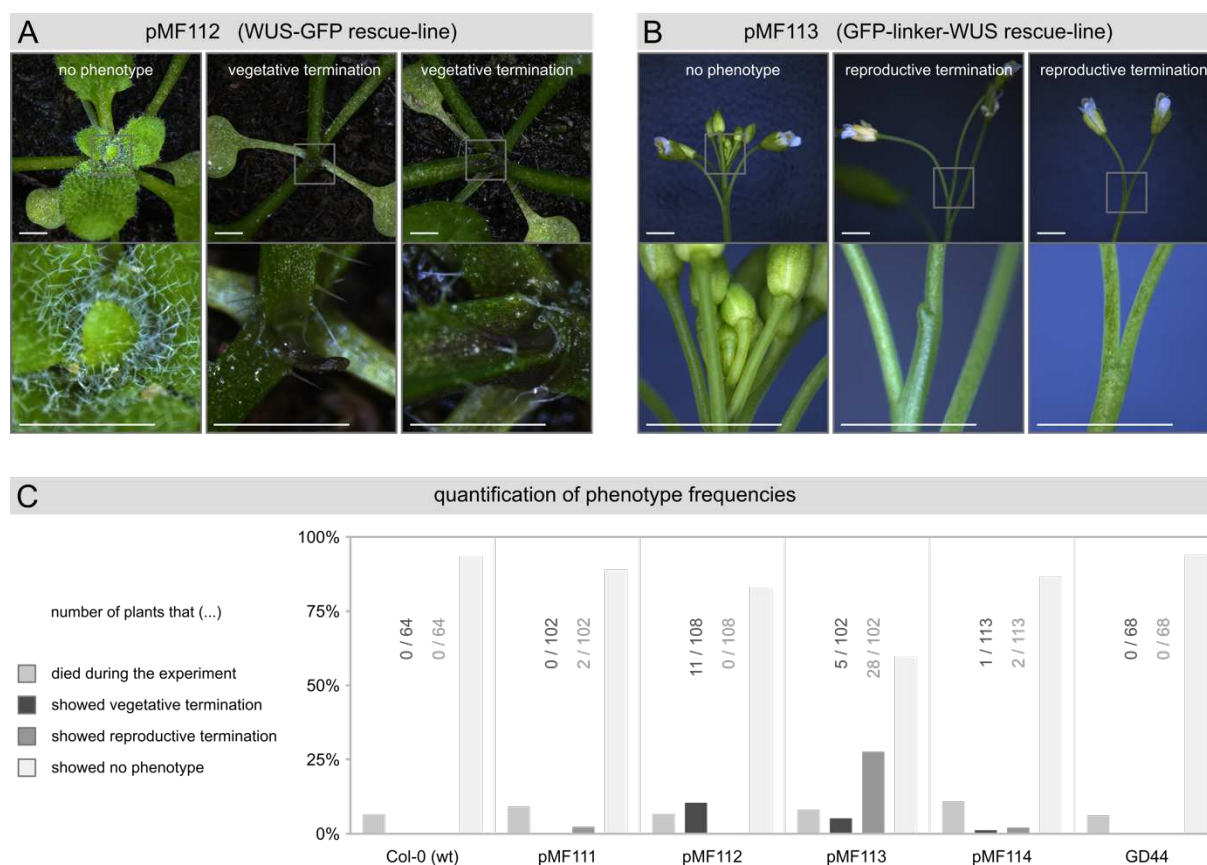


**Figure 8: Comparison of the frequency of meristematic phenotypes in *WUS* rescue lines.** (A) Vegetative termination phenotype versus unaffected plants in pMF112 (WUS-GFP rescue line): Affected plants produce a small number of leaves before the shoot meristem terminates and development is arrested. Subsequent growth results in the growth of atypical tissues. Scale bars represent a length of 2 mm. The bottom images represent a zoom of the top images, as highlighted by the gray boxes. (B) Reproductive termination phenotype versus unaffected plants in pMF113 (GFP-linker-WUS rescue line): Affected plants develop normally during vegetative development, but terminate the shoot meristem after growth of a small number of floral organs. No further organs are produced, but organs grown prior to termination develop normally. Scale bars represent a length of 2 mm. The bottom images represent a zoom of the top images, as highlighted by the gray boxes. (C) Quantification of the frequency of meristematic phenotypes occurring in pMF111 (GFP-WUS), pMF112 (WUS-GFP), pMF113 (GFP-linker-WUS), pMF114 (WUS-linker-GFP) and GD44 (WUS-linker-GFP) in comparison to the wildtype control Col-0 (wt).

Plants that were affected in vegetative development usually produced no more than 3-4 true leaves before the pool of apical stem cells was depleted, the shoot meristem was visibly lost

## Results

and development arrested. While new stem cells were re-initiated eventually, continued growth of plant tissue usually only resulted in the formation of disorganized, atypical structures. Plants that were affected in reproductive development grew normally during early development, forming a standard-sized rosette with regular number of leaves, and bolted at the same time as non-affected mutant rescue plants or wildtype control plants. After outgrowth of the main inflorescence the shoot apical meristem terminated eventually, producing only a small number of floral organs, which, however, appeared phenotypically normal and continued to develop siliques. Unlike for meristem termination in the vegetative stage, I could observe neither re-initiation of stem cells nor subsequent development of atypical organ structures. The outgrowth of secondary shoots from the rosette or the branching of side shoots from the main inflorescence seemed unaffected and these shoots also did not always show stem cell depletion themselves, further underlining a certain plasticity of the phenotype.

I could not observe termination of the meristem at the vegetative or reproductive stage for either the Col-0 wildtype control (0/64) or for GD44 (WUS-linker-GFP) (0/68) (Figure 8 C). pMF111 (GFP-WUS) showed a low frequency of termination during reproductive development (1.96% reproductive termination (2/102)), while for pMF114 (GFP-linker-WUS) both phenotypes occurred, but at similarly low frequency (0.88% vegetative termination (1/113), 1.76% reproductive termination (2/113)). In contrast, pMF112 (WUS-GFP) was clearly affected during vegetative development (10.19% vegetative termination (11/108)) and pMF113 (GFP-linker-WUS) showed a high rate of meristem termination at the vegetative as well as the reproductive stage (4.9% vegetative termination (5/102), 27.45% reproductive termination (28/102)). These data confirmed, that the small changes in vertical distribution between the different *WUS* alleles, which image quantification with the IFNH tool had revealed (Figure 7), are likely to represent functionally relevant differences.

Importantly, quantitative analysis of phenotype frequency and live-imaging data suggested no qualitative difference between a WUS fusion protein tagged at the N-terminus without a linker and a WUS fusion protein tagged at the C-terminus with the addition of a flexible serine-glycine linker between protein and fluorophore. Consequently, both tagging variants, which represent the two alleles most commonly used in the community, seem equally suited for the analysis of WUS mobility.

### 2.3. Analysis of interdependence between WUS protein mobility and tissue specific cellular environment

Proteins that are found outside of their mRNA expression domain, implying mobility of either the protein or the mRNA, are not uncommon in plants (Lee et al., 2006). While such mobility does not necessarily reflect functional relevance of cell-to-cell movement, it has been well established that in case of WUS the ability to move from the OC to the CZ is indispensable for its function (Daum et al., 2014). However, central questions regarding the mechanism of WUS mobility remain largely unanswered: First, does the WUS protein move via passive diffusion or is its mobility facilitated by a, yet unknown, active transport mechanism? Second, is the WUS gradient maintained by regulation of WUS mobility or via regulation of protein stability? And third, does WUS mobility or the regulation of the WUS gradient depend on WUS protein structure, including specific sequence stretches and domains, or on the tissue specific cellular environment?

To start answering these questions, I expressed a number of fusion proteins from the *WUS* promoter as well as from the *MERISTEM LAYER 1 (ML1)* promoter. Expression from the *WUS* promoter allowed me to assess upwards mobility within the meristem, from the L3 to the L1, while expression from the *ML1* promoter, which is epidermis-specific (Sessions et al., 1999), allowed me to assess downwards mobility, from the L1 to the L3. Since the use of C-terminal WUS fusion constructs with a flexible serine-glycine linker is well established

## Results

in our lab and my comparison of WUS tagging variants confirmed that this tagging strategy is suited for the analysis of WUS mobility, I continued using C-terminal tagging with a linker between the (WUS) fusion protein and the fluorophore. Unlike for the *wus* rescue constructs, where it had been necessary to use established lines, I decided to analyze T1 populations. Given that my previous experiment had shown variability to be high even within stable lines, I reasoned that the use of T1 populations would not drastically increase variability, but rather help to faithfully represent the full extent of natural variability, compensating for potential unconscious bias in line selection and differences in transgene expression specific to the genomic insertion site. Due to the large number of plants necessary for these experiments, I decided to switch from side-view imaging to top-view imaging (Fuchs and Lohmann, 2022), which offers a lower spatio-temporal resolution along the apical-basal axis of the SAM, but simpler and faster sample preparation and imaging.

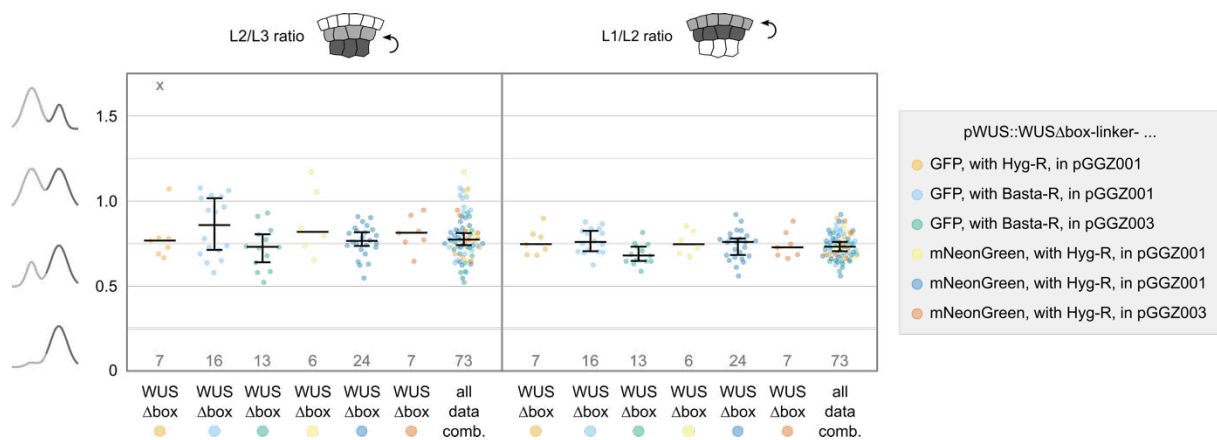


**Figure 9: Quantification of potential differences in signal distribution between different alleles for the same protein of interest.** Quantitative analysis of the vertical distribution of different alleles of WUS $\Delta$ box-linker-FP, expressed from the WUS promoter. Alleles differ in the fluorophore used (GFP or mNeonGreen), the plant resistance (hygromycin resistance (Hyg-R) or glufosinate ammonium (Basta-R)) or the plant destination vector (pGGZ001 or pGGZ003). Vertical distribution in the SAM is displayed as the ratio between L2 and L3, signifying mobility from L3 to L2, and as the ratio between L1 and L2, signifying mobility from L2 to L1. Individual data points represent individual plants. The median of each population is indicated by a black bar, together with the 95% confidence interval. The sample size is indicated in gray numbers below each population. The results of an ANOVA-Tukey HSD statistical test (significance value = 0.01; same letters indicate no statistically significant difference) are shown above each population.

To further increase sample size – and with that also the reliability of my statistical analysis – I also pooled plant populations, carrying constructs with the same protein of interest, but tagged with different fluorophores (GFP or mNeonGreen), containing different plant

resistance cassettes (BASTA or hygromycin) or using different plant destination vectors (pGGZ001 or pGGZ003). I could not observe systematic differences in distribution that would have suggested that the use of specific fluorophores, resistance cassettes or cloning vectors was relevant to the mobility of the protein of interest. Instead, when I pooled the data of several T1 populations, some of which appeared not to be normally distributed due to low sample size, the resulting population with increased sample size showed gaussian distribution (Figure 9).

Miss-expression of functional WUS protein in the shoot meristem leads to ectopic initiation of stem cells, over-proliferation and severe changes in tissue architecture (Schoof et al., 2000; Ma et al., 2019). Modifications to the WUS protein that increase its mobility have similar effects, while restriction of WUS movement leads to stem cell depletion and meristem termination (Daum et al., 2014; Ma et al., 2019). To analyze WUS protein mobility independent of protein function and feedback regulation, I used a mutation in the WUS box ( $\Delta$ box), which, according to earlier studies, renders the protein non-functional and transcriptionally inactive but does not qualitatively alter its mobility (Ikeda et al., 2009; Daum et al., 2014). I characterized the vertical distribution of WUS $\Delta$ box and compared these data to the distribution of 2xGFP, representing a non-nuclear diffusion control, and 2xGFP tagged with a strong nuclear localization signal (2xGFP-NLS), which according to a previous study does not move and therefore served as an immobile control (Daum et al., 2014). Since an earlier study has hypothesized that regulation of WUS distribution and maintenance of the WUS gradient may involve nuclear-cytoplasmic partitioning via C-terminal transcriptional domains (Rodriguez et al., 2016), I analyzed the vertical distribution of WUS $\Delta$ box, which has been N-terminally tagged with a nuclear export signal (NES-WUS $\Delta$ box) and should therefore be mostly excluded from the nucleus. I also analyzed the vertical distribution of MiniMe $\Delta$ box, an artificial WUS-like transcriptional repressor protein

## Results

where all endogenous WUS sequence except for the homeodomain, the (mutated) WUS box and the EAR motif has been replaced by flexible serine-glycine linker sequences. Both transcriptionally inactive MiniMe $\Delta$ box as well as MiniMe with a non-mutated WUS box show excessive protein movement to upper meristematic layers and expression of the latter leads to massively enlarged, fasciated meristems (Daum et al., 2014). Finally, I characterized the distribution of WUSCHEL RELATED HOMEODOMAIN 13 (WOX13) protein, which is the most distant member of the WOX gene family and the only WOX gene without a WUS box (Haecker et al., 2004), thus mimicking WUS $\Delta$ box. In addition, WUS and WOX13 share little overall sequence homology and the WOX13 homeodomain is distinctly different from the WUS homeodomain.

I expressed all constructs from the *WUS* promoter and first compared the distribution of fusion proteins via visual inspection (Figure 10): WUS $\Delta$ box(-linker-FP) showed clear nuclear localization and was visibly present in the OC and above, with a shallow, decreasing protein gradient from L3 to L1 in the center of the meristem. In comparison, 2xGFP was not distinctly nuclear but appeared similarly distributed, even though the protein seemed to spread more broadly in all directions. Addition of a strong NLS (2xGFP-NLS) on the other hand, led to exclusive nuclear localization in cells of the OC, with only weak nuclear signal observed in L2 and no signal in L1. NES-WUS $\Delta$ box(-linker-FP), while being specifically excluded from the nucleus, appeared unaffected in protein distribution and displayed a gradient similar to WUS $\Delta$ box and 2xGFP. In contrast, MiniMe $\Delta$ box(-linker-FP) was less nuclear than WUS $\Delta$ box and showed strong upwards mobility in the center as well as the periphery, forming what appeared to be a reverse gradient with the majority of MiniMe $\Delta$ box fusion protein located in L2 and L1, despite the construct being expressed from the *WUS* promoter in the OC below. WOX13(-linker-FP) looked similar to WUS $\Delta$ box regarding

nuclear localization, but displayed a much steeper protein gradient compared to WUS $\Delta$ box, with only a small amount of fusion protein found in the L1.

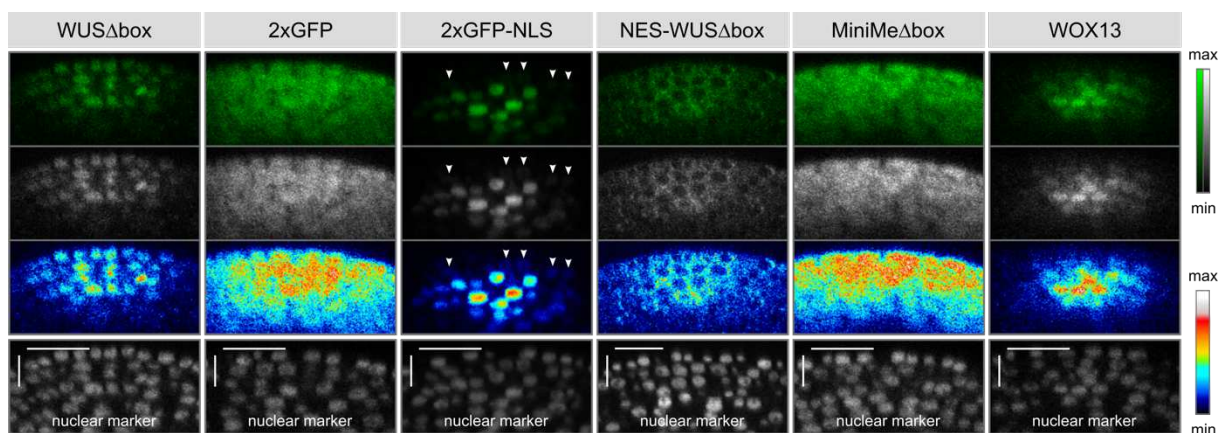


**Figure 10: Live-cell imaging of fusion proteins expressed from the WUS promoter to analyze upwards mobility.** Micrographs of fusion proteins (T1) in Col-0 wildtype plants, containing a genetically encoded, ubiquitous nuclear marker (T3 or higher). Images have been acquired from a top-view perspective. Horizontal and vertical scale bars represent a length of 15  $\mu$ m. White arrowheads point towards low abundantly 2xGFP-NLS protein in individual L2 cells.

Quantification of layer-specific fluorescence intensity (Figure 11) supported my initial visual analysis: 2xGFP-NLS (L2/L3 median ratio 0.264,  $n = 14$ ) showed minimal movement in L2 cells, but since its mobility was slightly higher than for 3xGFP-NLS (data not shown; data was obtained by me for a collaborative research project) the protein likely represents a diffusion control with a strong NLS rather than a completely immobile control. WOX13 (L2/L3 median ratio 0.497,  $n = 17$ ) exhibited higher L3 to L2 mobility, but moved less efficiently than WUS $\Delta$ box (L2/L3 median ratio 0.772,  $n = 73$ ) even though both proteins, judging from fluorescence images, appeared to have a similar nuclear-cytoplasmic ratio. Interestingly, NES-WUS $\Delta$ box (L2/L3 median ratio 0.943,  $n = 11$ ), which localizes almost exclusively to the cytoplasm, also showed higher mobility than WOX13 and WUS $\Delta$ box and moved not significantly different from freely diffusible 2xGFP (L2/L3 median ratio 0.972,  $n = 27$ ). MiniMe $\Delta$ box (L2/L3 median ratio 1.105,  $n = 55$ ) on the other hand moved significantly better than 2xGFP and 78% of the plants (43/55) had a L2/L3 ratio  $>1$ , while for 2xGFP this was only the case for 33% of the plants (9/27). Since the difference in movement correlates with a difference in size, MiniMe $\Delta$ box-linker-FP being slightly smaller

## Results

than 2xGFP, it seemed reasonable to assume that in both cases protein mobility was driven by passive diffusion. However, passive diffusion alone could not result in a concentration maximum outside of the OC, that is the domain where proteins expressed from the *WUS* promoter are synthesized. It is possible that variability within the analysis can in some cases lead to overestimation of the actual L2/L3 ratio, but since this effect would equally affect both analyses it offers no explanation for the difference between MiniMe $\Delta$ box and 2xGFP. Instead, I hypothesize that 2xGFP moves via passive diffusion, but MiniMe $\Delta$ box, additionally, moves via a yet unknown active transport mechanism.

Quantitative data for the L2 to L1 transition seemed to support this hypothesis: MiniMe $\Delta$ box (L1/L2 median ratio 0.820, n = 55) showed high mobility, significantly different from 2xGFP (L1/L2 median ratio 0.710, n = 27). Interestingly, and in contrast to my data on the L3 to L2 transition, WUS $\Delta$ box (L1/L2 median ratio 0.730, n = 73) moved similar to 2xGFP, even though the latter, lacking a nuclear localization signal or DNA binding domain, can diffuse freely. WUS $\Delta$ box and MiniMe $\Delta$ box on the other hand, both contain a homeodomain, which efficiently binds to chromatin, reducing the overall pool of unbound, mobile protein compared to 2xGFP. Therefore, for WUS $\Delta$ box to move similar to 2xGFP and for MiniMe $\Delta$ box to move even better, it seems reasonable to assume that WUS $\Delta$ box and MiniMe $\Delta$ box move via a different, likely active, mechanism. In accordance with this hypothesis, NES-WUS $\Delta$ box (L1/L2 median ratio 0.840, n = 11), which due to the addition of a nuclear export signal was hardly nuclear and therefore only a small fraction should be bound to chromatin despite the protein containing the WUS homeodomain, moved significantly better than 2xGFP. WOX13 (L1/L2 median ratio 0.432, n = 17), which has little sequence homology with WUS, but can bind chromatin via its own homeodomain, likely making it a more suitable diffusion control than 2xGFP, showed significantly reduced L2-to-L1 mobility, further supporting the idea of an active mechanism for WUS transport. For

2xGFP-NLS (L1/L2 median ratio 0.348,  $n = 14$ ), L2-to-L1 mobility seemed increased, compared to movement from the L3 to the L2, but since I had barely observed any fluorescence signal in L2 and no signal at all in L1, it is unlikely that this represents a biologically relevant effect, but rather an analysis artifact.

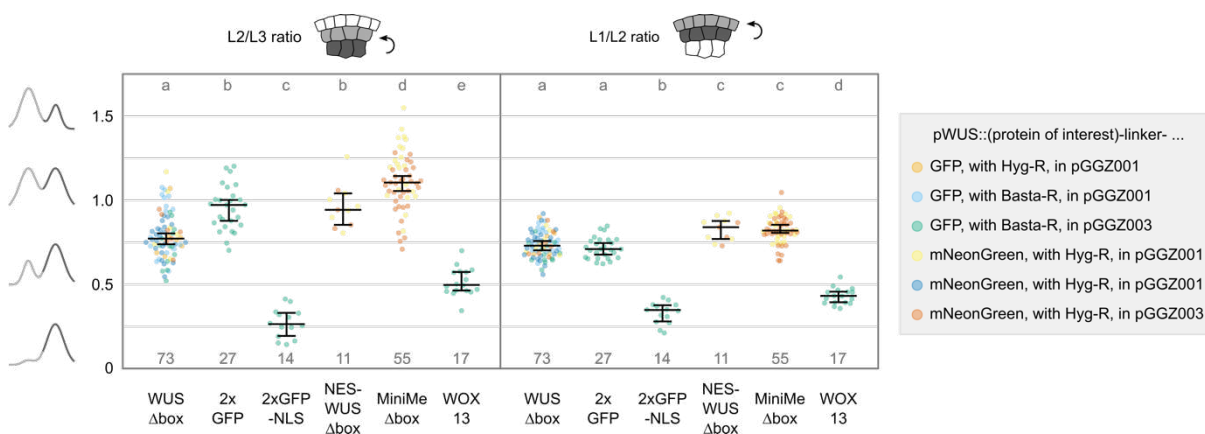


**Figure 11: Quantification of fusion proteins expressed from the *WUS* promoter to analyze upwards mobility.** Vertical distribution in the SAM is displayed as the ratio between L2 and L3, signifying mobility from L3 to L2, and as the ratio between L1 and L2, signifying mobility from L2 to L1. Individual data points represent individual plants; different colors for data points represent different constructs carrying the same protein of interest. The median of each population is indicated by a black bar, together with the 95% confidence interval. The sample size is indicated in gray numbers below each population. The results of an ANOVA-Tukey HSD statistical test (significance value = 0.01; same letters indicate no statistically significant difference) are shown above each population. The *WUS* $\Delta$ box dataset was already shown in Figure 9.

To investigate the role of the tissue specific cellular environment on protein mobility, I expressed the same set of constructs from the L1-specific *MLI* promoter and again analyzed vertical distribution of all fusion proteins in the SAM. Initial visual inspection of fluorescence images (Figure 12) did not show qualitative changes with regard to sub-cellular localization and mobility compared to expression from the *WUS* promoter: 2xGFP-NLS did not move beyond its expression domain, but was observed only in the L1, while WOX13 consistently moved at least one cell layer further and was found also in the L2. All other fusion proteins, *WUS* $\Delta$ box, NES-*WUS* $\Delta$ box, MiniMe $\Delta$ box and 2xGFP, were consistently found in L2 and L3, moving at least 3-4 cell layers downwards, which is in line with previously published results (Daum et al., 2014).

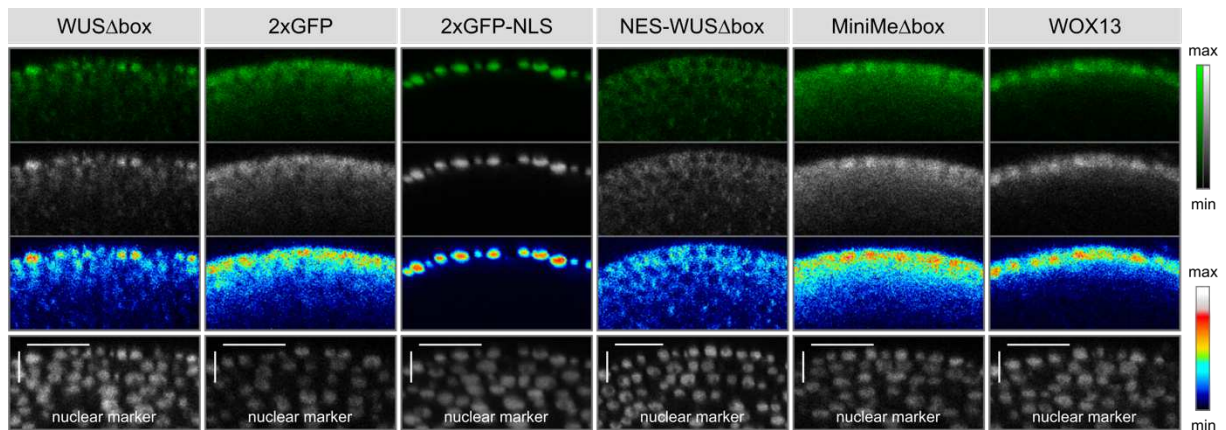


**Figure 12: Live-cell imaging of fusion proteins expressed from the *MLI* promoter to analyze downwards mobility.** Micrographs of fusion proteins (T1) in Col-0 wildtype plants, containing a genetically encoded, ubiquitous nuclear marker (T3 or higher). Images have been acquired from a top-view perspective. Horizontal and vertical scale bars represent a length of 15  $\mu\text{m}$ .

Quantitative analysis using the IFNH tool (Figure 13) confirmed low downwards mobility of 2xGFP-NLS (L2/L1 median ratio 0.236,  $n = 28$ ). WOX13 (L2/L1 median ratio 0.615,  $n = 23$ ) showed significantly higher L1-to-L2 mobility compared to 2xGFP-NLS, but moved significantly lower than the similarly nuclear WUS $\Delta$ box (L2/L1 median ratio 0.829,  $n = 90$ ). At the same time, WUS $\Delta$ box was not significantly different from 2xGFP (L2/L1 median ratio 0.805,  $n = 11$ ), despite the latter being able to freely diffuse. These data confirmed that WUS $\Delta$ box moved more than its diffusion controls, suggesting that active WUS transport may not be limited to (upwards) movement from the OC to the CZ, but may also facilitate mobility in the reverse direction, albeit potentially less efficient as suggested by a visual comparison of *pWUS* and *pMLI* fluorescence images. In line with my previous data and with my hypothesis, NES-WUS $\Delta$ box (L2/L1 median ratio 1.004,  $n = 39$ ) moved significantly better than WUS $\Delta$ box, but also showed higher mobility than MiniMe $\Delta$ box (L2/L1 median ratio 0.886,  $n = 40$ ), where my analysis revealed a larger fraction of protein to remain within the layer of synthesis (L1), compared to expression from the *WUS* promoter (L3). This again suggested that while a potential mechanism for active WUS transport would likely be non-directional, it seems to promote movement in the basal-apical direction (upwards) more efficiently than movement in the apical-basal direction (downwards). In addition, the

difference observed between MiniMe $\Delta$ box and NES-WUS $\Delta$ box allowed to speculate whether active WUS transport might be geared towards preventing (nuclear) WUS from leaving the L1 again.

Analysis of L2-to-L3 mobility revealed no significant difference between WUS $\Delta$ box (L3/L2 median ratio 0.712, n = 90), NES-WUS $\Delta$ box (L3/L2 median ratio 0.714, n = 39), MiniMe $\Delta$ box (L3/L2 median ratio 0.700, n = 40) and 2xGFP (L3/L2 median ratio 0.648, n = 11). It was interesting to notice though, that 2xGFP showed the lowest mobility of all four fusion proteins and given the high variability in combination with low sample size, the effect might have been different in a larger population. In line with my hypothesis, but also with previous visual inspection (Figure 12), WOX13 (L3/L2 median ratio 0.445, n = 23) displayed lower L2-to-L3 mobility than WUS $\Delta$ box, but also moved less efficiently from L2 to L3, compared to L1 to L2. In contrast, 2xGFP-NLS (L3/L2 median ratio 0.313, n = 28) showed an increased L2-to-L3 mobility, compared to its L1-to-L2 mobility, but similar to expression from the *WUS* promoter, it is highly arguable whether this result is biologically meaningful due to the apparent lack of fusion protein in L2 and L3 (Figure 12).

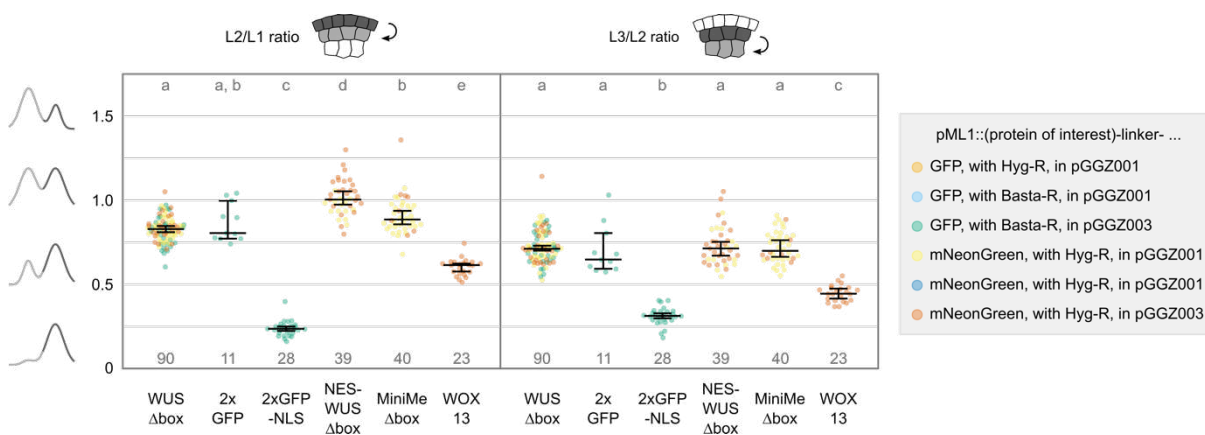


**Figure 13: Quantification of fusion proteins expressed from the *MLI1* promoter to analyze downwards mobility.** Vertical distribution in the SAM is displayed as the ratio between L2 and L1, signifying mobility from L1 to L2, and as the ratio between L3 and L2, signifying mobility from L2 to L3. Individual data points represent individual plants; different colors for data points represent different constructs carrying the same protein of interest. The median of each population is indicated by a black bar, together with the 95% confidence interval. The sample size is indicated in gray numbers below each population. The results of an ANOVA-Tukey HSD statistical test (significance value = 0.01; same letters indicate no statistically significant difference) are shown above each population.

## Results

The comparison of data on all layer transitions, including upwards-directed L3-to-L2 and L2-to-L1 movement for constructs driven from the *WUS* promoter as well as downwards-directed L1-to-L2 and L2-to-L3 movement for constructs driven from the *ML1* promoter, suggested that despite WUS mobility being non-directional, its regulation likely contains a layer-sensitive component. WUS $\Delta$ box and 2xGFP moved highly similar from the L2 to the L1, in the reverse direction from the L1 to the L2 and also from the L2 towards OC cells in the L3, which, given the differences between the two proteins, suggested a mode of active transport for WUS $\Delta$ box, however, upwards mobility from the OC (L3-to-L2 mobility) was significantly lower. Therefore, I postulate the existence of a regulatory mechanism that works via protein retention in the OC. L3-specific protein retention seemed to similarly apply to active transport of NES-WUS $\Delta$ box but neither to active transport of MiniMe $\Delta$ box nor diffusion of WOX13, suggesting that the mechanism for protein retention was specific to protein sequence outside the homeodomain and the EAR motif.

In summary, these data allowed the hypothesis that WUS movement includes a yet undescribed component of active transport, which, while not being directional per se, is regulated via a mechanism for protein retention in L3 cells.

### 2.4. Comparison of downwards mobility between the OC and the periphery

Since WUS moves predominantly along the apical-basal axis, from the OC to the CZ, and it is mostly required in the stem cells in the central zone, I hypothesized that a potential mechanism for active WUS movement could also be limited to the center and might not be present in the periphery. To test this idea, I created an optional workflow for the analysis of an additional peripheral domain, surrounding the central analysis domain, and implemented it in the IFNH plugin. I then analyzed the vertical distribution of fluorescence signal within a hollow cylinder (donut) with a diameter of 40  $\mu$ m and a thickness of 10  $\mu$ m, for various fusion proteins expressed from the *ML1* promoter. Unlike the *WUS* promoter, which is

expressed in the center of the SAM, but does not extend towards the periphery, expression of the *ML1* promoter covers the whole epidermis, allowing me to assess differential mobility between the center and the periphery – however only for downwards-directed movement and not upwards-directed mobility. Here I saw, that WUS $\Delta$ box, NES-WUS $\Delta$ box and MiniMe $\Delta$ box did not show differential mobility between the CZ and the peripheral zone (PZ), suggesting that a postulated mechanism for active WUS transport likely facilitates (downwards-directed) mobility in the center as well as the periphery (Figure 14). Similarly, analysis of WOX13 and 2xGFP also revealed no differences in vertical distribution between the CZ and the PZ, suggesting that passive diffusion, downwards along the apical-basal axis, also likely faces no domain specific barriers between central zone and periphery (Figure 14).

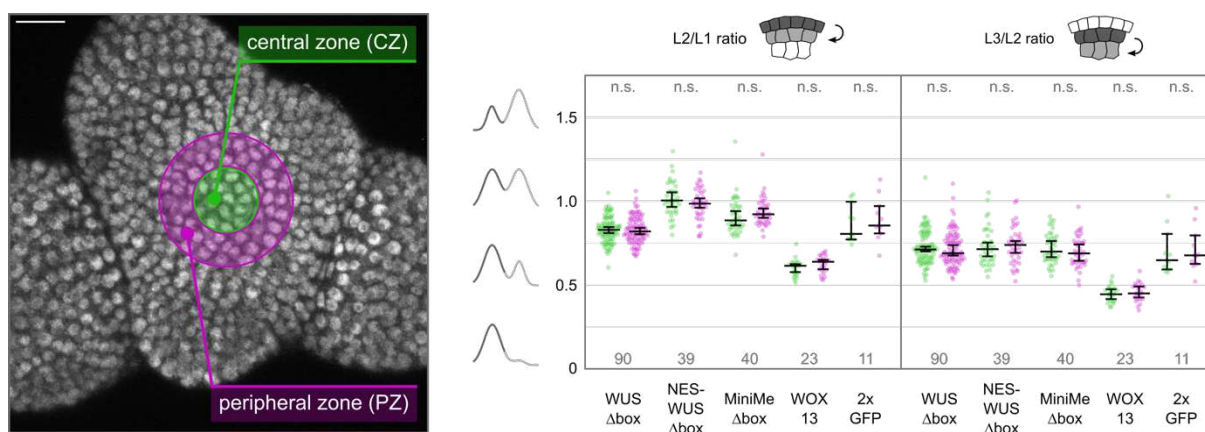


**Figure 14: Quantification of fusion proteins expressed from the *ML1* promoter to analyze downwards mobility in the central zone (CZ) compared to the peripheral zone (PZ).** Representation of the analysis domains for the CZ and PZ in the shoot meristem from a top-view perspective. Vertical distribution in the SAM is displayed as the ratio between L2 and L1, signifying mobility from L1 to L2, and as the ratio between L3 and L2, signifying mobility from L2 to L3. Individual data points represent individual plants; green data points represent analysis in the CZ and purple data points represent analysis in the PZ. The median of each population is indicated by a black bar, together with the 95% confidence interval. The sample size is indicated in gray numbers below each population. The results of a two-tailed Student's t-Test with unequal variance (significance value = 0.05; n.s. = no statistically significant difference) are shown above each population. The WUS $\Delta$ box CZ, NES-WUS $\Delta$ box CZ, MiniMe $\Delta$ box CZ, WOX13 CZ and 2xGFP CZ datasets were already shown in Figure 13.

A recent study has suggested that nuclear-cytoplasmic ratio and cytoplasmic stability of the WUS protein were controlled in a *CLV3*-dependent manner (Plong et al., 2021). Plong and colleagues base their hypothesis on experiments including exogenous application of *CLV3* peptide as well as over-expression of a protein fusion of WUS with the glucocorticoid

## Results

receptor (GR) and GFP (GFP-WUS-GR), which upon induction with the chemical dexamethasone translocates to the nucleus. However, a GFP-WUS-GR fusion protein likely represents only a crude approximation of a functional WUS molecule, due to its large size and tagging from both sides. In contrast, my transgenic lines and, more importantly, the ability to reliably quantify fluorescence signal along the apical-basal axis in the meristem, not only in the center, with high levels of CLV3 present, but also in the periphery, with low levels of CLV3 present (Figure 15), allowed me to test this hypothesis in a more natural setting, at the same time eliminating the need for exogenous application of either dexamethasone or CLV3 peptide.

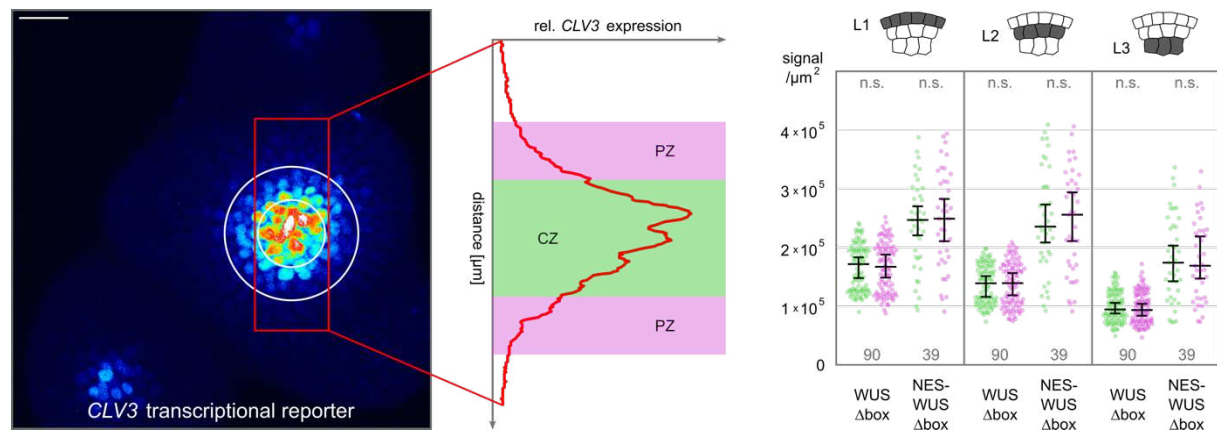


**Figure 15: Quantitative comparison of the signal intensity of nuclear (WUS $\Delta$ box) and cytoplasmic (NES-WUS $\Delta$ box) WUS expressed from the *MLI* promoter in the CZ (high levels of CLV3) compared to the PZ (lower levels of CLV3).** Signal intensity of a transcriptional *CLV3* reporter in CZ and PZ in the shoot meristem from a top-view perspective. Signal intensity of WUS $\Delta$ box and NES-WUS $\Delta$ box translational reporters is normalized to the area of the analysis domain. Individual data points represent individual plants; green data points represent analysis in the CZ and purple data points represent analysis in the PZ. The median of each population is indicated by a black bar, together with the 95% confidence interval. The sample size is indicated in gray numbers below each population. The results of a two-tailed Student's t-Test with unequal variance (significance value = 0.05; n.s. = no statistically significant difference) are shown above each population.

Therefore, I quantified the signal intensity of WUS $\Delta$ box, which predominantly localizes to the nucleus, and NES-WUS $\Delta$ box, which is mostly found in the cytoplasm, in the CZ and the periphery in L1, L2 and L3. I then normalized the intensity to the size of the area included in the analysis domain and took the intensity per area as a measure for absolute protein levels. Here, I found no difference between the protein levels of either WUS $\Delta$ box or NES-WUS $\Delta$ box in the center versus the periphery in L1, L2 or L3 (Figure 15), despite the

differential accumulation of endogenous CLV3 peptide, whose expression levels decrease from the CZ towards the PZ and from the L1 to the L3. In conclusion, these data did not support a hypothesized CLV3-dependent mechanism for maintaining the WUS gradient.

## 2.5. The role of conserved protein motifs for WUS mobility

The data I have presented so far suggests an active transport mechanism that promotes mobility of (nuclear) WUS $\Delta$ box, of (cytosolic) NES-WUS $\Delta$ box and even of the MiniMe $\Delta$ box protein, where most stretches of original WUS sequence have been replaced by unrelated serine-glycine linker sequence. In contrast, WOX13, which is a distant member of the *WOX* gene family, also sharing little sequence homology with WUS, and the structurally unrelated 2xGFP seem to not be transported by the same mechanism, raising the question how specificity of active WUS transport might be achieved.

(Actively transported) MiniMe $\Delta$ box contains the WUS homeodomain, the (mutated) WUS box and the EAR motif, while (not actively transported) WOX13 contains a homeodomain not identical with the WUS homeodomain and lacks a WUS box as well as the EAR motif. Therefore, I decided to first focus on the role of the EAR motif: I created a fusion protein containing a mutation in both the WUS box and the EAR motif (WUS $\Delta$ box $\Delta$ EAR) (mutations described in Ikeda, Mitsuda, and Ohme-Takagi 2009), expressed it from the *WUS* promoter and imaged T1 plants from a top-view perspective. Initial visual inspection showed no striking differences in vertical distribution for WUS $\Delta$ box $\Delta$ EAR(-linker-FP) compared to WUS $\Delta$ box. Both proteins were similarly nuclear and displayed a shallow L3-to-L1 gradient, with decreasing protein levels towards the L1 (Figure 16). Similarly, when I analyzed the data using my IFNH plugin, I found no statistically significant difference between WUS $\Delta$ box $\Delta$ EAR (L3/L2 median ratio 0.798, L2/L1 median ratio 0.704, n = 24) and WUS $\Delta$ box (L3/L2 median ratio 0.772, L2/L1 median ratio 0.730, n = 73) (Figure 16), indicating that the EAR motif is an unlikely candidate to mediate transport specificity.

## Results

Similarly, it is unlikely that the EAR motif is involved in the control of WUS mobility or stability, unless one assumes a scenario, where the WUS box would be epistatic over the EAR motif.

To take a closer look at the WUS box, I then went back to my previous dataset for transcriptionally active WUS(-linker-GFP). Even though these data are not directly comparable to WUS $\Delta$ box (or WUS $\Delta$ box $\Delta$ EAR), as they represent an established line (T3) in the *wus* mutant background imaged from a side-view perspective, rather than T1 populations in the wildtype background imaged from a top-view perspective, a comparison might still be informative. Initial analysis based on visual inspection of fluorescence images suggested that for WUS $\Delta$ box and WUS $\Delta$ box $\Delta$ EAR, containing the inactivating  $\Delta$ box mutation, the amount of cytosolic protein seemed slightly larger than for functional WUS, which appears strictly nuclear (Figure 16), likely reflecting the loss of protein-protein interaction with nuclear proteins like the transcriptional co-repressor TOPLESS (TPL) (Kieffer et al., 2006; Long et al., 2006; Ikeda et al., 2009). Comparison of the quantitative data revealed that WUS (L2/L3 median ratio 0.634, L1/L2 median ratio 0.464, n = 24) containing a functional WUS box moved significantly less than WUS $\Delta$ box (L3/L2 median ratio 0.772, L2/L1 median ratio 0.730, n = 73) or WUS $\Delta$ box $\Delta$ EAR (L3/L2 median ratio 0.798, L2/L1 median ratio 0.704, n = 24) (Figure 16), both from L3 to L2 as well as from L2 to L1. Again, this difference in mobility is likely caused by the inability of  $\Delta$ box proteins to interact with proteins and protein complexes of the transcription machinery, as such interactions likely render the protein immobile for the duration of the interaction. Consequently, for WUS protein, which contains a non-mutated, functional WUS box, a larger fraction of molecules is unavailable for cell-to-cell transport at any given time, compared to WUS $\Delta$ box and WUS $\Delta$ box $\Delta$ EAR, which cannot engage in protein-protein interactions mediated by the WUS box. Interestingly, the difference in mobility between

WUS and  $\Delta$ box proteins was larger for the transition from L2 to L1 than for the L3-to-L2 transition, again hinting towards the presence of a regulatory mechanism in the L3 that, while potentially including protein-protein interactions via the WUS box, is not dependent on the WUS box. Additionally, considering the mobility of WUS, WUS $\Delta$ box and WOX13 (L3/L2 median ratio 0.497, L2/L1 median ratio 0.432,  $n = 17$ ) (Figure 16), which from L2 to L3 moves less than WUS and WUS $\Delta$ box, with which it shares the  $\Delta$ box mutation, and from L2 to L1 moves less than WUS $\Delta$ box and as much as WUS, despite containing the  $\Delta$ box mutation, these data suggest that specificity of active WUS transport might be mediated via the WUS homeodomain.

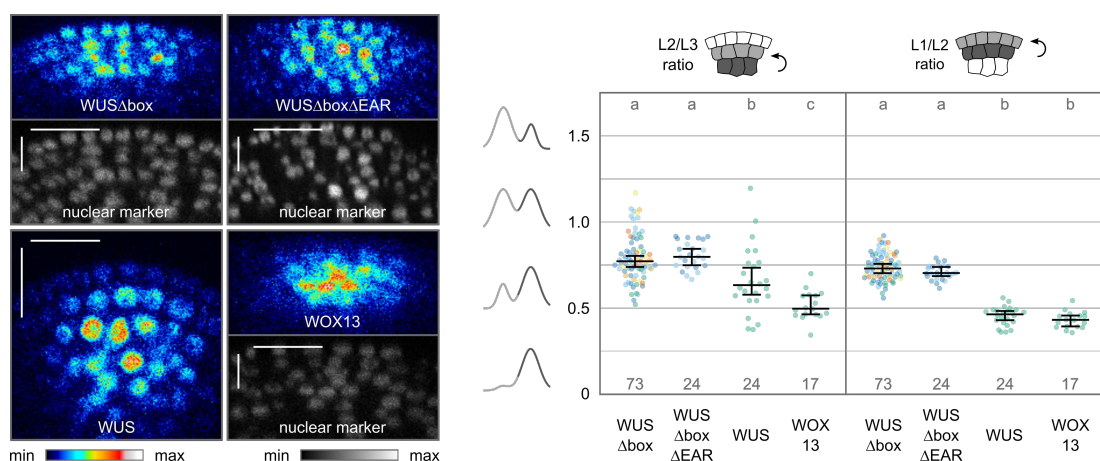


**Figure 16: Analysis of conserved domains at the WUS C-terminus.** Visual comparison of WUS-linker-GFP (T3 rescue line, imaged from a side-view perspective) and WUS $\Delta$ box, WUS $\Delta$ box $\Delta$ EAR and WOX13 (T1 in wt background, imaged from a top-view perspective) expressed from the *WUS* promoter. Scale bars represent a length of 15  $\mu$ m. Vertical distribution in the SAM is displayed as the ratio between L2 and L3, signifying mobility from L3 to L2, and as the ratio between L1 and L2, signifying mobility from L2 to L1. Individual data points represent individual plants; different colors for data points represent different constructs carrying the same protein of interest. The median of each population is indicated by a black bar, together with the 95% confidence interval. The sample size is indicated in gray numbers below each population. The results of an ANOVA-Tukey HSD statistical test (significance value = 0.01; same letters indicate no statistically significant difference) are shown above each population. The WUS $\Delta$ box dataset was already shown in Figure 9 and Figure 11. The WUS(-linker-GFP) dataset was already shown in Figure 7. The WOX13 dataset was already shown in Figure 11.

## 2.6. The influence of NLS-tagging on WUS mobility

Having seen that 2xGFP-NLS barely moves in comparison to 2xGFP, both of which I have to assume to move via passive diffusion, I wondered whether WUS $\Delta$ box, for which my data suggests the presence of an active transport mechanism, would remain mobile despite the addition of a strong NLS. Therefore, I compared L3-to-L2 mobility, as a measure for

## Results

upwards movement, and L1-to-L2 mobility, as a measure for downwards movement, for 2xGFP-NLS and NLS-WUS $\Delta$ box(-linker-mNeonGreen) expressed from the *WUS* promoter as well as the *MLI* promoter. For upwards mobility, I observed no statistically significant difference between 2xGFP-NLS (L2/L3 median ratio 0.264, n = 14) and NLS-WUS $\Delta$ box (L2/L3 median ratio 0.279, n = 10), suggesting that the addition of a strong nuclear localization signal, introducing yet another potential barrier for protein mobility, prevented active WUS transport (Figure 17). For downwards mobility, however, I saw that NLS-WUS $\Delta$ box (L2/L1 median ratio 0.398, n = 11) moved significantly better than 2xGFP-NLS (L2/L1 median ratio 0.236, n = 28) (Figure 17). This was a strong indication that active WUS transport was able to overcome the limitations caused by addition of a strong NLS, again supported the notion of such a transport mechanism to work bi-directionally and also supported the hypothesis of transport regulation via a retention of the WUS protein specifically in L3 cells.

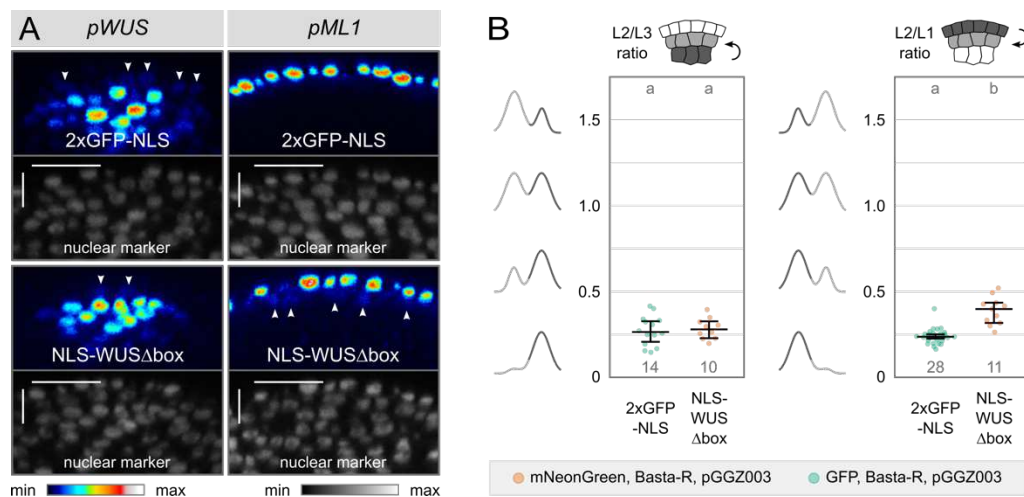


**Figure 17: Analysis of the effects of a strong nuclear localization signal (NLS) on protein mobility.** Visual comparison of 2xGFP-NLS and NLS-WUS $\Delta$ box(-linker-FP) expressed from the *WUS* promoter and the *MLI* promoter. Scale bars represent a length of 15  $\mu$ m. Vertical distribution in the SAM is displayed as the ratio between L2 and L3, signifying (upwards) mobility from L3 to L2, and as the ratio between L2 and L1, signifying (downwards) mobility from L1 to L2. Individual data points represent individual plants; different colors for data points represent different constructs carrying the same protein of interest. The median of each population is indicated by a black bar, together with the 95% confidence interval. The sample size is indicated in gray numbers below each population. The results of an ANOVA-Tukey HSD statistical test (significance value = 0.01; same letters indicate no statistically significant difference) are shown above each population. The 2xGFP-NLS datasets were already shown in Figure 11 and Figure 13.

## 2.7. Linker-Scanning to identify regulatory sequence in the WUS protein

To further investigate the regulation of active WUS transport, I again focused on the differences between WUS $\Delta$ box and the MiniMe $\Delta$ box fusion protein. A previous study has shown the presence of regulatory sequences between the homeodomain and the WUS box, but has found no evidence for regulation of mobility within either the WUS N-terminus or its C-terminus (Daum et al., 2014). Based on these results, I decided to perform a systematic linker-scanning experiment, leveraging the increased sensitivity offered by my IFNH quantification tool.

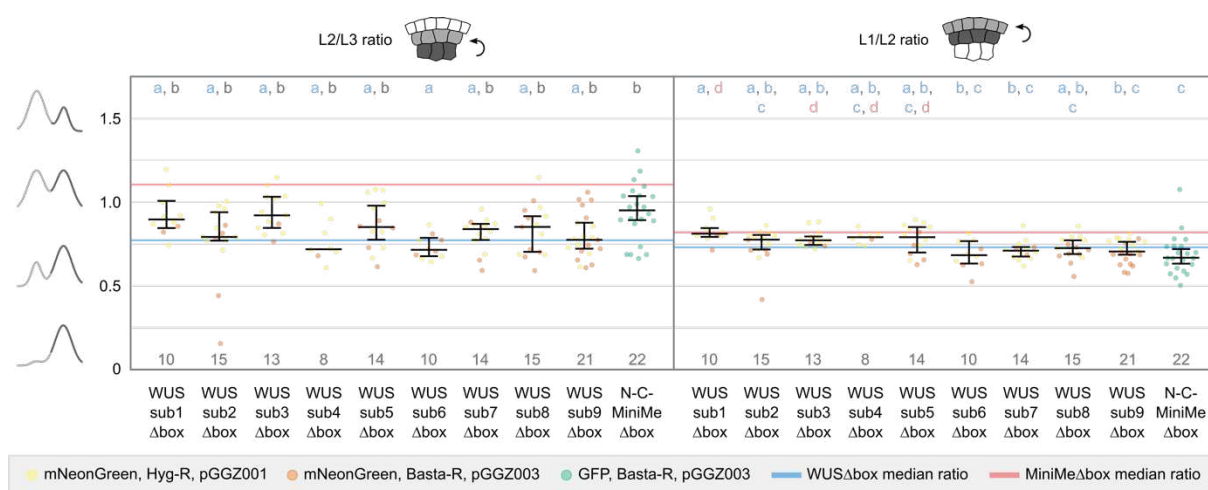


**Figure 18: Quantification of the mobility of linker-scanning alleles expressed from the WUS promoter.** Vertical distribution in the SAM is displayed as the ratio between L2 and L3, signifying mobility from L3 to L2, and as the ratio between L1 and L2, signifying mobility from L2 to L1. Individual data points represent individual plants; different colors for data points represent different constructs carrying the same protein of interest. The median of each population is indicated by a black bar, together with the 95% confidence interval. Blue and red lines represent the median ratios of previously shown WUS $\Delta$ box and MiniMe $\Delta$ box populations. The sample size is indicated in gray numbers below each population. The results of an ANOVA-Tukey HSD statistical test (significance value = 0.01; same letters indicate no statistically significant difference) are shown above each population.

To this end, I created a WUS-MiniMe hybrid protein, termed N-C-MiniMe $\Delta$ box, which is identical to MiniMe $\Delta$ box in sequence between the homeodomain and the (mutated) WUS box, but contains the endogenous WUS N-terminus as well as C-terminus. I also created nine substitution alleles of WUS $\Delta$ box, in which subsequent sequence stretches of 17 amino acids (aa) were replaced with unspecific, flexible serine-glycine linker, similar to the original MiniMe-approach. I used C-terminal tagging for all constructs, including a flexible linker

## Results

between WUS and the fluorophore (GFP or mNeonGreen), expressed them from the *WUS* promoter and performed live-cell imaging from a top-view perspective. Initial visual analysis suggested that all alleles were qualitatively similar to  $WUS\Delta\text{box}$  and none showed increased mobility comparable to  $\text{MiniMe}\Delta\text{box}$ . However, quantification of these data using the IFNH plugin revealed that while N-C-MiniMe (L2/L3 median ratio 0.950,  $n = 22$ ) moved significantly less from the L3 to the L2 compared to  $\text{MiniMe}\Delta\text{box}$  (L2/L3 median ratio 1.105,  $n = 55$ ), it still moved significantly better than  $WUS\Delta\text{box}$  (L2/L3 median ratio 0.772,  $n = 73$ ) (Figure 18). Together with the data I have acquired previously, which suggested a regulatory mechanism via L3-specific WUS retention, this finding points to the presence of regulatory sequences not only within the sequence between the WUS homeodomain and WUS box, as published by an earlier study (Daum et al., 2014), but – in contrast to the findings by Daum and colleagues – also within the N-terminus as well as the C-terminus of the WUS protein. Quantification of the substitution alleles, covering the sequence stretch implied to carry regulatory function by Daum and colleagues, revealed that all single substitution alleles were not significantly different from  $WUS\Delta\text{box}$ . Interestingly though, all substitution alleles, except for  $WUS\text{sub}6\Delta\text{box}$ , were also not statistically significant from  $\text{N-C-MiniMe}\Delta\text{box}$ , confirming my visual analysis in that no single substitution was able to recreate the drastic MiniMe phenotype and suggesting slightly increased, intermediate mobility. It also appears, that the regulatory role of the large sequence stretch between the WUS homeodomain and WUS box cannot be attributed to one or more smaller sequence stretches, likely due to secondary structure and folding of the protein. Interestingly, the differences in mobility observed between all fusion proteins became less apparent when looking at the mobility from the L2 towards the L1: Here, all substitution alleles, including N-C-MiniMe, were not significantly different from  $WUS\Delta\text{box}$ , while statistical analysis in addition even grouped some together with  $\text{MiniMe}\Delta\text{box}$ . The diminished difference

regarding L2-to-L1 mobility in alleles partially affected in regulation of WUS movement, again seems to support the idea that active WUS transport is regulated in an L3-specific manner.

## 2.8. Analysis of proteins conferring the *WUS* function in other species

To investigate regulation of WUS mobility from a different angle, I aimed to characterize the mobility of proteins that fulfill WUS function in other species: To this end I cloned the *ROSULATA* (*ROA*) gene from *Antirrhinum majus* (snapdragon), the *TERMINATOR* (*TER* or *PhWUS*) gene from *Petunia hybrida* (petunia) and the *WUSCHEL* (*LeWUS*) gene from *Solanum lycopersicum* (tomato) and created C-terminal linker-FP fusion proteins expressed under the control of a 4.4 kb and a 2.8 kb fragments of the *WUS* promoter and terminator, respectively. I then transformed these constructs in *wus* mutant plants to see whether they would rescue the *wus* phenotype in Arabidopsis. Unfortunately, the number of transgenic plants, despite several subsequent rounds of T1 selection, was really low and a fraction of these plants showed meristematic phenotypes. For *ROA* (snapdragon *WUS*), I got a total of 6 transgenic plants. Of these plants, two showed the *wus* mutant phenotype and another appeared *wus*-like at first but then developed an over-proliferation phenotype (Figure 19). For *TER* (petunia *WUS*), I had a total of 10 transgenic plants with two of them being fasciated due to over-proliferation (Figure 19) and for *LeWUS* (tomato *WUS*), I got 13 transgenic plants, of which one suffered from meristem termination and yet another had a fasciated meristem (Figure 19). I genotyped all plants for the *wus* locus, which here could be homozygous for either the *WUS* wildtype allele or the *wus* mutant allele or heterozygous for both, and while I could not see a clear correlation between the homozygous Arabidopsis *wus* mutant allele and meristematic phenotypes occurring, all four plants that showed a fasciated meristem due to over-proliferation were homozygous for the *wus* mutant allele. I then proceeded to image all plants and found that, across all lines, the majority of the plants that

## Results

had appeared phenotypically normal, did either not express the rescue construct at all or had no sufficient expression in the central SAM, but only in primordia, reducing the number of plants that were suitable for analysis, visual or quantitative, to three plants for *ROA*, four plants for *TER* and only two for *LeWUS*, including those with over-proliferation phenotypes. Interestingly, visual analysis of fluorescence images seemed to suggest that the plants showing over-proliferation formed concentration maxima outside of the OC, similar to MiniMe (Figure 19). Quantitative analysis using my IFNH tool confirmed this impression: All fasciated plants, which were also all homozygous for the *wus* mutation, had a high L2/L3 ratio (*ROA*-linker-mNeonGreen: 1.249; *TER*-linker-mNeonGreen: 1.482 and 1.702; *LeWUS*-linker-mNeonGreen: 1.209). On the other hand, there were also two plants that were genotyped as homozygous *wus* mutant plants, did not show a meristematic phenotype, and had either a similarly high L2/L3 ratio (*LeWUS*-linker-mNeonGreen: 1.580) or a comparatively low L2/L3 ratio together with a higher L1/L2 ratio (*TER*-linker-mNeonGreen: 0.411 (L2/L3), 0.690 (L1/L2)). Heterozygous plants as well as wildtype plants tended to show slightly increased mobility compared to *Arabidopsis WUS*, as indicated by higher layer ratios, but given that these plants still contained one or two functional alleles of the endogenous *WUS*, I would consider them less informative. Overall, none of the proteins analyzed here was able to reliably rescue the *wus* mutant phenotype. Instead, they seemed to show increased mobility, resulting in over-proliferation phenotypes similar to the MiniMe protein, suggesting a potential loss of regulation. Due to the extremely low sample size, however, these data and their analysis remains speculative.

Given the difficulties in characterizing rescue lines, I did not proceed with establishing stable lines, but decided to change my strategy and analyze the mobility of non-functional alleles of *ROA*, *TER* and *LeWUS*. To this end, I created constructs containing the  $\Delta$ box mutation, expressed all fusion proteins from the *WUS* promoter in *WUS* wildtype plants and aimed to

characterize large T1 populations. However, while I got more transgenic plants (34 for *ROAΔbox*, 33 for *TERΔbox*, 27 for *LeWUSΔbox*), the vast majority of these did either not express the fusion protein (*ROAΔbox*-linker-mNeonGreen, *TERΔbox*-linker-mNeonGreen or *LeWUSΔbox*-linker-mNeonGreen) or only in larger primordia. Only for *TERΔbox*, two plants had sufficient expression of the fusion protein in the central SAM and these showed diffuse, partially non-nuclear accumulation (data not shown). Quantification of these two individuals, again seemed to support slightly increased mobility, which is not surprising given the partially cytoplasmic localization and also might not at all be representative for a larger population.

In summary, my analysis of proteins that fulfil the *WUS* function in other species, namely petunia, snapdragon and tomato, remained inconclusive due to small sample sizes. The data that I have acquired, however, suggests that these proteins in *Arabidopsis* show increased mobility, compared to endogenous *WUS*, which might be a result of deregulation and, directly or indirectly, led to the over-proliferation phenotypes observed.

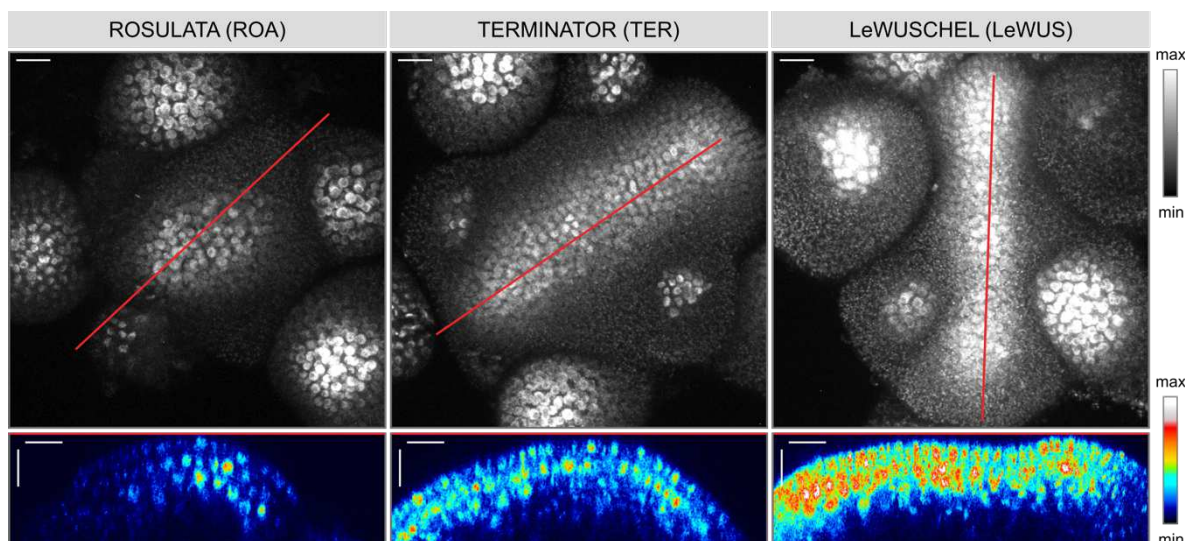


**Figure 19: Visual analysis of proteins conferring the *WUS* function in other species in *Arabidopsis wus* mutant plants.** Plants displayed are T1 plants that were confirmed homozygous *wus* mutants by genotyping. Upper panels show plants from a top-view perspective; lower panels represent a computed side-view slice through the red line indicated in the upper panels. Scale bars represent a length of 15  $\mu\text{m}$ .

### 2.9. Approaches towards deciphering the (temporal) dynamics of WUS mobility

While there are huge gaps in our understanding of the mechanism(s) driving the mobility of WUS in the shoot meristem, even less is known about the time scale of WUS movement, as regular microscopy, including what we consider live-cell imaging, can produce only snapshots of the homeostatic situation. In 2014, Daum and colleagues showed that WUS moves via plasmodesmata (Daum et al., 2014). For this they blocked plasmodesmata via inducible expression of constitutively active CALLOSE SYNTHASE 3 (CalS3m) specifically in the *CLV3* domain of *WUS* rescue plants (GD44). Without induction of CalS3m, WUS mobility is unaffected and WUS protein is found in a wedge-shaped domain encompassing the OC and CZ (Daum et al., 2014). Upon induction of CalS3m in the *CLV3* domain, WUS mobility gets limited and after 8 hours WUS protein can no longer be detected outside of the organizing center (Daum et al., 2014), giving a first hint towards the time scale of WUS protein mobility. Since these 8 hours include transcription and translation of CalS3m, synthesis and deposition of enough callose to reduce plasmodesmata size to the point where WUS passage is prevented and the regular lifespan of WUS protein already in L1 and L2, a more realistic estimate of the time it takes the WUS protein to move from the L3 to the L1 would probably be in the range of 2-4 hours.

Fluorescence recovery after photobleaching (FRAP) is a widely used approach to investigate molecular dynamics. In the SAM however, where live-cell imaging is usually performed from a top-view perspective, resulting in the path of the laser being parallel to the apical-basal axis, passing through all cell layers (L1, L2, L3), a FRAP-like approach including partial bleaching of individual cells or cell layers was previously not possible. My method for side-view imaging of the SAM (Fuchs and Lohmann, 2022), with the path of the laser being perpendicular to the apical-basal axis, on the other hand would allow me to perform partial bleaching of L1 and L2 cells of a fluorescently tagged WUS rescue line (pMF114:

WUS-linker-GFP), while at the same time avoiding bleaching in L3. Subsequent imaging of the same meristem over the course of several hours should then allow me to observe the movement of non-bleached WUS-linker-GFP molecules from the L3 towards L2 and later L1, to replace bleached WUS-linker-GFP molecules reaching the end of their natural lifespan. I figured this approach would enable me to closely investigate the dynamics of WUS mobility *in-vivo* and in the most natural setting, using a single insertion homozygous *WUS* rescue line.

Unfortunately, my first set of proof-of-principle experiments, revealed a number of problems: First, the pMF114 rescue line that I used here, does not contain a suitable nuclear marker. This can complicate the identification of individual cell layers during subsequent analysis in general, but also especially at later time points, due to progressive photobleaching of the whole tissue even without specific bleaching of a ROI. Therefore, I was not able to analyze time points later than 2 hours. Second, specific bleaching of a ROI, encompassing the whole L1 and L2 but not the L3, was neither very precise nor very efficient. In almost all cases, the L3 was partially bleached, with varying degrees of efficiency, but even worse, the L2 was usually also only partially bleached. Notwithstanding the fact that specificity of the bleaching ROI could potentially be improved by recalibrating and aligning the laser, this partial bleaching is again a general problem of tissue curvature: If the crest of the dome representing the L3 is taken as the border for the bleaching ROI, L2 bleaching will become increasingly incomplete with increasing distance from the crest. Trying to compensate for this by moving the border of the bleaching ROI further down along the apical-basal axis of the shoot meristem, will lead to increased L3 bleaching, which is similarly detrimental to the quality of the experiment. These effects will be worse the smaller, and therefore more curved, the meristem is. In any case, incomplete bleaching of a cell layer or even single cells within a layer will severely hamper the power of the experiment as non-bleached protein can

## Results

move into the analysis domain from the side or may stem from within the same cell, obscuring the analysis of layer-to-layer mobility. Generally, the efficiency of bleaching was not very high, and while up to 11 seconds of full exposure to 100% of our 488 nm laser line resulted in clearly visible bleaching, signal intensity was usually only reduced by about 50%. This could potentially be increased by either increasing the output of the laser (meaning that 100% laser power in the software would correspond to a higher light intensity), which however would be incompatible with our other imaging applications, or by prolonging the exposure time, which however would result in increased overall bleaching, likely further shortening the total length of time lapse imaging.

Despite all these difficulties, this proof-of-principle experiment yielded time laps data of two meristems suitable for analysis with the IFNH tool: one dataset with L1 and L2 specific bleaching and one dataset of a non-bleached control. I analyzed both sets of data and normalized fluorescence intensity per meristem to the intensity of the third nucleus at time point 0 hours (or pre-bleach) for comparison. The non-bleached dataset appeared very much as expected: Fluorescence intensity gradually decreased over time within all layers due to photobleaching (Figure 20). Interestingly though, this effect (of the decrease) was small in L1, larger in L2 and even larger in L3, suggesting fluorescently tagged WUS protein had moved from L3 to L2 and L1, compensating for both, the natural turnover of WUS protein as well as fluorescence lost due to bleaching. At the same time, synthesis of WUS-linker-GFP in the OC appeared to have ceased, which is likely why fluorescence intensity in L3 dropped dramatically. The bleached dataset showed initial reduction of fluorescence intensity in L1 and L2 by roughly a half and no reduction in L3, where in fact fluorescence intensity was increased, likely representing inaccuracy of the analysis. Subsequent datapoints for all layers showed an overall decrease of fluorescence intensity in a pattern similar to the non-bleached control, albeit with fluctuations at single time points that

appeared to be asynchronous between layers, again suggesting that the effect might be due to the lack of a nuclear marker for assignment of cell layers. However, unfortunately, I did not see a substantial increase in fluorescence intensity in the L1 as well as in the L2, where non-bleached WUS-linker-GFP protein from the L3 would have moved to first, within the first 2 hours. It is possible that an effect would be visible in a line containing a nuclear marker, which would then allow to get more reliable data from more plants and potentially for a longer period of time. Such a line, for example, could be obtained by crossing the WUS rescue line (pMF114) to CW66 (containing ubiquitously expressed 3xmCherry-NLS), which is the line that I used for transformation of most constructs in this thesis. However, given the added difficulties in complete bleaching of L2 and L1 discussed in the beginning, I decided to not continue with this approach.

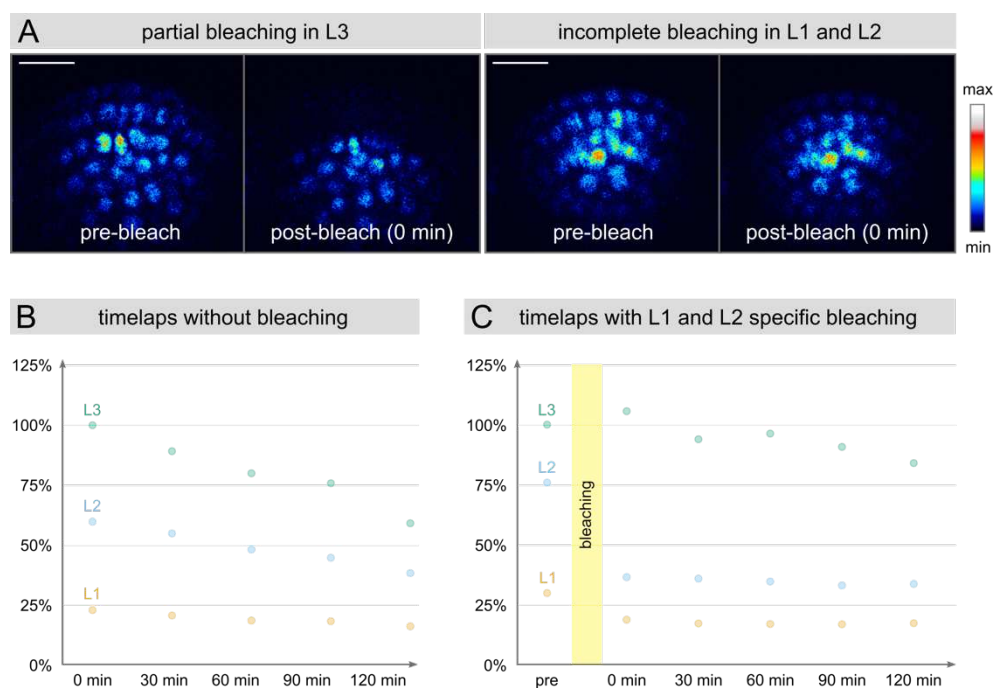


**Figure 20: Bleaching and recovery-of-fluorescence experiments in a WUS-linker-GFP rescue line.** (A) WUS-linker-GFP meristem, imaged and bleached from a side-view perspective, before and immediately after bleaching. Scale bars are valid in horizontal and vertical direction and represent a length of 15  $\mu\text{m}$ . (B) Layer specific relative intensity for WUS-linker-GFP in one meristem over time without bleaching. Signal intensity was normalized to the L3 signal at timepoint 0 min. (C) Layer specific relative intensity for WUS-linker-GFP in one meristem over time with L1-L2 bleaching. Signal intensity was normalized to the L3 signal at timepoint 0 min.

Instead, I aimed to use a fluorescent timer protein (fastFT) (Subach et al., 2009). This protein emits fluorescence within the blue spectrum, but as it matures and time progresses, its

## Results

emission shifts towards the red spectrum. I figured, that by expressing a protein (WUS, WUS $\Delta$ box or MiniMe $\Delta$ box) tagged with linker-fastFT from the *WUS* promoter in the SAM and then calculating the ratio of blue to red for each layer, I would get an impression of the age of the fusion protein within each layer and therefore of its mobility. Unfortunately, I did not get many transgenic plants and those that I got and was able to image did not express the construct(s): I could not observe any nuclear fluorescence in the blue spectrum in the OC, where the protein(s) should have been expressed, and in L1 and L2 I saw only weak fluorescence artifacts, not resembling the localization and behavior of any of the three fluorescent proteins when tagged with GFP or mNeonGreen (data not shown). Due to the complete lack of blue fluorescence in the L3 and considering that the blue detector in the microscope setup that I was using was less sensitive than the green and red detectors I decided to not further try to investigate protein fusions with fastFT.

I then switched my attention to inducible lines: I cloned several alleles, including WUS and WUS $\Delta$ box, tagged with GFP or mNeonGreen, making use of estradiol inducible expression (Zuo et al., 2000) under the control of the *WUS* promoter. I transformed them into CW66 plants, which contain a ubiquitously expressed nuclear marker and are wildtype for the *WUS* locus, selected and grew T1 plants, but due to time limitations were not able to further proceed with characterizing expression of the fusion protein, behavior of the constructs upon induction and establishment of stable lines.

### 3. Discussion

Over the past decades, *WUS* has emerged as one of the key regulators of shoot development: The *WUS* gene encodes an atypical homeodomain transcription factor (Mayer et al., 1998) with bifunctional activity as a transcriptional activator or repressor, depending on the specific cellular context (Mayer et al., 1998; Stuurman et al., 2002; Haecker et al., 2004; Kieffer et al., 2006; Ikeda et al., 2009; Lohmann et al., 2001; Leibfried et al., 2005). *WUS* is a core element of genetic feedback regulation in the shoot meristem (Brand et al., 2002, 2000; Schoof et al., 2000; Lenhard et al., 2001; Lohmann et al., 2001; Schlegel et al., 2021) and is essential for stem cell homeostasis in shoot and floral meristems (Mayer et al., 1998), floral patterning (Lohmann et al., 2001) and ovule development (Groß-Hardt et al., 2002). Its integration in feedback regulation in the SAM and therefore its function as a stem cell maintenance factor is dependent on the ability of the WUS protein to move from cell to cell, from the OC, where the protein is expressed, towards stem cells in the overlying CZ, establishing a protein gradient with decreasing WUS levels from the L3 to the epidermal L1 (Yadav et al., 2011; Daum et al., 2014). Perturbation of the WUS gradient, for example by blocking WUS movement or increasing the amount of protein in the L1, lead to drastic meristematic phenotypes, such as stem cell depletion, partially copying the phenotype of a *wus* null mutant, or stem cell over-proliferation, respectively (Daum et al., 2014).

While the importance of WUS protein mobility to exert WUS-dependent non-cell autonomous maintenance of shoot stem cells, is undisputed, the mechanism behind the formation and maintenance of the WUS gradient in the SAM, including the integration of environmental stimuli, remains controversially debated within the community. Several studies have presented partially conflicting data (discussed in (Fuchs and Lohmann, 2020)), suggesting mechanistic importance of WUS homodimerisation (Daum et al., 2014; Perales et al., 2016; Rodriguez et al., 2016), nuclear-cytoplasmic partitioning with CLV3-dependent

destabilization of the WUS protein (Plong et al., 2021; Rodriguez et al., 2016; Snipes et al., 2018) and protein-protein interactions (Han et al., 2020; Zhou et al., 2018, 2015). These studies have used different fluorescently tagged WUS fusion proteins in live-cell imaging of the shoot meristem, followed by qualitative analysis of the images via visual inspection (Yadav et al., 2011; Daum et al., 2014; Rodriguez et al., 2016) or by analysis via simple image quantifications (Snipes et al., 2018; Plong et al., 2021). However, to date, no systematic comparison between different WUS tagging strategies has been performed and no workflow for reliable, large-scale quantitative analysis, integrated with high-resolution live-cell imaging, has been published.

In this thesis, I chose quantitative approaches to describe the vertical distribution of the WUS gradient in the shoot apical meristem. For this, I developed a workflow for semi-automated layer-specific quantification of signal intensity along the apical-basal axis of the SAM, considering and compensating for the curvature of the tissue. I then compared the vertical distribution of differently tagged WUS fusion proteins in the background of *wus* complementation lines and linked these data to the frequency with which meristematic phenotypes occurred in these lines. To unravel the influence of the tissue on protein mobility, I further analyzed the distribution of transcriptionally non-active WUS variants with different movement capacities and subcellular localization, when expressed from the *WUS* promoter, but also when expressed ‘out-of-context’ from the epidermal *MLI* promoter. I extended these analyses to compare the capacity for protein mobility in the center of the SAM versus the periphery and investigated the hypothesis of potential CLV3-dependent regulation of the WUS gradient. I then characterized the influence of C-terminal domains, implied to be relevant for WUS mobility, and used my quantification workflow to analyze the influence of regulatory sequence stretches in the WUS protein. From these data, I hypothesize that WUS mobility is facilitated via a partially bi-directional, active transport

mechanism that is WUS-specific, likely via the WUS HD, and regulated via protein retention in the L3, likely via protein-protein interactions at the N- and C-terminus as well as in the intrinsically disordered sequence stretch between the WUS HD and WUS box. In the following, I will discuss my findings in comparison to previously published data and in light of recent, unpublished modeling data (not part of this thesis), which was acquired in collaboration with Thomas Stiel, Anna Marciniak-Czochra and Jan Lohmann, based on the quantitative data presented in this thesis.

### 3.1. Comparison of differently tagged WUS alleles in *wus* mutant rescue lines

For a systematic comparison of different WUS rescue alleles, I generated four different protein fusions between WUS and GFP, using N- and C-terminal tagging, with and without the addition of a flexible serine-glycine linker. All fusion proteins were expressed under the control of a 4.4 kb fragment of the *WUS* promoter and a 2.8 kb fragment of the *WUS* terminator and transgene assembly was done using the GreenGate cloning system, which minimizes cloning scars (Lampropoulos et al., 2013). I then used these transgenes to transform heterozygous *wus* mutant plants and generated homozygous, single insertion (T3) rescue lines within a homozygous *wus* mutant background. The resulting four rescue lines, containing GFP-WUS (pMF111), WUS-GFP (pMF112), GFP-linker-WUS (pMF113) and WUS-linker-GFP (pMF114), were then compared with regard to their rescue efficiency and the frequency of meristematic phenotypes as well as *in-vivo* protein distribution in the SAM. Additionally, I compared these lines to a previously published rescue line (GD44: WUS-linker-GFP, using the same 4.4 kb WUS promoter and 2.8 kb WUS terminator fragments, but assembled with Gateway cloning (Daum et al., 2014)). A comparison to another previously published *wus* rescue line (GFP-WUS (Yadav et al., 2011)) was not possible, since this particular line was not available to me.

Visual inspection of fluorescence images and quantification of phenotype frequency revealed no striking differences between pMF111 (GFP-WUS) and pMF114 and GD44 (both WUS-linker-GFP). All fusion proteins displayed a decreasing protein gradient from L3 to L1, qualitatively indistinguishable from previously published images (Daum et al., 2014; Yadav et al., 2011), were strongly nuclear localized and showed low frequency of stem cell depletion phenotypes. In contrast, pMF112 (WUS-GFP) seemed to increase protein mobility, as was evident from a shallower gradient and had a high rate of stem cell depletion and meristem arrest during vegetative development. pMF113 (GFP-linker-WUS) displayed a protein gradient that was even less steep, showed reduced nuclear localization of the fusion protein and a frequency of stem cell depletion and meristem termination at the vegetative stage. From the high rate of meristem termination in pMF112 and pMF113, I conclude that these protein fusions can be considered only partially functional, despite the fact that it was possible to establish stable T3 lines. It seems likely that for pMF112, which is a C-terminal fusion protein without a linker, the addition of the GFP-tag interfered with the function of important protein domains at the WUS C-terminus (potentially: acidic stretch (transcriptional activation), WUS box (transcriptional repression), EAR motif (transcriptional repression)). For pMF113, which is an N-terminal fusion protein with a linker, on the other hand, I would suggest, that the added flexibility (compared to pMF111 (GFP-WUS)) provided by the linker, may have led to interference with the function of the WUS homeodomain. It is noteworthy however, that while both, pMF112 (WUS-GFP) and pMF113 (GFP-linker-WUS), were affected in the same process (stem cell maintenance), the associated phenotype (stem cell depletion and meristem termination) occurred at different developmental stages, allowing to speculate whether the C-terminal domains of the WUS protein and the WUS homeodomain might have different importance during vegetative and reproductive development, respectively.

Quantitative analysis showed that pMF111 (GFP-WUS) as well as pMF114 and GD44 (both WUS-linker-GFP) did not differ significantly in their mobility from L2 to L3. For L2-to-L1 mobility, pMF111 was significantly different from GD44, but both were in turn not significantly different from pMF114. Taken together, these data suggested no critical difference between N-terminally tagged WUS missing a linker (GFP-WUS) and C-terminally tagged WUS with a linker (WUS-linker-GFP), neither on the phenotype level nor in layer-specific protein distribution and both tagging strategies seem equally suited for the analysis of WUS mobility. Additionally, the relatively low mobility of all three fusion proteins, compared to pMF112 (WUS-GFP) and pMF113 (GFP-linker-WUS), seems to contradict the hypothesis that tagging at the C-terminus masks domains important for protein degradation, therefore artificially stabilizing the fusion protein (Rodriguez et al., 2016).

Mobility of pMF112 (WUS-GFP) and pMF113 (GFP-linker-WUS) was increased and protein distribution was shifted towards higher levels of the respective fusion protein in L2 and L1. At the same time, both lines showed stem cell depletion phenotypes, resulting in meristem termination and developmental arrest, which have previously been shown to result from low levels of WUS protein in L2 and L1 following plasmodesmata blocking (Daum et al., 2014). Increased mobility of a functional WUS protein on the other hand, should result in stem cell over-proliferation and excessive meristem growth, rather than meristem termination, as was previously observed for the MiniMe protein, a highly mobile functional WUS variant (Daum et al., 2014). Therefore, I conclude that WUS-GFP and GFP-linker-WUS may represent WUS variants with reduced functionality compared to GFP-WUS and WUS-linker-GFP and that the increased mobility observed here, might represent a mechanism to compensate for reduced protein function by increasing protein levels in L2 and L1.

In general, it needs to be noted that quantitative analysis of WUS distribution revealed high variability between individual plants that was, however, comparable between all rescue lines. Variability did not increase when I analyzed T1 populations, where all plants had different genomic insertion sites and were heterozygous for the transgene, instead of stable, non-segregating T3 lines. Instead, variability increased in deeper layers of the meristem and was generally higher when regarding the L2/L3 (or L3/L2) ratio, compared to the L1/L2 (or L2/L1) ratio. I assume that this is partially due to the fact that the reference points defining the circle that in turn describes SAM curvature are placed at the meristem surface (just above L1) and consequently mirror L1 curvature better than L2 and L3 curvature, meaning that the precision of the layer alignment after polar transformation is bound to decrease with increasing distance from the meristem surface (and with increasing distance from the circle points). Additionally, cells within deeper layers of the SAM are generally less ordered than L2 and L1 cells, which undergo only anticlinal cell division, because of increasing cell sizes and periclinal cell division. However, while these factors explain why variability for L2/L3 (or L3/L2) ratio was bigger than for L1/L2 (or L2/L1) ratio, I think that local differences in growth conditions (light, water, biotic stress) even in plants grown at the same time in the same growth room, the time of day at dissection or imaging (influence of circadian rhythmicity), the length of the time period between dissection and imaging (influence of injury responses) or potentially differences in developmental progression (time after bolting) might account for the high amount in variability. Along these lines, the distribution of mobility ratios and variability of T2 populations was not linked to the mobility of their respective T1 parent plant, but showed the same overall distribution of mobility ratios and variability as the original T1 population (data not shown; data was acquired under my supervision as part of the bachelor thesis of Helena Greifzu). In order to compensate for the overall high variability and to increase the statistical power of my analysis, I switched from

side-view imaging to top-view imaging and pooled data from constructs based on the same protein of interest, allowing for increased sample sizes. At the same time, I decided to quantify T1 populations instead of T3 lines to cover the full extent of natural variability following random insertion of the transgene in the genome without the potential subconscious selection bias introduced by the process of line establishment.

### 3.2. WUS cell-to-cell movement is an active, bi-directional, WUS-specific process

To be able to analyze the influence of tissue context on protein mobility, via comparing the movement of fusion proteins expressed from the *WUS* promoter (upwards mobility) and their mobility when miss-expressed from the epidermal *MLI* promoter (downwards mobility), I used transcriptionally inactivated WUS protein variants with a mutation in the WUS box ( $\Delta$ box) (Ikeda et al., 2009), which according to an earlier study do not move qualitatively different from functional WUS (Daum et al., 2014). The use of inactivated WUS variants is critical to uncouple protein mobility from protein function and from changes in meristem architecture due to altered mobility or miss-expression: Increased levels of functional WUS protein in L1 and L2 of the CZ, for example, resulting from miss-expression or increased mobility, result in ectopic initiation of *CLV3* positive cells and over-proliferation (Ma et al., 2019; Daum et al., 2014). Preventing accumulation of functional WUS in L1 and L2 of the CZ, via blocking of plasmodesmata or targeted degradation of WUS protein in the *CLV3* domain, has the opposite effect, resulting in stem cell depletion and meristem termination (Ma et al., 2019; Daum et al., 2014).

When I expressed several fusion proteins, including *WUS* $\Delta$ box, NES-*WUS* $\Delta$ box, which unlike *WUS* $\Delta$ box is predominantly cytoplasmic, MiniMe $\Delta$ box, which moves excessively to L2 and L1, *WOX13*, a distantly related *WOX* family member that does not contain a WUS box, mirroring the  $\Delta$ box mutation and 2xGFP as well as 2xGFP-NLS, representing non-nuclear and nuclear unspecific diffusion controls, respectively, from the WUS promoter and

from the *ML1* promoter, I found evidence for a partially bi-directional, active, *WUS*-specific transport mechanism in the shoot apical meristem. MiniMe $\Delta$ box protein, expressed under the control of the *WUS* promoter, formed a concentration maximum in the L2, that is outside of its expression domain in L3, which cannot be explained by passive diffusion, but is strongly indicative of active transport. While I could occasionally observe similar protein distribution in the 2xGFP control population, the fraction of plants with a L2/L3 ratio  $> 1$ , was drastically increased in the MiniMe $\Delta$ box population (78% compared to 33%), suggesting that the effect is of biological relevance and not purely a result of potential imaging or analysis artifacts. Additional evidence for active transport comes from the fact that WUS $\Delta$ box, expressed from the *WUS* promoter, showed similar L2-to-L1 mobility as 2xGFP, even though the latter is not distinctly nuclear and, unlike WUS $\Delta$ box and MiniMe $\Delta$ box, is not able to bind chromatin. Consequently, NES-WUS $\Delta$ box, which is also able to bind chromatin, but due to its cytosolic accumulation will have only a small chromatin-bound fraction, showed higher L2-to-L1 mobility compared to WUS $\Delta$ box and 2xGFP, suggesting that it was subject to the same active transport mechanism as WUS $\Delta$ box, MiniMe $\Delta$ box and NES-WUS $\Delta$ box. In contrast, 2xGFP-NLS, which showed strong nuclear localization, but also WOX13, which is able to bind chromatin via its own homeodomain, showed little cell-to-cell mobility, suggesting that active transport in the SAM is a *WUS*-specific process.

Expression of the same set of fusion proteins from the epidermal *ML1* promoter suggested that the hypothesized process of *WUS*-specific, active transport is not limited to upwards movement, but might facilitate downwards mobility as well: WUS $\Delta$ box, MiniMe $\Delta$ box and NES-WUS $\Delta$ box all moved more than 2xGFP, from L1 to L2. The difference in mobility between WUS $\Delta$ box and MiniMe $\Delta$ box was low, which together with a visual analysis of downwards mobility for both proteins, seemed to point towards lower downwards movement

potential compared to upwards movement. Surprisingly, cytoplasmic NES-WUS $\Delta$ box showed higher (L1 to L2) downwards mobility than MiniMe $\Delta$ box, whereas MiniMe $\Delta$ box had shown higher (L3 to L2) upwards mobility. The reason for this difference is not immediately self-evident, but it presents an interesting starting point for speculation: As WUS is a nuclear protein and relies on nuclear localization to bind chromatin and act as a transcription factor, there might be a mechanism in L1 (stem cells) that prevents nuclear WUS, but not cytoplasmic WUS, to leave these cells again. It is also imaginable that there are simply more open chromatin binding sites for WUS in the L1 (stem cells) than in deeper cell layers. While cytoplasmic WUS (NES-WUS $\Delta$ box) would likely not be affected in its mobility, increased chromatin binding for MiniMe $\Delta$ box, as well as WUS $\Delta$ box, would result in a smaller pool of potentially mobile protein at any given time, which could account for lower downwards mobility. For L2-to-L3 mobility, there was no significant difference between WUS $\Delta$ box, MiniMe $\Delta$ box, NES-WUS $\Delta$ box and 2xGFP, which at first seemed to argue against active downwards transport, however, even though the difference was not statistically significant, 2xGFP still showed the lowest mobility. Since the sample size for 2xGFP, expressed from the *ML1* promoter, was small ( $n = 11$ ), it is possible that a larger population might have shown statistically significant differences also for L2-to-L3 mobility. Overall, the data strongly indicated the presence of a mechanism for WUS-specific, active WUS movement in upwards and downwards direction along the apical-basal axis of the shoot meristem.

3.3. WUS specificity of active transport might be mediated via the WUS homeodomain  
Since active transport in the SAM seemed to be WUS specific and did neither apply to 2xGFP nor WOX13, which is a distantly related member of the WOX gene family, sharing little sequence similarity with WUS, both for the overall protein sequence as well as within the homeodomain, and not containing a WUS box, I wondered how this specificity might be

achieved. Having shown that the MiniMe( $\Delta$ box) protein, which is a hybrid protein based on WUS, but has all original WUS sequence except the WUS homeodomain, the (mutated) WUS box and the EAR motif replaced by unspecific linker sequence, also moves via active transport, I figured that specificity of active transport was likely keyed to either the WUS HD, the WUS box or the EAR motif.

A previous paper has shown drastically increased protein mobility, indicated by a clear shift in protein distribution towards L2 and L1, for MiniMe as well as MiniMe $\Delta$ box (Daum et al., 2014). In the same paper, the authors could not observe qualitative differences between functional WUS protein and WUS $\Delta$ box protein, containing a mutation in the WUS box that renders the protein transcriptionally inactive (Daum et al., 2014). My own analysis of the  $\Delta$ box mutation revealed that functional WUS, expressed from the *WUS* promoter in a *wus* mutant rescue line and imaged from a side-view perspective with increased resolution along the apical-basal axis of the SAM, moved less than mutated WUS $\Delta$ box protein, expressed from the *WUS* promoter in wildtype background and imaged from a top-view perspective. This increase in mobility likely results from WUS $\Delta$ box having lost the ability to interact with co-repressors, such as TPL (Kieffer et al., 2006; Long et al., 2006), via the WUS box, since protein-protein interaction with large repressor complexes will increase the fraction of immobile protein. Interestingly, WOX13, which does not contain the WUS box at all, moved a lot less than WUS $\Delta$ box and also less than functional WUS. Taken together, these data – and especially the fact that mutation of the WUS box increased mobility instead of decreasing it – together with previously published data, make it unlikely that specificity of active WUS transport would be mediated via the WUS box.

My comparison of the mobility of WUS $\Delta$ box protein and WUS $\Delta$ box $\Delta$ EAR protein, which carries mutations in the WUS box and the EAR motif, showed no significant difference in vertical distribution. Therefore, I conclude that the EAR motif is also unlikely to mediate the

specificity of active WUS transport, leaving the WUS homeodomain as the remaining candidate. And indeed, I found evidence for this hypothesis in the literature: A protein fusion between the WUS HD and 2xGFP-NLS, was reported to consistently move from the L3 to the L2, unlike 2xGFP-NLS alone, while fusion with the WOX13 homeodomain did not result in a similar increase in mobility (Daum et al., 2014). Additionally, another study has qualitatively compared the mobility of the first 134aa of the WUS protein, including the WUS HD, fused to GFP (here called GFP-WUS\_1-134aa), to the mobility of GFP and NLS-GFP, reporting uniform distribution of all protein in the SAM (Rodriguez et al., 2016). Based on my own visual inspection of the images shown, I tend to disagree with this statement: GFP, expressed from the *WUS* promoter, is indeed uniformly distributed in the meristem. NLS-GFP seems more restricted, which makes sense as nuclear localization of the protein will increase diffusion barriers, but also spreads in the whole SAM. GFP-WUS\_1-134aa, on the other hand, seems to move excessively towards L2 and L1 along the apical-basal axis, but with little spread to the side. And while this data has to be interpreted with caution, due to over-saturation of the image preventing any more quantitative analysis, excessive mobility of GFP-WUS\_1-134aa is reminiscent of the mobility of the MiniMe( $\Delta$ box) protein, as reported in a previous study (Daum et al., 2014), as well as in this thesis. In comparison, a protein fusion of GFP and the C-terminus of WUS (here called GFP-WUS\_229-292), lacking the WUS HD, which Rodriguez and colleagues claim to fully resemble the distribution of full length WUS (Rodriguez et al., 2016), is barely present in L2 and L1, showing little movement potential.

Taken together, I propose that the specificity of active WUS transport might be keyed to the WUS homeodomain, which is distinctly different from all other homeodomains, including the homeodomains of WOX family members, likely via protein-protein interactions.

### 3.4. Regulation of WUS mobility via protein retention in the L3

If WUS mobility was an active transport process rather than undirected diffusion, it stands to reason that this process, that is the formation and maintenance of a stable WUS protein gradient along the apical-basal axis of the shoot meristem, is regulated somehow. In this thesis, I have presented data supporting the hypothesis that WUS mobility was regulated via protein retention in the L3: While WUS $\Delta$ box moved similar to 2xGFP, despite its nuclear localization and the ability to bind chromatin, from the L2 to the L1, from the L1 to the L2 and also from the L2 to the L3, WUS $\Delta$ box mobility from the L3 to the L2 was significantly reduced compared to 2xGFP, suggesting L3-specific reduction in mobility. Along the same line, the mobility difference between functional WUS and WUS $\Delta$ box, caused by protein-protein interactions via the WUS box, was reduced for the L2-to-L1 transition, compared to the L3-to-L2 transition, suggesting additional L3-specific mobility reduction, which unlike protein-protein interactions via the WUS box, would affect the functional as well as the mutated WUS $\Delta$ box protein. Interestingly, the comparison of 2xGFP-NLS and NLS-WUS $\Delta$ box, which moved indistinguishably from L3 to L2, but not from L1 to L2 (with NLS-WUS $\Delta$ box moving more than 2xGFP-NLS) did not only show that active WUS transport was not abolished by the addition of a strong nuclear localization signal, but supported the idea of L3-specific regulation. The same mechanism seemed to regulate the mobility of cytoplasmic WUS (NES-WUS $\Delta$ box), while MiniMe $\Delta$ box and WOX13 were not affected. Since a previous publication had described the presence of mobility restricting sequences in the sequence stretch between the WUS HD and the WUS box (Daum et al., 2014), I created a number of linker substitution alleles to more closely investigate this region of the WUS protein. All these alleles contained only short deletions within the WUS sequence, replaced by a serine-glycine linker of the same length, but otherwise, unlike the more drastic substitutions in the MiniMe proteins, mirrored the WUS $\Delta$ box protein. Additionally, I

investigated the mobility of a MiniMe $\Delta$ box protein, where the N- and C-terminus of the endogenous WUS protein have been reintroduced (N-C-MiniMe $\Delta$ box). However, while some alleles, including N-C-MiniMe $\Delta$ box, showed moderately increased mobility, no single substitution allele was able to reproduce the dramatic MiniMe $\Delta$ box mobility phenotype. Lacking controls to ensure proper folding of the protein, excluding the possibility that any effect on mobility might be a secondary effect rather than specific to the protein sequence replaced, and given the small changes in mobility observed generally, it seems premature to causally link protein mobility with specific sequence stretches or previously known protein-protein interaction domains, such as the HAM binding domain (Zhou et al., 2015) or the WUS homodimerization domain (Busch et al., 2010; Daum et al., 2014; Rodriguez et al., 2016). In any case, two important findings remain from these experiments: First, WUS mobility is not exclusively regulated via the sequence stretch between the WUS HD and the WUS box, but my quantitative analysis suggested the presence of additional regulatory sequence at the N- and C-terminus of the protein, which had not been detected by qualitative analysis in past studies. Second, increased mobility of substitution alleles, indicating loss of regulation, could only be observed for the transition from L3 to L2, but not for L2-to-L1 movement, further indicating that regulation of WUS mobility is a feature of the L3 or even of the OC in particular.

### 3.5. Is WUS mobility CLV3-dependent?

A previous paper has suggested that the maintenance of the WUS gradient was directly dependent on the levels of CLV3 peptide within the stem cells themselves (Plong et al., 2021). In their study, Plong and colleagues have over-expressed a GFP-WUS fusion protein, additionally tagged with the glucocorticoid receptor (GR) at its C-terminus (GFP-WUS-GR) to enable inducible translocation between the cytoplasm and the nucleus, and following external treatment with CLV3 peptide inferred that WUS stability was regulated by CLV3

via nuclear-cytoplasmic partitioning. The use of a C-terminal fusion in this case, especially considering the large size of the GR tag, is surprising, given that previous publications from the same lab have raised concerns about C-terminally tagged WUS variants, which the authors hypothesized to mask important C-terminal domains of the WUS proteins, resulting in artificial stabilization of the fusion protein (Rodriguez et al., 2016; Snipes et al., 2018). Since my own work had shown that C-terminal tagging of the WUS protein was not necessarily detrimental to WUS mobility, I set out to test the hypothesis of CLV3-dependent stabilization of nuclear versus cytoplasmic WUS by comparing the mobility of WUS $\Delta$ box and NES-WUS $\Delta$ box in the central zone of the meristem, where *CLV3* is expressed, versus the surrounding periphery, using my image analysis pipeline for signal quantification. I could, however, not identify any difference in signal identity for WUS $\Delta$ box and NES-WUS $\Delta$ box between CZ and PZ in L1, L2 or L3 and, in my experimental setting, found no evidence for CLV3-dependent stabilization or destabilization of the WUS protein.

3.6. Beyond this thesis: Modelling protein mobility in the SAM based on quantitative data  
Given the complexity of the data, but also the large size of the dataset, I wondered whether computational modeling could add additional facets to my hypothesis for WUS mobility. Therefore, I, together with my supervisor Jan Lohmann, entered a collaboration with Thomas Stiel and Anna Marciniak-Czochra, with whom our lab has already collaborated with in the past to model processes in the shoot apical meristem (Gaillochet et al., 2017; Klawe et al., 2020). Over the course of this collaboration, I provided the quantitative data, Thomas Stiel and Anna Marciniak-Czochra designed, programmed and continuously refined the computational model and Jan Lohman, Thomas Stiel, Anna Marciniak-Czochra and myself discussed the results as well as ideas to improve the model. In the following, I will shortly present a number of key findings of this collaborative effort and will highlight links to the data shown in this thesis.

Since my quantitative analysis generates layer-specific intensity readings by adding up all signal intensity within a disc with a height of one cell and a diameter of 20  $\mu\text{m}$ , resulting in a single intensity value for every cell layer (L1, L2, L3), the data for vertical protein distribution is effectively one-dimensional. Therefore, for the modeling, we decided to follow the same approach and not simulate the shoot meristem in all three dimensions, including multiple cells per layer and horizontal cell-cell connections, but to regard every layer as a single point entity, connected in a linear fashion (L1 connects to L2, but not L3; L2 connects to L1 and L3; L3 connects to L2, but not to L1). We modeled the presence of a cytoplasmic and a nuclear compartment, whose intensity values, however, were summed up to create a single intensity value in the end again, and assumed that only cytoplasmic protein could move, via plasmodesmata, from one cell to another. Interestingly, in this simple setting, the model could only explain the mobility of 2xGFP, moving via passive diffusion, if we either assumed differential degradation rates for every cell layer or if we assumed that the passage from cell to cell did not occur uniformly, but that protein could more easily enter the L2, from both sides (L1 and L3), than exit the L2. Differential degradation of a protein in a layer-specific manner might make sense for WUS and would then point towards a regulatory mechanism, but not for a protein that does not naturally occur in either the tissue or even the species, such as GFP. Additionally, I am not aware of any evidence in the literature, suggesting general differences in protein degradation between meristematic cell layers. In contrast, changes in plasmodesmata aperture have long been implicated to be connected to the developmental status of a tissue (Zambryski, 2004) and recently funnel-shaped plasmodesmata, with different aperture size on one side compared to the other, which could present a means for differential import and export into a cell, have been described (Ross-Elliott et al., 2017). We therefore decided to assume differential layer accessibility via

plasmodesmata, based on 2xGFP data and modeling of 2xGFP diffusion, for further modeling of WUS alleles.

We then started to systematically compare different scenarios and while this is very much work in progress, which I will not go into further detail on as it is also not part of this thesis, so far the model that best mirrors my quantitative data assumes, first, that protein degradation is uniform in the meristem, second, that diffusion and transport rates are identical for WUS $\Delta$ box and MiniMe $\Delta$ box, third, that diffusion and transport rates for 2xGFP are lower by a constant factor, compared to WUS $\Delta$ box and MiniMe $\Delta$ box, and fourth, that protein retention in the L3 can affect WUS $\Delta$ box, but not MiniMe $\Delta$ box or 2xGFP. At the same time, potential effects of protein dimerization are neglected. With this set of assumptions, the model predicts a rate of L3-specific WUS $\Delta$ box protein binding of 16% and finds 2xGFP to have 25% of the mobility (diffusion plus transport) that WUS $\Delta$ box and MiniMe $\Delta$ box possess. These preliminary modeling data support my hypothesis of WUS-specific, bi-directional, active transport, which is regulated via protein retention in the L3.

## 4. Materials and Methods

### 4.1. Molecular Cloning

All constructs created and used in this thesis were cloned using the GreenGate (GG) cloning system (Lampropoulos et al., 2013). GG cloning utilizes type-IIS endonucleases, such as Eco31I, to assemble plant destination vectors in a one-step digestion-ligation reaction by combining inserts with unique 4 bp overhangs (GG-overhangs) from multiple entry vectors in a defined sequential order of modules (e.g., A-module = promoter, B-module = N-terminal tag, C-module = gene of interest, D-module = C-terminal tag, E-module = terminator, F-module = plant resistance gene with independent promoter and terminator) in a destination vector (Z-module).

#### 4.1.1 GG entry vector design

GG entry vectors are based on the pUC19 vector and consist of a backbone carrying an ampicillin resistance gene as well as two Eco31I recognition sites, which flank an insert such that upon endonuclease activity the two recognition sites remain part of the vector backbone. Digestion of the GG entry vector with Eco31I creates two sticky ends at the position of the GG-overhangs, whose sequence is specific to the module-type (e.g., A-module = A-overhang and B-overhang, B-module = B-overhang and C-overhang, etc.) and the insert of the ‘empty’ entry vector containing a chloramphenicol acetyltransferase (caR)-ccdB cassette for negative selection in *ccdB*-sensitive *Eschereschia coli* (*E. coli*), is replaced by the DNA sequence of interest, resulting in a ‘filled’ entry vector that can be used in a GG reaction. Further details with regard to the design of GG entry vectors can be found in the original publication (Lampropoulos et al., 2013).

### 4.1.2 Creation of an entry vector insert via PCR amplification

The majority of GG entry vector inserts created in this thesis was generated via PCR amplification using Phusion High-Fidelity (HF) DNA Polymerase, primers with specifically designed non-binding 5' overhangs (5' end – 4 bp unspecific spacer sequence to enable binding of Eco31I – 6 bp specific Eco31I recognition sequence – 1 bp spacer nucleotide – 4 bp module-specific GG overhang – X bp vector-specific in frame addition: CAACA for C-type entry vector, GT for D-type entry vector – 3' end) and genomic DNA (gDNA), complementary DNA (cDNA) or plasmid DNA from previously cloned vectors as template. For this, 4 µl gDNA (or 4 µl cDNA or 1 µl plasmid DNA) were mixed with 1 µl 10 µM forward primer, 1 µl 10 µM reverse primer, 2 µl dNTPs at a concentration of 2 mM each, 4 µl 5x Phusion HF buffer and 0.2 µl Phusion HF polymerase in a PCR tube. Sterile desalted water (10.8 µl or 7.8 µl) was added to a final reaction volume of 20 µl. PCR was performed in a thermocycler using a standard program with low annealing temperature (98°C for 30 sec, 98°C for 8 sec, 48°C for 20 sec, 72°C for 1 min/kbp, repeat steps 2-4 for 29 times, 72°C for 5 min, 18°C for 10 min). 4 µl 6x loading dye were added to 20 µl reaction volume, which was then loaded onto a 1% agarose gel (1 g agarose, 100 ml 1x TAE buffer, 2.5 µl ethidiumbromide) with 6 µl GeneRuler DNA Ladder Mix being loaded in parallel for size comparison. Gel electrophoresis was performed at 130 V for 30 min after which the relevant DNA band was identified by size and visualized under UV-light, was then cut from the agarose gel and the gel slice was transferred to a 1.5 ml reaction tube for subsequent gel extraction (see 4.1.4).

### 4.1.3 Creation of an entry vector insert via combination of multiple PCR fragments

Inserts for GG entry vectors can be created via amplification of a single PCR fragment or via combining multiple PCR fragments. In this thesis, the latter was used to create non-naturally occurring DNA sequence via amplification from multiple templates or to remove

internal Eco31I sites from genomic or complementary DNA. For this, primers with non-binding 5' overhangs were designed as has been described above (see 4.1.2), making use of Eco31I recognition sites to define customized internal 4 bp overhangs, which after endonuclease activity can be ligated without creating cloning scars. This technique can also be used to introduce mutations to the final PCR product by exchanging single nucleotides within the binding part of the primer, which for example allows for the removal of an internal Eco31I recognition site via a silent mutation.

PCR followed by gel electrophoresis and excision of DNA bands was performed as has been described above (see 4.1.2) and multiple gel slices were pooled in a single 1.5 ml reaction tube for subsequent gel extraction (see 4.1.4).

#### 4.1.4 Purification of DNA fragments from agarose gel

PCR fragments were purified from agarose gel slices using the innuPREP doublePURE Kit from Analytic Jena. For this, the gel was solubilized by incubation with 650  $\mu$ l Gel Solubilizer (included) at 50°C for 10 min or until complete dissolution of the agarose. 50  $\mu$ l Binding Optimizer (included) were added to the sample, which, after mixing, was transferred to a Spin Filter (included) within a 2 ml Receiver Tube (included). It was then centrifuged at 11,000 rcf for 1 min and the filtrate was discarded. Afterwards, the filter was washed twice: 700  $\mu$ l Washing Solution LS (included) were applied onto the filter membrane, the filter was centrifuged at 11,000 rcf for 1 min and the filtrate was discarded. To completely remove Washing Solution LS, the filter was centrifuged at maximum speed for 2 min and was then transferred to a fresh 1.5 ml reaction tube (not included). 19  $\mu$ l Elution Buffer (included), pre-warmed to 50°C, were applied directly onto the filter membrane, followed by incubation at room temperature for 2 min. For final elution of DNA, the Spin Filter was centrifuged at 11,000 rcf for 1 min.

### 4.1.5 Endonuclease digestion of ‘empty’ entry vector (and insert)

Linearization of the GG entry vector and generation of single-stranded GG-overhangs on the vector backbone and the entry vector insert was performed via Eco31I digestion. For this, 16  $\mu$ l purified PCR fragment were mixed with 1  $\mu$ l ‘empty’ vector plasmid DNA, 2  $\mu$ l 10x FastDigest (FD) Buffer and 1  $\mu$ l Eco31I FD in a 1.5 ml reaction tube and were incubated at 37°C for 1 h.

### 4.1.6 Purification of DNA from endonuclease digestion reaction

The endonuclease digestion reaction was then purified using the innuPREP doublePURE Kit from Analytic Jena. For this, 500  $\mu$ l Binding Buffer (included) were added to the digestion reaction, both were mixed on a vortexer and the solution was transferred to a Spin Filter (included) within a 2 ml Receiver Tube (included). It was then centrifuged at 11,000 rcf for 3 min and the filtrate was discarded. The filter was centrifuged again at 11,000 rcf for 2 min and was then transferred to a 1.5 ml reaction tube (not included). 19  $\mu$ l Elution Buffer (included), pre-warmed to 50°C, were applied directly onto the filter membrane, followed by incubation at room temperature for 2 min. For final elution of DNA, the Spin Filter was centrifuged at 11,000 rcf for 1 min.

### 4.1.7 Assembly of a ‘filled’ entry vector

Entry vectors were assembled via ligation of digested vector backbone and insert fragments, both with single-stranded 5’ GG-overhangs. For this, 16  $\mu$ l purified digestion reaction, containing digested ‘empty’ entry vector and digested insert, were mixed with 2  $\mu$ l 10x T4 DNA Ligase Buffer and 2  $\mu$ l 30 U/ $\mu$ l T4 DNA Ligase in a 1.5 ml reaction tube. The ligation reaction was incubated at room temperature for 1 h and was then subjected to heat-inactivation at 70°C for 10 min prior to transformation into bacterial cells (see 4.1.9).

#### 4.1.8 Creation of an entry vector insert via oligo-annealing, digestion and ligation

In rare cases, small inserts (up to 50-70 bp) were cloned via annealing of a pair of partially complementary oligos, which were designed to overlap except for 4 bp at their respective 5'ends, generating single-stranded GG-overhangs without endonuclease digestion. For this, 9  $\mu$ l of each oligo (10 mM) were mixed in a PCR tube and were incubated using a thermocycler (95°C for 5 min, 95°C for 1 min, decrease by 1°C per 1 min until reaching 25°C, 18°C for 5 min). The entry vector (but not the insert) was linearized by mixing 16  $\mu$ l sterile desalted water with 1  $\mu$ l 'empty' vector plasmid DNA, 2  $\mu$ l 10x FastDigest Buffer and 1  $\mu$ l Eco31I FD in a 1.5 ml reaction tube, followed by incubation at 37°C for 1 h. The digestion reaction was purified as has been described above (see 4.1.5) and 16  $\mu$ l purified digested 'empty' entry vector, were mixed with 9  $\mu$ l annealed oligos, 3  $\mu$ l 10x T4 DNA Ligase Buffer and 2  $\mu$ l 30 U/ $\mu$ l T4 DNA Ligase in a 1.5 ml reaction tube. The ligation reaction was incubated at room temperature for 1 h to be subsequently transformed into bacterial cells (see 4.1.9).

#### 4.1.9 Transformation of chemically competent *E. coli*

*In-vivo* amplification of plasmid DNA was performed in chemically competent *Escherichia coli* (*E. coli*) of the strain XL1-Blue MR. For this, an aliquot with 50  $\mu$ l bacterial cells (stored at -80°C) was thawed on ice and 6  $\mu$ l entry vector ligation reaction were added to the tube, which after careful mixing by snipping, was then incubated on ice for 15 min. Afterwards, cells were subjected to heat shock at 42°C for 45 sec, followed by incubation on ice for 2 min. 1,400  $\mu$ l liquid LB medium were added and the cells were allowed to regenerate in a shaking incubator at 37°C for 1 h. After regeneration, 100  $\mu$ l bacterial culture were spread on an ampicillin selection plate using glass beads. The remaining bacterial culture was centrifuged at 3,000 rcf for 3 min and the supernatant was discarded. The bacterial pellet was resuspended in 100  $\mu$ l liquid LB, which were then spread on another selection plate. All

selection plates were incubated at 37°C overnight. The next day, 5 ml cultures of liquid LB containing ampicillin were inoculated with single colonies from the selection plate(s) and were grown in a shaking incubator at 37°C overnight.

### 4.1.10 Isolation of plasmid DNA from bacterial culture

Plasmid DNA was isolated from bacterial liquid culture using the innuPREP Plasmid Mini Kit from Analytic Jena. For this, 2 ml of culture were transferred to a 2 ml reaction tube (not included) and were pelleted by centrifugation at maximum speed for 1 min. The supernatant was discarded and the bacterial pellet was resuspended in 250 µl Resuspension Buffer (included) by pipetting up and down. 250 µl Lysis Buffer (included) were added to the sample, which was carefully mixed by inverting the tube 6-8 times. 350 µl of Neutralization Buffer (included) were added and the sample was again mixed by inverting the tube 6-8 times. Afterwards, it was centrifuged at maximum speed for 8 min and the supernatant was transferred to a Spin Filter (included) in a 2 ml Receiver Tube (included), to be centrifuged at 11,000 rcf for 1 min. The filtrate was discarded and the Spin Filter was washed by adding 500 µl Washing Solution A (included), followed by centrifugation at 11,000 rcf for 1 min after which the filtrate was again discarded. Likewise, a second wash was performed using 700 µl Washing Solution B (included), followed by additional centrifugation at maximum speed for 2 min after discarding the filtrate, to completely remove the washing solution. The Spin Filter was then placed in a new 1.5 ml reaction tube (not included) and 80 µl of Elution Buffer P (included) were applied directly onto the filter membrane, followed by incubation at room temperature for 1 min. For final elution of DNA, the Spin Filter was centrifuged at 11,000 rcf for 1 min.

#### 4.1.11 Validation of cloned entry vector via sequencing

Insert validation of entry vectors was performed via Sanger sequencing using the commercial MWG sequencing service: Inserts of up to 800-900 bp were sequenced in a single reaction from the 5' end using our labs standard sequencing primer A02372. Inserts of up to 1,600-1,800 bp were sequenced in separate reactions from both ends using our labs standard sequencing primers A02372 and A02371. Inserts that were longer than 1,800 bp were sequenced using additional internal primers. For the sequencing reaction, 7.5  $\mu$ l plasmid DNA were mixed with 7.5  $\mu$ l desalted water and 2  $\mu$ l 10 mM sequencing primer in a barcode labelled tube and the sample was submitted to MWG for sequencing.

Analysis of sequencing results was performed using the Basic Local Alignment Search Tool (BLAST) via aligning the results of the sequencing with the target sequence generated *in-silico*. The plasmid miniprep of a validated entry vector was stored at -20°C. For long-term storage of a validated entry vector, *E. coli* bacterial liquid culture was added to 670  $\mu$ l 60% glycerol in a cryo-tube to a final volume of 2 ml, the solution was thoroughly mixed and stored at -80°C.

#### 4.2. GG destination vector design

GG destination vectors are based on the pGreen-IIS vector and consist of a backbone carrying a spectinomycin resistance gene as well as Eco31I sites, which flank an insert such that upon endonuclease activity its recognition sites are removed from the vector backbone. Digestion of the GG entry vector with Eco31I creates two sticky ends at the position of the GG-overhangs (for destination vectors: 5' A-overhang and 3' G-overhang) and the insert of the 'empty' destination vector, containing a chloramphenicol acetyltransferase (caR)-ccdB cassette for negative selection in ccdB-sensitive *Eschereschia coli* (*E. coli*), is replaced by the DNA sequence of interest, resulting in a 'filled' destination vector ready for plant

transformation. Further details with regard to the design of GG destination vectors can be found in the literature (Lampropoulos et al., 2013).

### 4.2.1 Assembly of a destination vector via a one-step digestion-ligation reaction

Plant destination vectors were assembled in a one-step digestion-ligation reaction (GG reaction), combining the inserts of 6 different entry vectors into the destination vector backbone. For this, 2  $\mu\text{l}$  of each entry vector (100 ng/ $\mu\text{l}$ ) were mixed with 2  $\mu\text{l}$  100 ng/ $\mu\text{l}$  'empty' destination vector, 2  $\mu\text{l}$  10x FastDigest Buffer, 2  $\mu\text{l}$  10 mM ATP, 1  $\mu\text{l}$  T4 DNA Ligase (30 U/ $\mu\text{l}$ ) and 1  $\mu\text{l}$  Eco31I FD in a PCR tube. The GG reaction was then performed in a thermocycler using a shorter program (37°C for 1 min, 16°C for 1 min, repeat steps 1-2 for 29 times, 80°C for 5 min, 18°C for 5 min) compared to the original publication (Lampropoulos et al., 2013).

*In-vivo* amplification of plasmid DNA was performed via transformation of chemically competent *E. coli*, as has been described above (see 4.1.9), using 6  $\mu\text{l}$  of GG reaction. Bacterial growth and selection were performed as has been described above (see 4.1.9), using spectinomycin as selective antibiotic. Plasmid DNA was extracted from bacterial culture as described (see 4.1.10).

### 4.2.2 Validation of assembled destination vectors via test-digestion

Validation of assembled destination vectors was performed via digestion with suitable restriction enzymes, followed by gel electrophoresis and analysis of the fragment pattern. For this, 6  $\mu\text{l}$  plasmid DNA were mixed with 11  $\mu\text{l}$  sterile desalted water, 2  $\mu\text{l}$  10x enzyme specific digestion buffer and 1  $\mu\text{l}$  restriction enzyme in a 1.5 ml reaction tube. In case the concentration of plasmid DNA was considerably lower than 100 ng/ $\mu\text{l}$ , 17  $\mu\text{l}$  of plasmid DNA were mixed with 2  $\mu\text{l}$  10x enzyme specific digestion buffer and 1  $\mu\text{l}$  restriction enzyme in a 1.5 ml reaction tube. The digestion reaction was then incubated at 37°C, which is the

temperature optimum for all restriction enzymes used in this thesis, for 1 h. Subsequent analysis via gel electrophoresis was performed as described (see 4.1.2), however, agarose concentration or duration of electrophoresis were changed, if necessary, to take potential differences in fragment size into account. A destination vector was deemed confirmed if independent digestions with two restriction enzymes led to the predicted band pattern. The plasmid miniprep of a validated destination vector was stored at -20°C. For long-term storage of a validated destination vector, *E. coli* bacterial liquid culture was added to 670 µl 60% glycerol in a cryo-tube to a final volume of 2 ml, the solution was thoroughly mixed and stored at -80°C.

#### 4.2.3 Transformation of electrocompetent *Agrobacteria*

For final transformation into plants, GG destination vectors were transformed into electrocompetent *Agrobacterium tumefaciens* of the strain ASE. For this, an aliquot with 50 µl bacterial cells (stored at -80°C) was thawed on ice, 1 µl plasmid DNA was added to the tube and the sample was carefully mixed by snipping. Afterwards, the cells were transferred to a pre-cooled electroporation cuvette and were transformed using the pre-set program Ec1 (1 pulse, 1.8 kV) on a BioRad MicroPulser electroporation machine. 1,400 µl liquid LB were added to the cuvette, the sample was transferred to a 1.5 ml reaction tube and cells were allowed to regenerate in a shaking incubator at 28°C for 2 h. After regeneration, 100 µl bacterial culture were spread on a LB chloramphenicol kanamycin spectinomycin tetracycline (CKST) selection plate using glass beads. The remaining bacterial culture was centrifuged at 3,000 rcf for 3 min, the supernatant was discarded and the pellet was resuspended in 100 µl liquid LB, which was then spread on another CKST selection plate. Selection plates were incubated at 28°C for 48 h. 5 ml liquid LB containing CKST were inoculated with single colonies and were grown in a shaking incubator at 28°C for 48 h.

### 4.2.4 Plasmid validation after transformation in *Agrobacteria*

To ensure that a plasmid transformed in *Agrobacteria* had not been recombined, plasmid DNA was extracted from *Agrobacteria* as described above (see 4.1.10), using 30 µl Elution Buffer P for final elution, re-transformed in *E. coli* and analyzed performing a test-digestion. Transformation of chemically competent *E. coli* was performed as has been described above (see 4.1.9) using 1 µl plasmid DNA isolated from *Agrobacteria* culture. After regeneration, 100 µl bacterial culture were used to directly inoculate a liquid LB spectinomycin overnight-culture. Plasmid DNA was purified from this culture as described (see 4.1.10) and was analyzed via digestion with a suitable restriction enzyme as described (see 4.2.2). Upon validation that the destination vector has not recombined, another glycerol stock was made for long-storage: *Agrobacteria* liquid culture was added to 670 µl 60% glycerol in a cryo-tube to a final volume of 2 ml, the solution was thoroughly mixed and stored at -80°C.

### 4.3. Genotyping

Genotyping was used to assess whether plants originating from a heterozygous *wus-1* mutant line (GK870H12) were either heterozygous or homozygous for the WUS wt or mutant allele.

#### 4.3.1 DNA-extraction from plants

Extraction of genomic DNA for genotyping was done using a modified version of a commonly used protocol for the extraction of plant DNA (Edwards et al., 1991). For this, a young leaf was harvested from the plant and was transferred to a 2 ml reaction tube containing 2 1.7-2.1 mm and 1 2.9-3.5 mm glass beads, which was then immediately frozen in liquid nitrogen. The tissue was mechanically disrupted using a TissueLyser II (Retsch) at 22 Hz for 15 sec and tubes were transferred back to liquid nitrogen immediately. 400 µl Edwards buffer (31.52 g/l Tris-HCl, 9.306 g/l EDTA, 14.61 g/l NaCl, pH adjusted to 8.0 using NaOH/HCl, 5 g/l SDS) were added to the sample which was vigorously mixed on a

vortexer for 5 sec. Subsequent DNA extraction was performed at room temperature: The sample was centrifuged at maximum speed for 5 min after which 300  $\mu$ l supernatant were mixed with 300  $\mu$ l ice-cold 100% 2-propanol in a fresh 1.5 ml reaction tube, followed by incubation for 2 min and centrifugation at maximum speed for 10 min. The supernatant was discarded, the pellet was washed with 700  $\mu$ l 70% ethanol and centrifuged at maximum speed for 5 min, after which the supernatant was again discarded. The DNA pellet was dried at 37°C for 10 min, was then resolved in 50  $\mu$ l sterile desalted water by incubation at 55°C for 20 min and was mixed on a vortexer. Extracted gDNA was kept at -20°C for long-term storage.

#### 4.3.2 Genotyping via PCR amplification

Genotyping (of the *WUS* locus) was performed via two separate PCRs using the JumpStart REDTaq ReadyMix (Sigma Aldrich) on gDNA. The first reaction used a primer pair (A00566, A00317) to amplify a 750 bp fragment specific to the wildtype *WUS* locus; the second reaction used a primer pair (A00319, A00317) to amplify a 250 bp fragment specific to the mutant *wus* locus. For this, 5  $\mu$ l 2x JumpStart REDTaq ReadyMix were mixed with 0.2  $\mu$ l 10  $\mu$ M forward primer, 0.2  $\mu$ l 10  $\mu$ M reverse primer, 0.5  $\mu$ l gDNA and 4.1  $\mu$ l sterile desalted water to a final reaction volume of 10  $\mu$ l. PCR was performed in a thermocycler using the same program for the wt- and the mutant-PCR (94°C for 3 min, 94°C for 30 sec, 57°C for 20 sec, 72°C for 1 min, repeat steps 2-4 for 34 times, 72°C for 3 min, 15°C for 5 min). Both PCRs were combined in the same tube, were loaded onto a 1% agarose gel and were subjected to gel electrophoreses at 130 V for 25 min. 6  $\mu$ l GeneRuler DNA Ladder Mix were loaded onto the gel in parallel for size comparison.

A plant was deemed homozygous for the wildtype *WUS* locus or the mutant *wus* locus if the corresponding PCRs showed a single band at 750 bp or at 250 bp, respectively. If the PCRs showed both bands, the corresponding plant was declared heterozygous.

### 4.4. Plant Cultivation

All plants used in this thesis were of the Col-0 ecotype. Destination vectors were transformed in Col-0 wildtype plants, Col-0 *wus-1* mutant plants (GK870H12), a plant line (CW66) containing a ubiquitously expressed nuclear marker (3xmCherry-NLS) in Col-0 wildtype background (Gaillochet et al., 2017) or a plant line (*wus-red*) containing the same marker in the *wus-1* mutant background. The *wus-1* mutant rescue line GD44 has been described previously (Daum et al., 2014).

#### 4.4.1 General growth conditions

Plants were grown on shelves in growth rooms set to 23°C, 65% relative humidity and long day conditions (16 h light, 8 h darkness). Lighting was provided via red and blue or white light-emitting diodes (LEDs).

#### 4.4.2 Plant transformation via floral dip

*Arabidopsis thaliana* plants were transformed via a modified floral dip protocol (Clough and Bent, 1998). For this, 60 ml liquid LB CKST culture were inoculated with transgenic *Agrobacterium* from a glycerol stock and the culture was grown in a shaking incubator at 28°C for 48 h. The plasmid was again validated by extracting plasmid DNA from 2 ml bacterial culture, re-transformation in *E. coli* followed by a test-digestion as described (see 4.2.2). From the remaining culture, 50 ml were centrifuged at 3,000 rcf for 10 min. The supernatant was discarded and the bacterial pellet was resuspended in *Arabidopsis* transformation solution (2.15 g/l Murashige-Skoog (MS); 100 g/l sucrose; 500 µl/l Silwett® L-77), which was then transferred to a watertight container for subsequent dipping. Turgid plants with ~5-20 cm long stems were dipped into the *Agrobacterium*-solution, fully submerging the shoot apices for 5-10 sec, and were then incubated with reduced light and increased humidity conditions. Single pots were bagged with clear plastic bags to avoid seed cross-

contamination the next day and plants were grown for 4 more weeks before watering was reduced and the plants were allowed to dry.

#### 4.4.3 Selection for transgenic plants

Transgenic plants used in this thesis contained resistance genes against glufosinate-ammonium (Basta<sup>®</sup>) or hygromycin.

#### 4.4.4 Basta selection on soil

Selection of Basta resistant plants was performed directly on soil. For this, seeds were sown on soil, soaked with 20 mg/l Basta-solution and were stratified in darkness at 4°C for 2 d. Afterwards, seeds were allowed to germinate under a clear dome to increase humidity and, starting 6 to 7 days after germination, plants were sprayed with 20 mg/l Basta-solution every 2-3 d for 3-4 times.

#### 4.4.5 Hygromycin selection on plate

Prior to selection on ½ Murashige-Skoog (MS) plates, seeds were surface-sterilized: For this, up to 500 µl seeds were submerged in 2-3 volumes ethanol-detergent solution (70% EtOH, 0.1% Triton<sup>™</sup> X-100), were incubated and were regularly mixed for 5-20 min at room temperature. Afterwards, seeds were pelleted and the supernatant was discarded. The seeds were then washed three times in 2-3 volumes 70% ethanol, were resuspended in 99% ethanol, were poured onto a sterile filter paper in a sterile hood and were allowed to dry.

For hygromycin selection, surface sterilized seeds were sown on hygromycin-containing selection plates (2.15 g/l MS; 0.5 g/l MES; pH adjusted to 5.7; 0.7% phytoagar; 25 ng/l hygromycin added after autoclaving) and were stratified at 4°C in darkness for 2 d. Afterwards, plates were subjected to a light pulse of 6 h and were subsequently incubated in darkness for 3 d, followed by incubation in light, at long day conditions, for another 3 d.

### 4.4.6 Creation of homozygous single-insertion transgenic plant lines

After floral dip of T0 plants, seeds of these plants (T1 seeds) were harvested, sown out and subjected to antibiotic selection to check for the presence of the transgene. Individual resistant (= transgenic) T1 plants were grown and seeds of these plants (T2 seeds) were harvested. ~100 T2 seeds from a single T1 plant were sown out with sufficient spacing between individual seeds, to later allow for easier distinction of single plants, and were again subjected to antibiotic selection. The ratio of resistant to non-resistant plants was calculated and a T1 plant was deemed “single-insertion” if its T2 progeny segregated according to mendelian genetic laws (theoretically: 75% resistant plants, 25% non-resistant plants; in practice 60-75% resistant plants (with 25-40% non-resistant plants) were deemed sufficient). 10 resistant T2 plants - that were the offspring of one T1 plant carrying the transgene as a single-insertion - were propagated and seeds of these plants (T3 seeds) were harvested. ~50 T3 seeds from each T2 plant were sown out and were again subjected to antibiotic selection to identify a T2 plant whose offspring did not segregate for the transgene, meaning that the T2 plant itself was homozygous. One such T3 plant was then propagated and its seeds and all following generations were considered a >T3, homozygous single-insertion line.

In this thesis, homozygous single-insertion lines were created for the different *wus*-rescue variants. Most other experiments were performed on T1-populations to emulate natural variability.

### 4.4.7 WUS rescue assay

Rescue lines containing different WUS fusion proteins were compared with regard to their ability to rescue the *wus* mutant phenotype. For this, single, non-sterilized plant seeds from the different lines and Col-0 wildtype seeds were placed on soil, using a toothpick to ensure adequate spacing between plants. Plants were stratified in darkness at 4°C for 2 d, were afterwards allowed to germinate in increased humidity conditions (covered with a clear

dome for 2 d) and were screened for occurrence of meristematic phenotypes starting 8 d after transfer to light.

#### 4.5. Imaging

For imaging of the SAM, turgid plants with the main inflorescence grown to a length of 2-20 cm were dissected, mounted and imaged as has been described in the literature (Fuchs and Lohmann, 2022). Imaging was then done on a Nikon confocal microscope (Nikon A1) mounted on an upright stand (Eclipse Ni-E upright stand) and equipped with with a water immersion objective (CFI75 Apochromat 25XC W 1300) featuring a long working distance (2 mm), high numerical aperture (1.10) and chromatic aberration correction (visible to near infrared) as well as a 4-channel detector unit including two GaAsP-PMTs (for green and red).

##### 4.5.1 Top-view imaging

High throughput imaging of large T1 populations was performed from a top-view perspective as has been described in the literature (Fuchs and Lohmann, 2022). In brief, floral organs were removed from the shoot apex which was then vertically mounted in a petri dish filled with agarose. Remaining flower primordia were dissected with the help of a hypodermic needle until the shoot meristem was exposed. The sample was then submerged in water and imaged with a water dipping objective.

##### 4.5.2 Side-view imaging

For increased resolution along the apical-basal axis, WUS rescue lines were imaged from a side-view perspective as has been described in the literature (Fuchs and Lohmann, 2022). In brief, floral organs and primordia were removed from a vertically mounted shoot apex as has been described above (see 4.5.1). Then a solid block of agarose containing the sample

was cut, rotated by 90° and fixed in liquid agarose. The now horizontally oriented sample was submerged in water and imaged with a water dipping objective.

### 4.5.3 Imaging conditions

Shoot apices were usually imaged with a final resolution of 0.25 µm per pixel in XY-direction (scan size of 512 x 512 pixels, zoom factor of 4) and a step size of 0.5 µm in Z-direction, moving into the tissue as the scan progressed. For imaging from a top-view perspective, Z-stacks of about 50 µm, starting from 1-2 µm above the L1 surface were generated. For imaging from a side-view perspective, Z-stacks of 60-70 µm, starting from the upwards-facing side of the periphery and going in the direction of the central zone, were acquired. The scan speed was set to 0.5 frames per second (pixel dwell of 4.8 µsec) and imaging was done without averaging. For acquisition requiring multiple channels, sequential scanning was enabled only when strictly necessary: This was only the case when bleed-through from a support-channel (e.g., DAPI staining the cell walls) into the channel of interest (e.g., GFP) was expected, but not when bleed-through from the channel of interest (e.g., GFP) into the support-channel (e.g., FM 4-64, staining the plasma membrane) occurred. The pinhole was set to 16.6 µm and the laser power and the gain were balanced to minimize noise (high laser power, low gain) and at the same time reduce phototoxicity and bleaching during image acquisition (low laser power, high gain). In general, imaging settings (laser power and gain) were set to allow for only a few saturated pixels in the structure of interest, meaning that large clusters of over-saturated pixels, which would interfere with quantitative analysis were avoided.

### 4.6. Data analysis and visualization

Imaging data was analyzed using the Fiji software package (Schindelin et al., 2012). Quantification of the vertical distribution of WUS protein was done using my own custom-

made Fiji plugin, described in this thesis (see 2.1) and included (as code) on the CD attached to this thesis. Boxplots were generated using the PlotsOfData (Postma and Goedhart, 2019) and SuperPlotsOfData (Goedhart, 2021) webtools. Continuous data was plotted using the PlotTwist webtool (Goedhart, 2020). Bar plots were generated using Microsoft® Excel for Mac 2019. Visual appearance of all plots was adjusted with Inkscape (open-source software), without changing the informational content. Statistical analysis was performed via an ANOVA-TukeyHSD statistical test, using a previously published R-script (Schmidt, 2020), or via a two-tailed Student's t-Test with unequal variance in Microsoft® Excel for Mac 2019.



## 5. Bibliography

- Berckmans, B., Kirschner, G., Gerlitz, N., Stadler, R., and Simon, R.** (2020). CLE40 signaling regulates root stem cell fate. *Plant Physiol.* **182**: 1776–1792.
- Brand, U., Fletcher, J.C., Hobe, M., Meyerowitz, E.M., and Simon, R.** (2000). Dependence of stem cell fate in Arabidopsis on a feedback loop regulated by CLV3 activity. *Science* (80- ). **289**: 617–619.
- Brand, U., Grünewald, M., Hobe, M., and Simon, R.** (2002). Regulation of CLV3 expression by two homeobox genes in Arabidopsis. *Plant Physiol.* **129**: 565–575.
- Busch, W. et al.** (2010). Transcriptional control of a plant stem cell niche. *Dev. Cell* **18**: 841–853.
- Clark, S.E., Running, M.P., and Meyerowitz, E.M.** (1993). CLAVATA1, a regulator of meristem and flower development in Arabidopsis. *Development* **119**: 397–418.
- Clark, S.E., Running, M.P., and Meyerowitz, E.M.** (1995). CLAVATA3 is a specific regulator of shoot and floral meristem development affecting the same processes as CLAVATA1. *Development* **121**: 2057–2067.
- Clough, S.J. and Bent, A.F.** (1998). Floral dip: A simplified method for Agrobacterium-mediated transformation of Arabidopsis thaliana. *Plant J.* **16**: 735–743.
- Cui, H., Levesque, M.P., Vernoux, T., Jung, J.W., Paquette, A.J., Gallagher, K.L., Wang, J.Y., Blilou, I., Scheres, B., and Benfey, P.N.** (2007). An evolutionarily conserved mechanism delimiting SHR movement defines a single layer of endodermis in plants. *Science* (80- ). **316**: 421–425.
- Daum, G., Medzihradzky, A., Suzaki, T., and Lohmann, J.U.** (2014). A mechanistic framework for noncell autonomous stem cell induction in Arabidopsis. *Proc. Natl. Acad. Sci. U. S. A.* **111**: 14619–14624.
- Edwards, K., Johnstone, C., and Thompson, C.** (1991). A simple and rapid method for the preparation of plant genomic DNA for PCR analysis. *Nucleic Acids Res.* **19**: 1349.
- Fletcher, J.C.** (1999). Signaling of cell fate decisions by CLAVATA3 in Arabidopsis shoot meristems. *Science* (80- ). **283**: 1911–1914.
- Fuchs, M. and Lohmann, J.U.** (2020). Aiming for the top: non-cell autonomous control of shoot stem cells in Arabidopsis. *J. Plant Res.* **133**: 297–309.
- Fuchs, M. and Lohmann, J.U.** (2022). Multi-Angle In Vivo Imaging of the Arabidopsis thaliana Shoot Apical Meristem (SAM). In *Plasmodesmata: Methods and Protocols*, Y. Benitez-Alfonso and M. Heinlein, eds (Springer US: New York, NY), pp. 427–441.
- Gaillochet, C. et al.** (2017). Control of plant cell fate transitions by transcriptional and hormonal signals. *Elife* **6**: 1–30.
- Gallagher, K.L. and Benfey, P.N.** (2009). Both the conserved GRAS domain and nuclear localization are required for SHORT-ROOT movement. *Plant J.* **57**: 785–797.
- Gallagher, K.L., Paquette, A.J., Nakajima, K., and Benfey, P.N.** (2004). Mechanisms regulating SHORT-ROOT intercellular movement. *Curr. Biol.* **14**: 1847–1851.
- Gehring, W.J., Qian, Y.Q., Billeter, M., Furukubo-Tokunaga, K., Schier, A.F., Resendez-Perez, D., Affolter, M., Otting, G., and Wüthrich, K.** (1994). Homeodomain-DNA recognition. *Cell* **78**: 211–223.
- Goedhart, J.** (2020). PlotTwist: A web app for plotting and annotating continuous data. *PLOS Biol.* **18**: e3000581.
- Goedhart, J.** (2021). SuperPlotsOfData - A web app for the transparent display and quantitative comparison of continuous data from different conditions. *Mol. Biol. Cell* **32**: 470–474.
- Groß-Hardt, R., Lenhard, M., and Laux, T.** (2002). WUSCHEL signaling functions in interregional communication during Arabidopsis ovule development. *Genes Dev.* **16**: 1129–1138.
- Haecker, A., Groß-Hardt, R., Geiges, B., Sarkar, A., Breuninger, H., Herrmann, M., and Laux, T.** (2004). Expression dynamics of WOX genes mark cell fate decisions during early embryonic patterning in Arabidopsis thaliana. *Development* **131**: 657–668.
- Han, H., Yan, A., Li, L., Zhu, Y., Feng, B., Liu, X., and Zhou, Y.** (2020). A signal cascade originated from epidermis defines apical-basal patterning of Arabidopsis shoot apical

- meristems. *Nat. Commun.* **11**: 1214.
- Hiratsu, K., Mitsuda, N., Matsui, K., and Ohme-Takagi, M.** (2004). Identification of the minimal repression domain of SUPERMAN shows that the DLELRL hexapeptide is both necessary and sufficient for repression of transcription in Arabidopsis. *Biochem. Biophys. Res. Commun.* **321**: 172–178.
- Hobe, M., Müller, R., Grünewald, M., Brand, U., and Simon, R.** (2003). Loss of CLE40, a protein functionally equivalent to the stem cell restricting signal CLV3, enhances root waving in Arabidopsis. *Dev. Genes Evol.* **213**: 371–381.
- Ikeda, M., Mitsuda, N., and Ohme-Takagi, M.** (2009). Arabidopsis wuschel is a bifunctional transcription factor that acts as a repressor in stem cell regulation and as an activator in floral patterning. *Plant Cell* **21**: 3493–3505.
- Jackson, D., Veit, B., and Hake, S.** (1994). Expression of maize KNOTTED1 related homeobox genes in the shoot apical meristem predicts patterns of morphogenesis in the vegetative shoot. *Development* **120**: 405–413.
- Kieffer, M., Stern, Y., Cook, H., Clerici, E., Maulbetsch, C., Laux, T., and Davies, B.** (2006). Analysis of the transcription factor WUSCHEL and its functional homologue in Antirrhinum reveals a potential mechanism for their roles in meristem maintenance. *Plant Cell* **18**: 560–573.
- Kim, J.Y., Rim, Y., Wang, J., and Jackson, D.** (2005). A novel cell-to-cell trafficking assay indicates that the KNOX homeodomain is necessary and sufficient for intercellular protein and mRNA trafficking. *Genes Dev.* **19**: 788–793.
- Klawe, F.Z., Stiehl, T., Bastian, P., Gaillochet, C., Lohmann, J.U., and Marciniak-Czochra, A.** (2020). Mathematical modeling of plant cell fate transitions controlled by hormonal signals. *PLoS Comput. Biol.* **16**: 1–21.
- Koizumi, K., Wu, S., MacRae-Crerar, A., and Gallagher, K.L.** (2011). An essential protein that interacts with endosomes and promotes movement of the SHORT-ROOT transcription factor. *Curr. Biol.* **21**: 1559–1564.
- Kragler, F., Monzer, J., Shash, K., Xoconostle-Cázares, B., and Lucas, W.J.** (1998). Cell-to-cell transport of proteins: Requirement for unfolding and characterization of binding to a putative plasmodesmal receptor. *Plant J.* **15**: 367–381.
- Lampropoulos, A., Sutikovic, Z., Wenzl, C., Maegele, I., Lohmann, J.U., and Forner, J.** (2013). GreenGate - A novel, versatile, and efficient cloning system for plant transgenesis. *PLoS One* **8**.
- Landrein, B., Formosa-Jordan, P., Malivert, A., Schuster, C., Melnyk, C.W., Yang, W., Turnbull, C., Meyerowitz, E.M., Locke, J.C.W., and Jönsson, H.** (2018). Nitrate modulates stem cell dynamics in Arabidopsis shoot meristems through cytokinins. *Proc. Natl. Acad. Sci. U. S. A.* **115**: 1382–1387.
- Laux, T., Mayer, K.F.X., Berger, J., and Jürgens, G.** (1996). The WUSCHEL gene is required for shoot and floral meristem integrity in Arabidopsis. *Development* **122**: 87–96.
- Lee, J.Y., Colinas, J., Wang, J.Y., Mace, D., Ohler, U., and Benfey, P.N.** (2006). Transcriptional and posttranscriptional regulation of transcription factor expression in Arabidopsis roots. *Proc. Natl. Acad. Sci. U. S. A.* **103**: 6055–6060.
- Leibfried, A., To, J.P.C., Busch, W., Stehling, S., Kehle, A., Demar, M., Kieber, J.J., and Lohmann, J.U.** (2005). WUSCHEL controls meristem function by direct regulation of cytokinin-inducible response regulators. *Nature* **438**: 1172–1175.
- Lenhard, M., Bohnert, A., Jürgens, G., and Laux, T.** (2001). Termination of stem cell maintenance in Arabidopsis floral meristems by interactions between Wuschel and Agamous. *Cell* **105**: 805–814.
- Lenhard, M., Jürgens, G., and Laux, T.** (2002). The WUSCHEL and SHOOTMERISTEMLESS genes fulfil complementary roles in Arabidopsis shoot meristem regulation. *Development* **129**: 3195–3206.
- Lohmann, J.U., Hong, R.L., Hobe, M., Busch, M.A., Parcy, F., Simon, R., and Weigel, D.** (2001). A molecular link between stem cell regulation and floral patterning in Arabidopsis. *Cell* **105**: 793–803.
- Long, J.A., Ohno, C., Smith, Z.R., and Meyerowitz, E.M.** (2006). TOPLESS regulates apical embryonic fate in Arabidopsis. *Science (80- )*. **312**: 1520–1523.

- Lucas, W.J., Bouché-Pillon, S., Jackson, D.P., Nguyen, L., Baker, L., Ding, B., and Hake, S.** (1995). Selective trafficking of KNOTTED1 homeodomain protein and its mRNA through plasmodesmata. *Science* (80-. ). **270**: 1980–1983.
- Ma, Y. et al.** (2019). WUSCHEL acts as an auxin response rheostat to maintain apical stem cells in *Arabidopsis*. *Nat. Commun.* **10**: 5093.
- Mayer, K.F.X., Schoof, H., Haecker, A., Lenhard, M., Jürgens, G., and Laux, T.** (1998). Role of WUSCHEL in regulating stem cell fate in the *Arabidopsis* shoot meristem. *Cell* **95**: 805–815.
- Meijering, E.H.W., Niessen, W.J., and Viergever, M.A.** (2001). Quantitative evaluation of convolution-based methods for medical image interpolation. *Med. Image Anal.* **5**: 111–126.
- Müller, R., Borghi, L., Kwiatkowska, D., Laufs, P., and Simon, R.** (2006). Dynamic and compensatory responses of *Arabidopsis* shoot and floral to meristems to CLV3 signaling. *Plant Cell* **18**: 1188–1198.
- Nakajima, K., Sena, G., Nawy, T., and Benfey, P.N.** (2001). Intercellular movement of the putative transcription factor SHR in root patterning. *Nature* **413**: 307–311.
- Ohta, M., Matsui, K., Hiratsu, K., Shinshi, H., and Ohme-Takagi, M.** (2001). Repression domains of class II ERF transcriptional repressors share an essential motif for active repression. *Plant Cell* **13**: 1959–1968.
- Perales, M., Rodriguez, K., Snipes, S., Yadav, R.K., Diaz-Mendoza, M., and Reddy, G.V.** (2016). Threshold-dependent transcriptional discrimination underlies stem cell homeostasis. *Proc. Natl. Acad. Sci. U. S. A.* **113**: E6298–E6306.
- Plong, A., Rodriguez, K., Alber, M., Chen, W., and Reddy, G.V.** (2021). CLAVATA3 mediated simultaneous control of transcriptional and post-translational processes provides robustness to the WUSCHEL gradient. *Nat. Commun.* **12**: 1–13.
- Postma, M. and Goedhart, J.** (2019). PlotsOfData—A web app for visualizing data together with their summaries. *PLOS Biol.* **17**: e3000202.
- Ptashne, M.** (1988). How eukaryotic transcriptional activators work. *Nature* **335**: 683–689.
- Reddy, G.V., Heisler, M.G., Ehrhardt, D.W., and Meyerowitz, E.M.** (2004). Real-time lineage analysis reveals oriented cell divisions associated with morphogenesis at the shoot apex of *Arabidopsis thaliana*. *Development* **131**: 4225–4237.
- Rodriguez, K., Perales, M., Snipes, S., Yadav, R.K., Diaz-Mendoza, M., and Reddy, G.V.** (2016). DNA-dependent homodimerization, sub-cellular partitioning, and protein destabilization control WUSCHEL levels and spatial patterning. *Proc. Natl. Acad. Sci. U. S. A.* **113**: E6307–E6315.
- Rojo, E., Sharma, V.K., Kovaleva, V., Raikhel, N. V., and Fletcher, J.C.** (2002). CLV3 is localized to the extracellular space, where it activates the *Arabidopsis* CLAVATA stem cell signaling pathway. *Plant Cell* **14**: 969–977.
- Ross-Elliott, T.J. et al.** (2017). Phloem unloading in *Arabidopsis* roots is convective and regulated by the phloempole pericycle. *Elife* **6**.
- Sakakibara, K. et al.** (2014). WOX13-like genes are required for reprogramming of leaf and protoplast cells into stem cells in the moss *Physcomitrella patens*. *Dev.* **141**: 1660–1670.
- Satina, S., Blakeslee, A.F., and Avery, A.G.** (1940). Demonstration of the Three Germ Layers in the Shoot Apex of *Datura* by Means of Induced Polyploidy in Periclinal Chimeras. *Am. J. Bot.* **27**: 895.
- Schindelin, J. et al.** (2012). Fiji: An open-source platform for biological-image analysis. *Nat. Methods* **9**: 676–682.
- Schlegel, J., Denay, G., Wink, R., Pinto, K.G., Stahl, Y., Schmid, J., Blümke, P., and Simon, R.G.** (2021). Control of *Arabidopsis* shoot stem cell homeostasis by two antagonistic CLE peptide signalling pathways. *Elife* **10**: 1–30.
- Schmidt, V.A.F.** (2020). Polarization of a small GTPase at the plasma membrane of the root hair initiation domain.: 173 Seiten.
- Schoof, H., Lenhard, M., Haecker, A., Mayer, K.F.X., Jürgens, G., and Laux, T.** (2000). The stem cell population of *Arabidopsis* shoot meristems is maintained by a regulatory loop between the CLAVATA and WUSCHEL genes. *Cell* **100**: 635–644.
- Sessions, A., Weigel, D., and Yanofsky, M.F.** (1999). The *Arabidopsis thaliana* MERISTEM

- LAYER 1 promoter specifies epidermal expression in meristems and young primordia. *Plant J.* **20**: 259–263.
- Sloan, J., Hakenjos, J.P., Gebert, M., Ermakova, O., Gumiero, A., Stier, G., Wild, K., Sinning, I., and Lohmann, J.U.** (2020). Structural basis for the complex DNA binding behavior of the plant stem cell regulator WUSCHEL. *Nat. Commun.* **11**: 2223.
- Snipes, S.A., Rodriguez, K., DeVries, A.E., Miyawaki, K.N., Perales, M., Xie, M., and Reddy, G.V.** (2018). Cytokinin stabilizes WUSCHEL by acting on the protein domains required for nuclear enrichment and transcription. *PLoS Genet.* **14**: e1007351.
- Stahl, Y. et al.** (2013). Moderation of arabidopsis root stemness by CLAVATA1 and ARABIDOPSIS CRINKLY4 receptor kinase complexes. *Curr. Biol.* **23**: 362–371.
- Stahl, Y., Wink, R.H., Ingram, G.C., and Simon, R.** (2009). A Signaling Module Controlling the Stem Cell Niche in Arabidopsis Root Meristems. *Curr. Biol.* **19**: 909–914.
- Stewart, R.N. and Burk, L.G.** (1970). Independence of Tissues Derived from Apical Layers in Ontogeny of the Tobacco Leaf and Ovary. *Am. J. Bot.* **57**: 1010.
- Stuurman, J., Jäggi, F., and Kuhlemeier, C.** (2002). Shoot meristem maintenance is controlled by a GRAS-gene mediated signal from differentiating cells. *Genes Dev.* **16**: 2213–2218.
- Subach, F. V., Subach, O.M., Gundorov, I.S., Morozova, K.S., Piatkevich, K.D., Cuervo, A.M., and Verkhusha, V. V** (2009). Monomeric fluorescent timers that change color from blue to red report on cellular trafficking. *Nat. Chem. Biol.* **5**: 118–126.
- Tiwari, S.B., Hagen, G., and Guilfoyle, T.J.** (2004). Aux/IAA Proteins Contain a Potent Transcriptional Repression Domain. *Plant Cell* **16**: 533–543.
- Vatén, A. et al.** (2011). Callose Biosynthesis Regulates Symplastic Trafficking during Root Development. *Dev. Cell* **21**: 1144–1155.
- Xu, X.M., Wang, J., Xuan, Z., Goldshmidt, A., Borrill, P.G.M., Hariharan, N., Kim, J.Y., and Jackson, D.** (2011). Chaperonins facilitate KNOTTED1 cell-to-cell trafficking and stem cell function. *Science* (80-. ). **333**: 1141–1144.
- Yadav, R.K., Perales, M., Gruel, J., Girke, T., Jönsson, H., and Venugopala Reddy, G.** (2011). WUSCHEL protein movement mediates stem cell homeostasis in the Arabidopsis shoot apex. *Genes Dev.* **25**: 2025–2030.
- Zambryski, P.** (2004). Cell-to-cell transport of proteins and fluorescent tracers via plasmodesmata during plant development. *J. Cell Biol.* **164**: 165–168.
- Zhang, L., Gennaro, D. De, Lin, G., Chai, J., and Shpak, E.D.** (2021). ERECTA family signaling constrains CLAVATA3 and WUSCHEL to the center of the shoot apical meristem. *Development* **148**.
- Zhou, Y., Liu, X., Engstrom, E.M., Nimchuk, Z.L., Pruneda-Paz, J.L., Tarr, P.T., Yan, A., Kay, S.A., and Meyerowitz, E.M.** (2015). Control of plant stem cell function by conserved interacting transcriptional regulators. *Nature* **517**: 377–380.
- Zhou, Y., Yan, A., Han, H., Li, T., Geng, Y., Liu, X., and Meyerowitz, E.M.** (2018). Hairy meristem with wuschel confines clavata3 expression to the outer apical meristem layers. *Science* (80-. ). **361**: 502–506.
- Zuo, J., Niu, Q.W., and Chua, N.H.** (2000). Technical advance: An estrogen receptor-based transactivator XVE mediates highly inducible gene expression in transgenic plants. *Plant J.* **24**: 265–273.

## 6. Appendix

### 6.1. List of figures

**Figure 1: The shoot apical meristem (SAM) of *Arabidopsis thaliana*.** (Figure modified from my own review article (Fuchs and Lohmann, 2020); original figure concept, design and creation were done by myself.) (A) Schematic representation of the shoot apical meristem at the tip of the *Arabidopsis* shoot and of functional domains within the SAM. (B) Schematic representation of clonally distinct cell layers in the SAM. L1 and L2 originate from anticlinal cell divisions while cells in the L3 arise from anticlinal and periclinal divisions. 16

**Figure 2: Localization of key stem cell regulators in the SAM.** (Figure modified from my own review article (Fuchs and Lohmann, 2020); original figure concept, design and creation were done by myself.) (A) Schematic representation of the *CLV3* (red) and *WUS* (blue) mRNA expression domains. Note the overlap in the L3 (purple). (B) Confocal slice through the center of a *pCLV3* (red), *pWUS* (blue) and *pUBQ10* (gray) triple reporter SAM. The scale bar represents a length of 15  $\mu\text{m}$ . (C) Schematic representation of WUS protein localization (intensity coded in blue). (D) Confocal slice through the center of a *pWUS::WUS-linker-GFP* (GD44) rescue SAM. GFP was color coded on a linear scale. The scale bar represents a length of 15  $\mu\text{m}$ . 20

**Figure 3: Tissue curvature of the SAM complicates quantitative analysis.** Schematic representation of the shoot apical meristem (SAM) with distinct cell layers (L1, L2, L3) highlighted. Quantification of fluorescence intensity from micrographs in the SAM is complicated by the overlap between individual cell layers due to tissue curvature. Polar transformation of images, based on circle points recapitulating meristem curvature, can align cell that belong to the same cell layer and reduce overlap. 27

**Figure 4: The IFNH tool performs semi-automated alignment of meristematic cell layers, followed by layer specific intensity measurement.** Images in this workflow example are real data: The meristem depicted was imaged from a side-view perspective, did not contain a nuclear support channel and automated, threshold-based selection of the analysis domain was used. Horizontal and vertical scale bars represent a length of 15  $\mu\text{m}$ . All images use the 'HiLo' LUT, where blue color represents pixels with a value of zero. (A) Image stack of a SAM, imaged from a side-view perspective, with the curved outer surface of the meristem oriented upwards. (B) Maximum projection of (A) after rotation of the stack. This image is used for automated, threshold-based selection of the analysis domain. (C) Side-view image stack with reduced stack depth (Z-dimension), based on (B) to encompass only the analysis domain. This image stack is used for the selection of circle points later used for polar transformation. (D) Side-view image stack with reduced stack depth (Z-dimension), based on (B). Additionally, pixels outside the analysis domain in X-dimension, based on (B) have been set to 0. Y-dimension has been reduced by setting pixels to 0, based on circle points and the circle center point (C). (E) Side-view image stack, based on (D) after polar transformation using the center point of the circle defined in (C) as a pole. (F) Sum projection of (E). This image contains all information on signal intensity from (D) and (E), but represents a reduction from 3D to 2D. (G) 1D representation of (F) after rotation and sum projection. All information on signal intensity (within a specified analysis domain, along the apical-basal axis of the SAM) has been compressed from 3D to 1D and can be plotted in a line plot. The line plot is then used to define the borders between adjacent cell layers. (H) 2D representation, equivalent to (E), containing layer specific ROIs for intensity measurement, based on (G). (I) Layer specific intensity (for L1, L2, L3) within a specific analysis domain. Fluorescence intensity was measure in (H), based on the borders defined in (G). 34

**Figure 5: Different tagging strategies for WUSCHEL (WUS).** Schematic representation of the different tagging strategies for WUS, tested in this thesis. WUS was tagged with green fluorescent protein (GFP) at the N-terminus or C-terminus, with and without the addition of a flexible serine-glycine linker.

Known protein domains important for WUS transcriptional activity, their relative position in the WUS protein and their main function are highlighted. 37

**Figure 6: Live-cell imaging of *WUS* rescue lines to compare different *WUS* tagging strategies.**

Micrographs of single-insertion homozygous *WUS* rescue lines (T3 or higher). Images have been acquired from a side-view perspective to increase imaging resolution along the apical-basal axis. Scale bars are valid in horizontal and vertical dimension and represent a length of 15  $\mu\text{m}$ . 38

**Figure 7: Quantitative analysis of vertical protein distribution of fluorescently tagged *WUS* protein in *WUS* rescue lines.**

Vertical distribution in the SAM is displayed as the ratio between L2 and L3, signifying mobility from L3 to L2, and as the ratio between L1 and L2, signifying mobility from L2 to L1. Individual data points represent individual plants. The red data points represent the individuals shown in Figure 6. The median of each population is indicated by a black bar, together with the 95% confidence interval. The mean of each population is indicated by a black X. The sample size is indicated in gray numbers below each population. The results of an ANOVA-Tukey HSD statistical test (significance value = 0.01; same letters indicate no statistically significant difference) are shown above each population. 40

**Figure 8: Comparison of the frequency of meristematic phenotypes in *WUS* rescue lines.**

(A) Vegetative termination phenotype versus unaffected plants in pMF112 (*WUS*-GFP rescue line): Affected plants produce a small number of leaves before the shoot meristem terminates and development is arrested. Subsequent growth results in the growth of atypical tissues. Scale bars represent a length of 2 mm. The bottom images represent a zoom of the top images, as highlighted by the gray boxes. (B) Reproductive termination phenotype versus unaffected plants in pMF113 (GFP-linker-*WUS* rescue line): Affected plants develop normally during vegetative development, but terminate the shoot meristem after growth of a small number of floral organs. No further organs are produced, but organs grown prior to termination develop normally. Scale bars represent a length of 2 mm. The bottom images represent a zoom of the top images, as highlighted by the gray boxes. (C) Quantification of the frequency of meristematic phenotypes occurring in pMF111 (GFP-*WUS*), pMF112 (*WUS*-GFP), pMF113 (GFP-linker-*WUS*), pMF114 (*WUS*-linker-GFP) and GD44 (*WUS*-linker-GFP) in comparison to the wildtype control Col-0 (wt). 41

**Figure 9: Quantification of potential differences in signal distribution between different alleles for the same protein of interest.**

Quantitative analysis of the vertical distribution of different alleles of *WUS* $\Delta$ box-linker-FP, expressed from the *WUS* promoter. Alleles differ in the fluorophore used (GFP or mNeonGreen), the plant resistance (hygromycin resistance (Hyg-R) or glufosinate ammonium (Basta-R)) or the plant destination vector (pGGZ001 or pGGZ003). Vertical distribution in the SAM is displayed as the ratio between L2 and L3, signifying mobility from L3 to L2, and as the ratio between L1 and L2, signifying mobility from L2 to L1. Individual data points represent individual plants. The median of each population is indicated by a black bar, together with the 95% confidence interval. The sample size is indicated in gray numbers below each population. The results of an ANOVA-Tukey HSD statistical test (significance value = 0.01; same letters indicate no statistically significant difference) are shown above each population. 44

**Figure 10: Live-cell imaging of fusion proteins expressed from the *WUS* promoter to analyze upwards mobility.**

Micrographs of fusion proteins (T1) in Col-0 wildtype plants, containing a genetically encoded, ubiquitous nuclear marker (T3 or higher). Images have been acquired from a top-view perspective. Horizontal and vertical scale bars represent a length of 15  $\mu\text{m}$ . White arrowheads point towards low abundantly 2xGFP-NLS protein in individual L2 cells. 47

**Figure 11: Quantification of fusion proteins expressed from the *WUS* promoter to analyze upwards mobility.**

Vertical distribution in the SAM is displayed as the ratio between L2 and L3, signifying

mobility from L3 to L2, and as the ratio between L1 and L2, signifying mobility from L2 to L1. Individual data points represent individual plants; different colors for data points represent different constructs carrying the same protein of interest. The median of each population is indicated by a black bar, together with the 95% confidence interval. The sample size is indicated in gray numbers below each population. The results of an ANOVA-Tukey HSD statistical test (significance value = 0.01; same letters indicate no statistically significant difference) are shown above each population. The WUS $\Delta$ box dataset was already shown in Figure 9. **49**

**Figure 12: Live-cell imaging of fusion proteins expressed from the *MLI* promoter to analyze downwards mobility.** Micrographs of fusion proteins (T1) in Col-0 wildtype plants, containing a genetically encoded, ubiquitous nuclear marker (T3 or higher). Images have been acquired from a top-view perspective. Horizontal and vertical scale bars represent a length of 15  $\mu$ m. **50**

**Figure 13: Quantification of fusion proteins expressed from the *MLI* promoter to analyze downwards mobility.** Vertical distribution in the SAM is displayed as the ratio between L2 and L1, signifying mobility from L1 to L2, and as the ratio between L3 and L2, signifying mobility from L2 to L3. Individual data points represent individual plants; different colors for data points represent different constructs carrying the same protein of interest. The median of each population is indicated by a black bar, together with the 95% confidence interval. The sample size is indicated in gray numbers below each population. The results of an ANOVA-Tukey HSD statistical test (significance value = 0.01; same letters indicate no statistically significant difference) are shown above each population. **51**

**Figure 14: Quantification of fusion proteins expressed from the *MLI* promoter to analyze downwards mobility in the central zone (CZ) compared to the peripheral zone (PZ).** Representation of the analysis domains for the CZ and PZ in the shoot meristem from a top-view perspective. Vertical distribution in the SAM is displayed as the ratio between L2 and L1, signifying mobility from L1 to L2, and as the ratio between L3 and L2, signifying mobility from L2 to L3. Individual data points represent individual plants; green data points represent analysis in the CZ and purple data points represent analysis in the PZ. The median of each population is indicated by a black bar, together with the 95% confidence interval. The sample size is indicated in gray numbers below each population. The results of a two-tailed Student's t-Test with unequal variance (significance value = 0.05; n.s. = no statistically significant difference) are shown above each population. The WUS $\Delta$ box CZ, NES-WUS $\Delta$ box CZ, MiniMe $\Delta$ box CZ, WOX13 CZ and 2xGFP CZ datasets were already shown in Figure 13. **53**

**Figure 15: Quantitative comparison of the signal intensity of nuclear (WUS $\Delta$ box) and cytoplasmic (NES-WUS $\Delta$ box) WUS expressed from the *MLI* promoter in the CZ (high levels of *CLV3*) compared to the PZ (lower levels of *CVLV3*).** Signal intensity of a transcriptional *CLV3* reporter in CZ and PZ in the shoot meristem from a top-view perspective. Signal intensity of WUS $\Delta$ box and NES-WUS $\Delta$ box translational reporters is normalized to the area of the analysis domain. Individual data points represent individual plants; green data points represent analysis in the CZ and purple data points represent analysis in the PZ. The median of each population is indicated by a black bar, together with the 95% confidence interval. The sample size is indicated in gray numbers below each population. The results of a two-tailed Student's t-Test with unequal variance (significance value = 0.05; n.s. = no statistically significant difference) are shown above each population. **54**

**Figure 16: Analysis of conserved domains at the WUS C-terminus.** Visual comparison of WUS-linker-GFP (T3 rescue line, imaged from a side-view perspective) and WUS $\Delta$ box, WUS $\Delta$ box $\Delta$ EAR and WOX13 (T1 in wt background, imaged from a top-view perspective) expressed from the *WUS* promoter. Scale bars represent a length of 15  $\mu$ m. Vertical distribution in the SAM is displayed as the ratio between L2 and L3, signifying mobility from L3 to L2, and as the ratio between L1 and L2, signifying mobility from L2 to L1. Individual data points represent individual plants; different colors for data points represent different constructs carrying the same protein of interest. The median of each

population is indicated by a black bar, together with the 95% confidence interval. The sample size is indicated in gray numbers below each population. The results of an ANOVA-Tukey HSD statistical test (significance value = 0.01; same letters indicate no statistically significant difference) are shown above each population. The WUS $\Delta$ box dataset was already shown in Figure 9 and Figure 11. The WUS(-linker-GFP) dataset was already shown in Figure 7. The WOX13 dataset was already shown in Figure 11. 57

**Figure 17: Analysis of the effects of a strong nuclear localization signal (NLS) on protein mobility.**

Visual comparison of 2xGFP-NLS and NLS-WUS $\Delta$ box(-linker-FP) expressed from the *WUS* promoter and the *ML1* promoter. Scale bars represent a length of 15  $\mu$ m. Vertical distribution in the SAM is displayed as the ratio between L2 and L3, signifying (upwards) mobility from L3 to L2, and as the ratio between L2 and L1, signifying (downwards) mobility from L1 to L2. Individual data points represent individual plants; different colors for data points represent different constructs carrying the same protein of interest. The median of each population is indicated by a black bar, together with the 95% confidence interval. The sample size is indicated in gray numbers below each population. The results of an ANOVA-Tukey HSD statistical test (significance value = 0.01; same letters indicate no statistically significant difference) are shown above each population. The 2xGFP-NLS datasets were already shown in Figure 11 and Figure 13. 58

**Figure 18: Quantification of the mobility of linker-scanning alleles expressed from the *WUS* promoter.**

Vertical distribution in the SAM is displayed as the ratio between L2 and L3, signifying mobility from L3 to L2, and as the ratio between L1 and L2, signifying mobility from L2 to L1. Individual data points represent individual plants; different colors for data points represent different constructs carrying the same protein of interest. The median of each population is indicated by a black bar, together with the 95% confidence interval. Blue and red lines represent the median ratios of previously shown WUS $\Delta$ box and MiniMe $\Delta$ box populations. The sample size is indicated in gray numbers below each population. The results of an ANOVA-Tukey HSD statistical test (significance value = 0.01; same letters indicate no statistically significant difference) are shown above each population. 59

**Figure 19: Visual analysis of proteins conferring the *WUS* function in other species in *Arabidopsis wus* mutant plants.**

Plants displayed are T1 plants that were confirmed homozygous *wus* mutants by genotyping. Upper panels show plants from a top-view perspective; lower panels represent a computed side-view slice through the red line indicated in the upper panels. Scale bars represent a length of 15  $\mu$ m. 63

**Figure 20: Bleaching and recovery-of-fluorescence experiments in a WUS-linker-GFP rescue line. (A)**

WUS-linker-GFP meristem, imaged and bleached from a side-view perspective, before and immediately after bleaching. Scale bars are valid in horizontal and vertical direction and represent a length of 15  $\mu$ m. **(B)** Layer specific relative intensity for WUS-linker-GFP in one meristem over time without bleaching. Signal intensity was normalized to the L3 signal at timepoint 0 min. **(C)** Layer specific relative intensity for WUS-linker-GFP in one meristem over time with L1-L2 bleaching. Signal intensity was normalized to the L3 signal at timepoint 0 min. 67

## 6.2. List of all entry vectors

The following table contains all entry vectors that were created for the WUS mobility project over the course of this thesis. Vectors were cloned as has been described above (see 4.1.1, following).

Entry vector	Content	Oligos	Template	Backbone	E. coli glycerol stock
pGGA052	MIOX2 (At2g19800) promoter	A06143 + A05188	plasmid from Raimund Tenhakens lab	pGGA000	XL1 Blue MR; 12.08.2016
pGGB052	WUS	A05901 + A05902	pGGC001	pGGB000	XL1 Blue MR; 09.05.2016
pGGB053	WUS $\Delta$ box	A05901 + A05903; A05904 + A05902	pGGC001	pGGB000	XL1 Blue MR; 09.05.2016
pGGB054	wus7	A05901 + A05906; A05907 + A05902	pGGC001	pGGB000	XL1 Blue MR; 10.05.2016
pGGB055	wus7 $\Delta$ box	A05901 + A05903; A05904 + A05902	pGGB054	pGGB000	XL1 Blue MR; 17.05.2016
pGGB059	<b>Dex-induction</b> module: B-dummy : GR-LhG4 : D-dummy :: <b>tRBCS</b> : FH-adapter with insulator _ HA-adapter : 6xOP :: B-dummy	A06233 + A06234	GG-like reaction of pGGB003 + pGGC018 + pGGD017 + pGGE001 + pGGG006 + pGGG002 + pGGA016	pGGB000	XL1 Blue MR; 23.09.2016
pGGB060	mNeonGreen-linker	A06256 + A06257; A06258 + A06259	pGGD046; pGGB022	pGGB000	XL1 Blue MR; 18.10.2016
pGGB061	GFP (A206K)-linker (different from pGGB025)	A06256 + A06257; A06258 + A06259	pGGD045; pGGB022	pGGB000	XL1 Blue MR; 20.10.2016
pGGB063	MiniMe	A06859 + A05902	pGGC203	pGGB000	XL1 Blue MR; 10.11.2016
pGGB064	WOX13	A06860 + A06861	pGGC230	pGGB000	XL1 Blue MR; 10.11.2016
pGGB065	N-C-MiniMe $\Delta$ box	A05901 + A5902	pGGC251	pGGB000	XL1 Blue MR; 10.11.2016
pGGC180	WUS (with Kozak sequence)	A05916 + A02230	pGGB052	pGGC000	XL1 Blue MR; 17.05.2016
pGGC181	WUS $\Delta$ box	A05916 + A02230	pGGB053	pGGC000	XL1 Blue MR; 17.05.2016
pGGC182	wus7	A05916 + A02230	pGGB054	pGGC000	XL1 Blue MR; 17.05.2016
pGGC183	wus7 $\Delta$ box	A05916 + A02230	pGGB055	pGGC000	XL1 Blue MR; 20.05.2016
pGGC184	WUS del1 (298-348bp replaced by GS-linker)	A05916 + A05943; A05944 + A02230	pGGC180	pGGC000	XL1 Blue MR; 30.05.2016
pGGC185	WUS del2 (349-399bp replaced by GS-linker)	A05916 + A05945; A05946 + A02230	pGGC180	pGGC000	XL1 Blue MR; 27.05.2016
pGGC186	WUS del3 (400-450bp replaced by GS-linker)	A05916 + A05947; A05948 + A02230	pGGC180	pGGC000	XL1 Blue MR; 27.05.2016
pGGC187	WUS del4 (451-501bp replaced by GS-linker)	A05916 + A05949; A05950 + A02230	pGGC180	pGGC000	XL1 Blue MR; 27.05.2016
pGGC188	WUS del5 (502-552bp replaced by GS-linker)	A05916 + A05953; A05954 + A02230	pGGC180	pGGC000	XL1 Blue MR; 30.05.2016
pGGC189	WUS del6 (553-603bp replaced by GS-linker)	A05916 + A05955; A05956 + A02230	pGGC180	pGGC000	XL1 Blue MR; 27.05.2016
pGGC190	WUS del7 (604-654bp replaced by GS-linker)	A05916 + A05957; A05958 + A02230	pGGC180	pGGC000	XL1 Blue MR; 27.05.2016
pGGC191	WUS del8 (655-705bp replaced by GS-linker)	A05916 + A05959; A05960 + A02230	pGGC180	pGGC000	XL1 Blue MR; 27.05.2016
pGGC192	WUS del9 (709-759bp replaced by GS-linker)	A05916 + A05961; A05962 + A02230	pGGC180	pGGC000	XL1 Blue MR; 07.06.2016

## Appendix

Entry vector	Content	Oligos	Template	Backbone	E. coli glycerol stock
pGGC193	WUS del1 (298-348bp replaced by GS-linker), Δbox	A05901 + A05903; A05904 + A05902	pGGC184	pGGC000	XL1 Blue MR; 08.06.2016
pGGC194	WUS del2 (349-399bp replaced by GS-linker), Δbox	A05901 + A05903; A05904 + A05902	pGGC185	pGGC000	XL1 Blue MR; 07.06.2016
pGGC195	WUS del3 (400-450bp replaced by GS-linker), Δbox	A05901 + A05903; A05904 + A05902	pGGC186	pGGC000	XL1 Blue MR; 08.06.2016
pGGC196	WUS del4 (451-501bp replaced by GS-linker), Δbox	A05901 + A05903; A05904 + A05902	pGGC187	pGGC000	XL1 Blue MR; 08.06.2016
pGGC197	WUS del5 (502-552bp replaced by GS-linker), Δbox	A05901 + A05903; A05904 + A05902	pGGC188	pGGC000	XL1 Blue MR; 07.06.2016
pGGC198	WUS del6 (553-603bp replaced by GS-linker), Δbox	A05901 + A05903; A05904 + A05902	pGGC189	pGGC000	XL1 Blue MR; 07.06.2016
pGGC199	WUS del7 (604-654bp replaced by GS-linker), Δbox	A05901 + A05903; A05904 + A05902	pGGC190	pGGC000	XL1 Blue MR; 20.06.2016
pGGC200	WUS del8 (655-705bp replaced by GS-linker), Δbox	A05901 + A05903; A05904 + A05902	pGGC191	pGGC000	XL1 Blue MR; 07.06.2016
pGGC201	WUS del9 (709-759bp replaced by GS-linker), Δbox	A05916 + A05961; A06010 + A02230	pGGC180	pGGC000	XL1 Blue MR; 27.05.2016
pGGC202	MiniMe	A05979 + A02230	pGD133	pGGC000	XL1 Blue MR; 30.05.2016
pGGC203	MiniMeΔbox	A05979 + A02230	pGD344	pGGC000	XL1 Blue MR; 30.05.2016
pGGC204	wus7-MiniMe	A05979 + A05906; A05907 + A02230	pGGC202	pGGC000	XL1 Blue MR; 07.06.2016
pGGC205	wus7-MiniMeΔbox	A05979 + A05906; A05907 + A02230	pGGC203	pGGC000	XL1 Blue MR; 06.06.2016
pGGC214	petunia WUS	A06023 + A06024	pTL028	pGGC000	XL1 Blue MR; 03.08.2016
pGGC215	snapdragon WUS	A06073 + A06074	pTL029	pGGC000	XL1 Blue MR; 03.08.2016
pGGC216	tomato WUS	A06071 + A06072	pTL030	pGGC000	XL1 Blue MR; 03.08.2016
pGGC217	MPB2C	A06061 + A06062; A06063 + A06064	plasmid from Fritz Kraglers lab	pGGC000	XL1 Blue MR; 04.08.2016
pGGC219	WUSΔboxSNP1 (mutation at bp 316)	A05916 + A06144; A06116 + A02230	pGGC181	pGGC000	XL1 Blue MR; 20.09.2016
pGGC220	WUSΔboxSNP2 (mutation at bp 355)	A05916 + A06114; A06060 + A02230	pGGC181	pGGC000	XL1 Blue MR; 20.09.2016
pGGC221	WUSΔboxSNP3 (mutation at bp 717)	A05916 + A06013; A05878 + A02230	pGGC181	pGGC000	XL1 Blue MR; 21.09.2016
pGGC222	petunia WUSΔbox	A06235 + A06023; A06236 + A06024	pGGC214	pGGC000	XL1 Blue MR; 07.10.2016
pGGC223	snapdragon WUSΔbox	A06237 + A06073; A06238 + A06074	pGGC215	pGGC000	XL1 Blue MR; 21.10.2016
pGGC224	tomato WUSΔbox	A06239 + A06071; A06240 + A06072	pGGC216	pGGC000	XL1 Blue MR; 07.10.2016
pGGC228	WUSΔboxΔEAR	A05916 + A06280	pGGB053	pGGC000	XL1 Blue MR; 02.12.2016
pGGC229	linker-mNeonGreen	A06289 + A06290	pGGD046	pGGC000	XL1 Blue MR; 02.12.2016
pGGC230	WOX13	A06284 + A06285	pGD049	pGGC000	XL1 Blue MR; 08.12.2016
pGGC251	N-C-MiniMeΔbox	A05916 + A06873; A06874 + A06875; A06876 + A02230	pGGC181; pGGC203; pGGC181	pGGC000	XL1 Blue MR; 03.11.2017
pGGC266	N-C-MiniMeHAM1Δbox (HAM1 binding domain reintroduced)	A05916 + A07036; A07037 + A07038; A07039 + A02230	pGGC251; pGGC181; pGGC251	pGGC000	XL1 Blue MR; 25.01.2018
pGGC285	N-C-MiniMe	A05916 + A07240; A07241 + A02230	pGGC251	pGGC000	XL1 Blue MR; 06.08.2018
pGGC286	N-C-MiniMeHAM1	A05916 + A07240; A07241 + A02230	pGGC266	pGGC000	XL1 Blue MR; 06.08.2018

Entry vector	Content	Oligos	Template	Backbone	E. coli glycerol stock
pGGC343	MiniMe C-term, WUS del1 (298-348bp replaced by GS-linker), Δbox	A05979 + A06873; A06874 + A02230	pGGC203; pGGC193	pGGC000	XL1 Blue MR; 25.03.2021
pGGC344	MiniMe C-term, WUS del2 (349-399bp replaced by GS-linker), Δbox	A05979 + A06873; A06874 + A02230	pGGC203; pGGC194	pGGC000	XL1 Blue MR; 13.01.2021
pGGC345	MiniMe C-term, WUS del3 (400-450bp replaced by GS-linker), Δbox	A05979 + A06873; A06874 + A02230	pGGC203; pGGC195	pGGC000	XL1 Blue MR; 13.01.2021
pGGC346	MiniMe C-term, WUS del4 (451-501bp replaced by GS-linker), Δbox	A05979 + A06873; A06874 + A02230	pGGC203; pGGC196	pGGC000	XL1 Blue MR; 03.05.2021
pGGC347	MiniMe C-term, WUS del5 (502-552bp replaced by GS-linker), Δbox	A05979 + A06873; A06874 + A02230	pGGC203; pGGC197	pGGC000	XL1 Blue MR; 25.03.2021
pGGC348	MiniMe C-term, WUS del6 (553-603bp replaced by GS-linker), Δbox	A05979 + A06873; A06874 + A02230	pGGC203; pGGC198	pGGC000	XL1 Blue MR; 13.01.2021
pGGC349	MiniMe C-term, WUS del7 (604-654bp replaced by GS-linker), Δbox	A05979 + A06873; A06874 + A02230	pGGC203; pGGC199	pGGC000	XL1 Blue MR; 25.03.2021
pGGC350	MiniMe C-term, WUS del8 (655-705bp replaced by GS-linker), Δbox	A05979 + A06873; A06874 + A02230	pGGC203; pGGC200	pGGC000	XL1 Blue MR; 13.01.2021
pGGC351	MiniMe C-term, WUS del9 (709-759bp replaced by GS-linker), Δbox	A05979 + A06873; A06874 + A02230	pGGC203; pGGC201	pGGC000	XL1 Blue MR; 13.01.2021
pGGD044	mNeonGreen	A05891 + A05892	pGGC107	pGGD000	XL1 Blue MR; 19.05.2016
pGGD045	linker-GFP (A206K)	A05917 + A05918; A05919 + A05920	pGGC014; pGGC087	pGGD000	XL1 Blue MR; 20.05.2016
pGGD046	linker-mNeonGreen	A05917 + A05918; A05919 + A05920	pGGD044; pGGD045	pGGD000	XL1 Blue MR; 06.06.2016
pGGD049	WUS 298-348 bp fragment	A06843 + A06844	-	pGGD000	XL1 Blue MR; 29.09.2017
pGGD050	WUS 400-450 bp fragment	A06845 + A06846	-	pGGD000	XL1 Blue MR; 29.09.2017
pGGD051	WUS 553-603 bp fragment	A06847 + A06848	-	pGGD000	XL1 Blue MR; 29.09.2017
pGGD052	WUS 604-654 bp fragment	A06849 + A06850	-	pGGD000	XL1 Blue MR; 29.09.2017
pGGD054	WUS non-conserved region (between HD and WUS box)	A06851 + A06852	pGGC181	pGGD000	XL1 Blue MR; 03.11.2017
pGGD056	HAM1 binding domain	A07034 + A07035	pGGC181	pGGD000	XL1 Blue MR; 23.01.2018
pGGS005	WUS + STOP codon	A05916 + A06255	pGGC180	pGGC000	XL1 Blue MR; 18.10.2016
pGGS006	WUSΔbox + STOP codon	A05916 + A06255	pGGC181	pGGC000	XL1 Blue MR; 18.10.2016
pGGS007	WUSΔboxΔEAR + STOP codon	A05916 + A06281	pGGS006	pGGC000	Sure; 12.12.2026
pGGS008	N-C-MiniMe + STOP codon	A05916 + A06255	pGGC285	pGGC000	XL1 Blue MR; 11.03.2019
pGGS009	N-C-MiniMe – HAM1 binding domain reintroduced + STOP codon	A05916 + A06255	pGGC286	pGGC000	XL1 Blue MR; 11.03.2019
pGGM010	pWUS :: B-dummy : XVE + STOP : D-dummy :: tWUS : FH-adaptor	-	pGGA003 pGGB003 pGGC124 pGGD017 pGGE002 pGGG001	pGGM00 0_puc19	XL1 Blue MR; 14.11.2016

## Appendix

Entry vector	Content	Oligos	Template	Backbone	E. coli glycerol stock
pGGM011	pML1 :: B-dummy : XVE + STOP : D-dummy :: tRBCS : FH-adaptor	-	pGGA022 pGGB003 pGGC124 pGGD017 pGGE001 pGGG001	pGGM000_puc19	XL1 Blue MR; 14.11.2016
pGGM012	pMIOX2 :: B-dummy : XVE + STOP : D-dummy :: tMIOX2 : FH-adaptor	-	pGGA052 pGGB003 pGGC124 pGGD017 pGGE026 pGGG001	pGGM000_puc19	XL1 Blue MR; 14.11.2016
pGGM013	pUBQ10 :: B-dummy : XVE + STOP : D-dummy :: tUBQ10 : FH-adaptor	-	pGGA006 pGGB003 pGGC124 pGGD017 pGGE009 pGGG001	pGGM000_puc19	XL1 Blue MR; 17.11.2016
pGGN014	HA-adaptor : pOlexTATA :: B-dummy : WUSΔbox : linker-mNeonGreen :: tHSP18.2-tUBQ5 : pUBQ10 :: HygR :: tOCS	-	pGGG002 pGGA044 pGGB003 pGGC181 pGGD046 pGGE015 pGGF005	pGGN000_puc19	XL1 Blue MR; 14.11.2016
pGGN015	HA-adaptor : pOlexTATA :: B-dummy : WUS : linker-mNeonGreen :: tHSP18.2-tUBQ5 : pUBQ10 :: HygR :: tOCS	-	pGGG002 pGGA044 pGGB003 pGGC180 pGGD046 pGGE015 pGGF005	pGGN000_puc19	XL1 Blue MR; 14.11.2016

## 6.3. List of destination vectors

The following table contains all destination vectors that were created for the WUS mobility project over the course of this thesis. Vectors were cloned as has been described above (see 4.2, following).

Destination vector	Content	Entry vectors used	Backbone	E. coli glycerol stock	Agrobacterium glycerol stock
pMF037	LB_pWUS :: B-dummy : WUS $\Delta$ box : linker-GFP :: tWUS_pUBQ10 :: HygR :: tOCS_RB	pGGA003 pGGB003 pGGC181 pGGD045 pGGE002 pGGF005	pGGZ001	01.07.2016	08.07.2016
pMF038	LB_pWUS :: B-dummy : WUS $\Delta$ box : linker-mNeonGreen :: tWUS_pUBQ10 :: HygR :: tOCS_RB	pGGA003 pGGB003 pGGC181 pGGD046 pGGE002 pGGF005	pGGZ001	21.06.2016	08.07.2016
pMF039	LB_pWUS :: B-dummy : wus-7 $\Delta$ box : linker-GFP :: tWUS_pUBQ10 :: HygR :: tOCS_RB	pGGA003 pGGB003 pGGC183 pGGD045 pGGE002 pGGF005	pGGZ001	01.07.2016	08.07.2016
pMF040	LB_pWUS :: B-dummy : wus-7 $\Delta$ box : linker-Neon :: tWUS_pUBQ10 :: HygR :: tOCS_RB	pGGA003 pGGB003 pGGC183 pGGD046 pGGE002 pGGF005	pGGZ001	01.07.2016	08.07.2016
pMF041	LB_pWUS :: B-dummy : WUS : linker-Neon :: tWUS_pUBQ10 :: HygR :: tOCS_RB	pGGA003 pGGB003 pGGC180 pGGD046 pGGE002 pGGF005	pGGZ001	07.07.2016	14.07.2016
pMF042	LB_pWUS :: NES : WUS $\Delta$ box : linker-mNeonGreen :: tWUS_pUBQ10 :: HygR :: tOCS_RB	pGGA003 pGGB056 pGGC181 pGGD046 pGGE002 pGGF005	pGGZ001	27.07.2016	12.08.2016
pMF043	LB_pUBQ10 :: NES : WUS $\Delta$ box : linker-mNeonGreen :: tRBCS_pUBQ10 :: HygR :: tOCS_RB	pGGA006 pGGB056 pGGC181 pGGD046 pGGE001 pGGF005	pGGZ001	27.07.2016	09.08.2016
pMF044	LB_pML1 :: NES : WUS $\Delta$ box : linker-mNeonGreen :: tRBCS_pUBQ10 :: HygR :: tOCS_RB	pGGA022 pGGB056 pGGC181 pGGD046 pGGE001 pGGF005	pGGZ001	27.07.2016	12.08.2016
pMF045	LB_pWUS :: B-dummy : WUS del1 (298-348bp replaced by GS-linker), $\Delta$ box : linker-mNeonGreen :: tWUS_pUBQ10 :: HygR :: tOCS_RB	pGGA003 pGGB003 pGGC193 pGGD046	pGGZ001	27.07.2016	12.08.2016

## Appendix

Destination vector	Content	Entry vectors used	Backbone	E. coli glycerol stock	Agrobacterium glycerol stock
		pGGE002 pGGF005			
pMF046	LB_pWUS :: B-dummy : WUS del2 (349-399bp replaced by GS-linker), Δbox : linker-mNeonGreen :: tWUS_pUBQ10 :: HygR :: tOCS_RB	pGGA003 pGGB003 pGGC194 pGGD046 pGGE002 pGGF005	pGGZ001	27.07.2016	12.08.2016
pMF047	LB_pWUS :: B-dummy : WUS del3 (400-450bp replaced by GS-linker), Δbox : linker-mNeonGreen :: tWUS_pUBQ10 :: HygR :: tOCS_RB	pGGA003 pGGB003 pGGC195 pGGD046 pGGE002 pGGF005	pGGZ001	27.07.2016	12.08.2016
pMF048	LB_pWUS :: B-dummy : WUS del4 (451-501bp replaced by GS-linker), Δbox : linker-mNeonGreen :: tWUS_pUBQ10 :: HygR :: tOCS_RB	pGGA003 pGGB003 pGGC196 pGGD046 pGGE002 pGGF005	pGGZ001	27.07.2016	12.08.2016
pMF049	LB_pWUS :: B-dummy : WUS del5 (502-552bp replaced by GS-linker), Δbox : linker-mNeonGreen :: tWUS_pUBQ10 :: HygR :: tOCS_RB	pGGA003 pGGB003 pGGC197 pGGD046 pGGE002 pGGF005	pGGZ001	27.07.2016	12.08.2016
pMF050	LB_pWUS :: B-dummy : WUS del6 (553-603bp replaced by GS-linker), Δbox : linker-mNeonGreen :: tWUS_pUBQ10 :: HygR :: tOCS_RB	pGGA003 pGGB003 pGGC198 pGGD046 pGGE002 pGGF005	pGGZ001	27.07.2016	12.08.2016
pMF051	LB_pWUS :: B-dummy : WUS del7 (604-654bp replaced by GS-linker), Δbox : linker-mNeonGreen :: tWUS_pUBQ10 :: HygR :: tOCS_RB	pGGA003 pGGB003 pGGC199 pGGD046 pGGE002 pGGF005	pGGZ001	27.07.2016	12.08.2016
pMF052	LB_pWUS :: B-dummy : WUS del8 (655-705bp replaced by GS-linker), Δbox : linker-mNeonGreen :: tWUS_pUBQ10 :: HygR :: tOCS_RB	pGGA003 pGGB003 pGGC200 pGGD046 pGGE002 pGGF005	pGGZ001	27.07.2016	12.08.2016
pMF053	LB_pWUS :: B-dummy : WUS del9 (709-759bp replaced by GS-linker), Δbox : linker-mNeonGreen :: tWUS_pUBQ10 :: HygR :: tOCS_RB	pGGA003 pGGB003 pGGC201 pGGD046 pGGE002 pGGF005	pGGZ001	27.07.2016	12.08.2016
pMF054	LB_pUBQ10 :: B-dummy : WUSΔbox : linker-mNeonGreen :: tRBCS_pUBQ10 :: HygR :: tOCS_RB	pGGA006 pGGB003 pGGC181 pGGD046 pGGE001 pGGF005	pGGZ001	28.07.2016	09.08.2016
pMF055	LB_pUBQ10 :: B-dummy : MiniMeΔbox : linker-mNeonGreen :: tRBCS_pUBQ10 :: HygR :: tOCS_RB	pGGA006 pGGB003 pGGC203 pGGD046 pGGE001 pGGF005	pGGZ001	28.07.2016	09.08.2016

Destination vector	Content	Entry vectors used	Backbone	E. coli glycerol stock	Agrobacterium glycerol stock
pMF056	LB_pML1 :: B-dummy : WUSΔbox : linker-mNeonGreen :: tRBCS_pUBQ10 :: HygR :: tOCS_RB	pGGA022 pGGB003 pGGC181 pGGD046 pGGE001 pGGF005	pGGZ001	28.07.2016	12.08.2016
pMF057	LB_pML1 :: B-dummy : MiniMeΔbox : linker-mNeonGreen :: tRBCS_pUBQ10 :: HygR :: tOCS_RB	pGGA022 pGGB003 pGGC203 pGGD046 pGGE001 pGGF005	pGGZ001	28.07.2016	12.08.2016
pMF058	LB_pWUS :: B-dummy : MiniMeΔbox : linker-mNeonGreen :: tWUS_pUBQ10 :: HygR :: tOCS_RB	pGGA003 pGGB003 pGGC203 pGGD046 pGGE002 pGGF005	pGGZ001	28.07.2016	12.08.2016
pMF059	LB_pWUS :: B-dummy : wus7MiniMeΔbox : linker-mNeonGreen :: tWUS_pUBQ10 :: HygR :: tOCS_RB	pGGA003 pGGB003 pGGC205 pGGD046 pGGE002 pGGF005	pGGZ001	28.07.2016	12.08.2016
pMF060	LB_pCLV3 :: B-dummy : MPB2C : D-dummy :: tCLV3_pUBQ10 :: HygR :: tOCS_RB	pGGA033 pGGB003 pGGC217 pGGD017 pGGE008 pGGF005	pGGZ001	11.08.2016	22.08.2016
pMF062	LB_pMIOX2 :: B-dummy : 3xmCherry : D-dummy :: tMIOX2_pUBQ10 :: HygR :: tOCS_RB	pGGA052 pGGB003 pGGC026 pGGD017 pGGE026 pGGF005	pGGZ001	16.09.2016	22.09.2016
pMF063	LB_pWUS :: B-dummy : Petunia WUS : linker-mNeonGreen :: tWUS_pUBQ10 :: HygR :: tOCS_RB	pGGA003 pGGB003 pGGC214 pGGD046 pGGE002 pGGF005	pGGZ001	20.09.2016	27.09.2016
pMF064	LB_pWUS :: B-dummy : Antirrhinum WUS : linker-mNeonGreen :: tWUS_pUBQ10 :: HygR :: tOCS_RB	pGGA003 pGGB003 pGGC215 pGGD046 pGGE002 pGGF005	pGGZ001	20.09.2016	27.09.2016
pMF065	LB_pWUS :: B-dummy : Solanum WUS : linker-mNeonGreen :: tWUS_pUBQ10 :: HygR :: tOCS_RB	pGGA003 pGGB003 pGGC216 pGGD046 pGGE002 pGGF005	pGGZ001	20.09.2016	27.09.2016
pMF068	LB_pWUS :: B-dummy : WUSΔbox-SNP1 : linker-mNeonGreen :: tWUS_pUBQ10 :: HygR :: tOCS_RB	pGGA003 pGGB003 pGGC219 pGGD046 pGGE002 pGGF005	pGGZ001	10.10.2016	02.11.2016
pMF069	LB_pWUS :: B-dummy : WUSΔbox-SNP2 : linker-mNeonGreen :: tWUS_pUBQ10 :: HygR :: tOCS_RB	pGGA003 pGGB003 pGGC220 pGGD046	pGGZ001	10.10.2016	02.11.2016

Appendix

Destination vector	Content	Entry vectors used	Backbone	E. coli glycerol stock	Agrobacterium glycerol stock
		pGGE002 pGGF005			
pMF070	LB_pWUS :: B-dummy : WUSΔbox-SNP3 : linker-mNeonGreen :: tWUS_pUBQ10 :: HygR :: tOCS_RB	pGGA003 pGGB003 pGGC221 pGGD046 pGGE002 pGGF005	pGGZ001	10.10.2016	02.11.2016
pMF074	LB_pWUS :: GFP : WUS+STOP : D-dummy :: tWUS_pUBQ10 :: HygR :: tOCS_RB	pGGA003 pGGB009 pGGS005 pGGD017 pGGE002 pGGF005	pGGZ001	14.11.2016	01.12.2016
pMF075	LB_pWUS :: B-dummy : WUS : GFP :: tWUS_pUBQ10 :: HygR :: tOCS_RB	pGGA003 pGGB003 pGGC180 pGGD011 pGGE002 pGGF005	pGGZ001	14.11.2016	01.12.2016
pMF076	LB_pWUS :: GFP-linker : WUS+STOP : D-dummy :: tWUS_pUBQ10 :: HygR :: tOCS_RB	pGGA003 pGGB061 pGGS005 pGGD017 pGGE002 pGGF005	pGGZ001	15.11.2016	01.12.2016
pMF077	LB_pWUS :: B-dummy : WUS : linker-GFP :: tWUS_pUBQ10 :: HygR :: tOCS_RB	pGGA003 pGGB003 pGGC180 pGGD045 pGGE002 pGGF005	pGGZ001	15.11.2016	01.12.2016
pMF078	LB_pWUS :: B-dummy : WUS+STOP : D-dummy :: tWUS_pUBQ10 :: HygR :: tOCS_RB	pGGA003 pGGB003 pGGS005 pGGD017 pGGE002 pGGF005	pGGZ001	14.11.2016	01.12.2016
pMF079	LB_pWUS :: mNeonGreen-linker : WUS+STOP : D-dummy :: tWUS_pUBQ10 :: HygR :: tOCS_RB	pGGA003 pGGB060 pGGS005 pGGD017 pGGE002 pGGF005	pGGZ001	14.11.2016	01.12.2016
pMF080	LB_pWUS :: mNeonGreen-linker : WUSΔbox+STOP : D-dummy :: tWUS_pUBQ10 :: HygR :: tOCS_RB	pGGA003 pGGB060 pGGS006 pGGD017 pGGE002 pGGF005	pGGZ001	14.11.2016	01.12.2016
pMF081	LB_pWUS :: B-dummy : XVE+STOP : D-dummy :: tWUS : FH-adaptor_HA-adaptor : pOlexTATA :: B-dummy : WUSΔbox : linker-mNeonGreen :: tHSP18.2-tUBQ5_pUBQ10 :: HygR :: tOCS_RB	pGGM010 pGGN014	pGGZ001	06.12.2016	04.01.2017
pMF082	LB_pWUS :: B-dummy : XVE+STOP : D-dummy :: tWUS : FH-adaptor_HA-adaptor : pOlexTATA :: B-dummy : WUS : linker-mNeonGreen :: tHSP18.2-tUBQ5_pUBQ10 :: HygR :: tOCS_RB	pGGM010 pGGN015	pGGZ001	06.12.2016	04.01.2017
pMF085	LB_pMIOX2 :: B-dummy : XVE+STOP : D-dummy :: tMIOX2 :	pGGM012 pGGN014	pGGZ001	06.12.2016	04.01.2017

Destination vector	Content	Entry vectors used	Backbone	E. coli glycerol stock	Agrobacterium glycerol stock
	FH-adaptor _ HA-adaptor : pOlexTATA :: B-dummy : WUSΔbox : linker-mNeonGreen :: tHSP18.2- tUBQ5 _ pUBQ10 :: HygR :: tOCS _ RB				
pMF086	LB _ pMIOX2 :: B-dummy : XVE+STOP : D-dummy :: tMIOX2 : FH-adaptor _ HA-adaptor : pOlexTATA :: B-dummy : WUS : linker-mNeonGreen :: tHSP18.2- tUBQ5 _ pUBQ10 :: HygR :: tOCS _ RB	pGGM012 pGGN015	pGGZ001	06.12.2016	04.01.2017
pMF087	LB _ pUBQ10 :: B-dummy : XVE+STOP : D-dummy :: tUBQ10 : FH-adaptor _ HA-adaptor : pOlexTATA :: B-dummy : WUS : linker-mNeonGreen :: tHSP18.2- tUBQ5 _ pUBQ10 :: HygR :: tOCS _ RB	pGGM013 pGGN015	pGGZ001	06.12.2016	04.01.2017
pMF089	LB _ pWUS :: B-dummy : WUSΔboxΔEAR : linker-GFP :: tWUS _ pUBQ10 :: HygR :: tOCS _ RB	pGGA003 pGGB003 pGGC228 pGGD045 pGGE002 pGGF005	pGGZ001	15.12.2016	04.01.2017
pMF090	LB _ pWUS :: B-dummy : WUSΔboxΔEAR : linker-mNeonGreen :: tWUS _ pUBQ10 :: HygR :: tOCS _ RB	pGGA003 pGGB003 pGGC228 pGGD046 pGGE002 pGGF005	pGGZ001	15.12.2016	04.01.2017
pMF091	LB _ pCLV3 :: omega element : BFP : linker-N7 NLS :: tCLV3 _ pUBQ10 :: HygR :: tOCS _ RB	pGGA033 pGGB002 pGGC024 pGGD007 pGGE008 pGGF005	pGGZ001	17.02.2017	06.03.2017
pMF092	LB _ pWUS :: B-dummy : WUSΔbox : linker-GFP :: tWUS _ pMAS :: BastaR :: tMAS _ RB	pGGA003 pGGB003 pGGC181 pGGD046 pGGE002 pGGF001	pGGZ001	17.02.2017	06.03.2017
pMF093	LB _ pWUS :: B-dummy : WUSΔbox : linker-mNeonGreen :: tWUS _ pMAS :: BastaR :: tMAS _ RB	pGGA003 pGGB003 pGGC181 pGGD045 pGGE002 pGGF001	pGGZ001	17.02.2017	06.03.2017
pMF094	LB _ pWUS :: B-dummy : WUSΔboxΔEAR : linker-GFP :: tWUS _ pMAS :: BastaR :: tMAS _ RB	pGGA003 pGGB003 pGGC228 pGGD046 pGGE002 pGGF001	pGGZ001	17.02.2017	06.03.2017
pMF095	LB _ pWUS :: B-dummy : WUSΔboxΔEAR : linker-mNeonGreen :: tWUS _ pMAS :: BastaR :: tMAS _ RB	pGGA003 pGGB003 pGGC228 pGGD045 pGGE002 pGGF001	pGGZ001	17.02.2017	06.03.2017
pMF096	LB _ pWUS :: B-dummy : petunia WUSΔbox : linker-mNeonGreen :: tWUS _ pMAS :: BastaR :: tMAS _ RB	pGGA003 pGGB003 pGGC222	pGGZ001	07.03.2017	27.04.2017

Appendix

Destination vector	Content	Entry vectors used	Backbone	E. coli glycerol stock	Agrobacterium glycerol stock
		pGGD046 pGGE002 pGGF001			
pMF097	LB_pWUS :: B-dummy : snapdragon WUSΔbox : linker-mNeonGreen :: tWUS_pMAS :: BastaR :: tMAS_RB	pGGA003 pGGB003 pGGC223 pGGD046 pGGE002 pGGF001	pGGZ001	07.03.2017	27.04.2017
pMF098	LB_pWUS :: B-dummy : tomato WUSΔbox : linker-mNeonGreen :: tWUS_pMAS :: BastaR :: tMAS_RB	pGGA003 pGGB003 pGGC224 pGGD046 pGGE002 pGGF001	pGGZ001	07.03.2017	27.04.2017
pMF099	LB_pWUS :: B-dummy : WUS del1 (298-348bp replaced by GS-linker), Δbox : linker-mNeonGreen :: tWUS_p MAS :: BastaR :: tMAS_RB	pGGA003 pGGB003 pGGC193 pGGD046 pGGE002 pGGF001	pGGZ001	07.03.2017	27.04.2017
pMF100	LB_pWUS :: B-dummy :: WUS del2 (349-399bp replaced by GS-linker), Δbox : linker-mNeonGreen :: tWUS_p MAS :: BastaR :: tMAS_RB	pGGA003 pGGB003 pGGC194 pGGD046 pGGE002 pGGF001	pGGZ001	07.03.2017	27.04.2017
pMF101	LB_pWUS :: B-dummy : WUS del3 (400-450bp replaced by GS-linker), Δbox : linker-mNeonGreen :: tWUS_p MAS :: BastaR :: tMAS_RB	pGGA003 pGGB003 pGGC195 pGGD046 pGGE002 pGGF001	pGGZ001	07.03.2017	27.04.2017
pMF102	LB_pWUS :: B-dummy : WUS del4 (451-501bp replaced by GS-linker), Δbox : linker-mNeonGreen :: tWUS_p MAS :: BastaR :: tMAS_RB	pGGA003 pGGB003 pGGC196 pGGD046 pGGE002 pGGF001	pGGZ001	07.03.2017	27.04.2017
pMF103	LB_pWUS :: B-dummy : WUS del5 (502-552bp replaced by GS-linker), Δbox : linker-mNeonGreen :: tWUS_p MAS :: BastaR :: tMAS_RB	pGGA003 pGGB003 pGGC197 pGGD046 pGGE002 pGGF001	pGGZ001	07.03.2017	27.04.2017
pMF104	LB_pWUS :: B-dummy : WUS del6 (553-603bp replaced by GS-linker), Δbox : linker-mNeonGreen :: tWUS : pMAS :: BastaR :: tMAS_RB	pGGA003 pGGB003 pGGC198 pGGD046 pGGE002 pGGF001	pGGZ001	07.03.2017	27.04.2017
pMF105	LB_pWUS :: B-dummy : WUS del7 (604-654bp replaced by GS-linker), Δbox : linker-mNeonGreen :: tWUS_p MAS :: BastaR :: tMAS_RB	pGGA003 pGGB003 pGGC199 pGGD046 pGGE002 pGGF001	pGGZ001	07.03.2017	27.04.2017
pMF106	LB_pWUS :: B-dummy : WUS del8 (655-705bp replaced by GS-linker), Δbox : linker-mNeonGreen :: tWUS_p MAS :: BastaR :: tMAS_RB	pGGA003 pGGB003 pGGC200 pGGD046 pGGE002 pGGF001	pGGZ001	07.03.2017	27.04.2017

Destination vector	Content	Entry vectors used	Backbone	E. coli glycerol stock	Agrobacterium glycerol stock
pMF107	LB_pWUS :: B-dummy : WUS del9 (709-759bp replaced by GS-linker), Δbox : linker-mNeonGreen :: tWUS_pMAS :: BastaR :: tMAS_RB	pGGA003 pGGB003 pGGC201 pGGD046 pGGE002 pGGF001	pGGZ001	07.03.2017	27.04.2017
pMF108	LB_pML1 :: B-dummy : GFP : D-dummy :: tRBCS_pMAS :: BastaR :: tMAS_RB	pGGA022 pGGB003 pGGC014 pGGD017 pGGE001 pGGF001	pGGZ001	11.05.2017	06.06.2017
pMF109	LB_pML1 :: B-dummy : mNeonGreen : D-dummy :: tRBCS_pMAS :: BastaR :: tMAS_RB	pGGA022 pGGB003 pGGC107 pGGD017 pGGE001 pGGF001	pGGZ001	18.05.2017	06.06.2017
pMF110	RB_pWUS :: B-dummy : WUS+STOP : D-dummy :: tWUS_pMAS :: BastaR :: tMAS_LB	pGGA003 pGGB003 pGGS005 pGGD017 pGGE002 pGGF001	pGGZ003	27.06.2017	06.07.2017
pMF111	RB_pWUS :: GFP : WUS+STOP : D-dummy :: tWUS_pMAS :: BastaR :: tMAS_LB	pGGA003 pGGB009 pGGS005 pGGD017 pGGE002 pGGF001	pGGZ003	27.06.2017	06.07.2017
pMF112	RB_pWUS :: B-dummy : WUS : GFP :: tWUS_pMAS :: BastaR :: tMAS_LB	pGGA003 pGGB003 pGGC180 pGGD011 pGGE002 pGGF001	pGGZ003	27.06.2017	06.07.2017
pMF113	RB_pWUS :: GFP-linker : WUS+STOP : D-dummy :: tWUS_pMAS :: BastaR :: tMAS_LB	pGGA003 pGGB061 pGGS005 pGGD017 pGGE002 pGGF001	pGGZ003	27.06.2017	06.07.2017
pMF114	RB_pWUS :: B-dummy : WUS : linker-GFP :: tWUS_pMAS :: BastaR :: tMAS_LB	pGGA003 pGGB003 pGGC180 pGGD045 pGGE002 pGGF001	pGGZ003	27.06.2017	06.07.2017
pMF115	RB_pWUS :: B-dummy : WUSΔboxSNP1 : linker-mNeonGreen :: tWUS_pMAS :: BastaR :: tMAS_LB	pGGA003 pGGB003 pGGC219 pGGD046 pGGE002 pGGF001	pGGZ003	07.07.2017	26.07.2017
pMF116	RB_pWUS :: B-dummy : WUSΔboxSNP2 : linker-mNeonGreen :: tWUS_pMAS :: BastaR :: tMAS_LB	pGGA003 pGGB003 pGGC220 pGGD046 pGGE002 pGGF001	pGGZ003	07.07.2017	26.07.2017
pMF117	RB_pWUS :: B-dummy : WUSΔboxSNP3 : linker-mNeonGreen :: tWUS_pMAS :: BastaR :: tMAS_LB	pGGA003 pGGB003 pGGC221 pGGD046	pGGZ003	07.07.2017	26.07.2017

## Appendix

Destination vector	Content	Entry vectors used	Backbone	E. coli glycerol stock	Agrobacterium glycerol stock
		pGGE002 pGGF001			
pMF118	RB_pMIOX2 :: B-dummy : WUSΔbox : linker-mNeonGreen :: tWUS_pMAS :: BastaR :: tMAS_LB	pGGA052 pGGB003 pGGC181 pGGD046 pGGE026 pGGF001	pGGZ003	07.07.2017	31.07.2017
pMF119	RB_pWUS :: B-dummy : WUSΔbox : linker-mNeonGreen :: tWUS_pMAS :: BastaR :: tMAS_LB	pGGA003 pGGB003 pGGC181 pGGD046 pGGE002 pGGF001	pGGZ003	22.09.2017	28.09.2017
pMF120	RB_pWUS :: B-dummy : WOX13 : linker-mNeonGreen :: tWUS_pMAS :: BastaR :: tMAS_LB	pGGA003 pGGB003 pGGC230 pGGD046 pGGE002 pGGF001	pGGZ003	22.09.2017	28.09.2017
pMF121	RB_pWUS :: B-dummy : MiniMeΔbox : linker-mNeonGreen :: tWUS_pMAS :: BastaR :: tMAS_LB	pGGA003 pGGB003 pGGC203 pGGD046 pGGE002 pGGF001	pGGZ003	22.09.2017	28.09.2017
pMF122	RB_pML1 :: B-dummy : WUSΔbox : linker-mNeonGreen :: tRBCS_pMAS :: BastaR :: tMAS_LB	pGGA022 pGGB003 pGGC181 pGGD046 pGGE001 pGGF001	pGGZ003	22.09.2017	28.09.2017
pMF123	RB_pML1 :: B-dummy : WOX13 : linker-mNeonGreen :: tRBCS_pMAS :: BastaR :: tMAS_LB	pGGA022 pGGB003 pGGC230 pGGD046 pGGE001 pGGF001	pGGZ003	22.09.2017	28.09.2017
pMF124	RB_pML1 :: B-dummy : MiniMeAbox : linker-mNeonGreen :: tRBCS_p MAS :: BastaR :: tMAS_LB	pGGA022 pGGB003 pGGC203 pGGD046 pGGE001 pGGF001	pGGZ003	22.09.2017	28.09.2017
pMF125	GG152: RB_pMIOX2::B- dummy:WOX13:linker- mNeonGreen::tMIOX2:pMAS:BastaR:: tMAS_LB	pGGA052 pGGB003 pGGC230 pGGD046 pGGE026 pGGF001	pGGZ003	22.09.2017	28.09.2017
pMF126	RB_pMIOX2 :: B-dummy : MiniMeΔbox : linker-mNeonGreen :: tMIOX2_pMAS :: BastaR :: tMAS_LB	pGGA052 pGGB003 pGGC203 pGGD046 pGGE026 pGGF001	pGGZ003	22.09.2017	28.09.2017
pMF127	RB_pWUS :: B-dummy : N-C- MiniMeΔbox : linker-mNeonGreen :: tWUS_pMAS :: BastaR :: tMAS_LB	pGGA003 pGGB003 pGGC251 pGGD046 pGGE002 pGGF001	pGGZ003	30.11.2017	20.12.2017
pMF128	RB_pML1 :: B-dummy : N-C- MiniMeΔbox : linker-mNeonGreen ::	pGGA022 pGGB003	pGGZ003	30.11.2017	20.12.2017

Destination vector	Content	Entry vectors used	Backbone	E. coli glycerol stock	Agrobacterium glycerol stock
	tRBCS_pMAS :: BastaR :: tMAS_LB	pGGC251 pGGD046 pGGE001 pGGF001			
pMF129	RB_pMIOX2 :: B-dummy : N-C-MiniMeΔbox : linker-mNeonGreen :: tMIOX2_pMAS :: BastaR :: tMAS_LB	pGGA052 pGGB003 pGGC251 pGGD046 pGGE026 pGGF001	pGGZ003	21.12.2017	22.1.2018
pMF130	RB_pWUS :: MiniMeΔbox : linker-mNeonGreen : del1 fragment :: tWUS_pMAS :: BastaR :: tMAS_LB	pGGA003 pGGB063 pGGC229 pGGD049 pGGE002 pGGF001	pGGZ003	04.12.2017	20.12.2017
pMF131	RB_pWUS :: MiniMeΔbox : linker-mNeonGreen : del3 fragment :: tWUS_pMAS :: BastaR :: tMAS_LB	pGGA003 pGGB063 pGGC229 pGGD050 pGGE002 pGGF001	pGGZ003	04.12.2017	20.12.2017
pMF132	RB_pWUS :: MiniMeΔbox : linker-mNeonGreen : non-conserved region :: tWUS_pMAS :: BastaR :: tMAS_LB	pGGA003 pGGB063 pGGC229 pGGD054 pGGE002 pGGF001	pGGZ003	04.12.2017	20.12.2017
pMF133	RB_pWUS :: N-C-MiniMeΔbox : linker-mNeonGreen : del1 fragment :: tWUS_pMAS :: BastaR :: tMAS_LB	pGGA003 pGGB065 pGGC229 pGGD049 pGGE002 pGGF001	pGGZ003	04.12.2017	20.12.2017
pMF134	RB_pWUS :: N-C-MiniMeΔbox : linker-mNeonGreen : del3 fragment :: tWUS_pMAS :: BastaR :: tMAS_LB	pGGA003 pGGB065 pGGC229 pGGD050 pGGE002 pGGF001	pGGZ003	04.12.2017	20.12.2017
pMF135	RB_pWUS :: N-C-MiniMeΔbox : linker-mNeonGreen : non-conserved region :: tWUS_pMAS :: BastaR :: tMAS_LB	pGGA003 pGGB065 pGGC229 pGGD054 pGGE002 pGGF001	pGGZ003	04.12.2017	20.12.2017
pMF136	RB_pWUS :: WOX13 : linker-mNeonGreen : del6 fragment :: tWUS_pMAS :: BastaR :: tMAS_LB	pGGA003 pGGB064 pGGC229 pGGD051 pGGE002 pGGF001	pGGZ003	04.12.2017	20.12.2017
pMF137	RB_pWUS :: WOX13 : linker-mNeonGreen : del7 fragment :: tWUS_pMAS :: BastaR :: tMAS_LB	pGGA003 pGGB064 pGGC229 pGGD052 pGGE002 pGGF001	pGGZ003	04.12.2017	20.12.2017
pMF138	RB_pWUS :: B-dummy : WUS : linker-mNeonGreen :: tWUS_pMAS :: BastaR :: tMAS_LB	pGGA003 pGGB003 pGGC180 pGGD046 pGGE002 pGGF001	pGGZ003	21.12.2017	16.01.2018

## Appendix

Destination vector	Content	Entry vectors used	Backbone	E. coli glycerol stock	Agrobacterium glycerol stock
pMF141	RB_pWUS :: B-dummy : N-C-MiniMeHAMΔbox : linker-mNeonGreen :: tWUS_pMAS :: BastaR :: tMAS_LB	pGGA003 pGGB003 pGGC266 pGGD046 pGGE002 pGGF001	pGGZ003	26.02.2018	02.03.2018
pMF142	RB_pML1 :: B-dummy : N-C-MiniMeHAMΔbox : linker-mNeonGreen :: tRBCS_pMAS :: BastaR :: tMAS_LB	pGGA022 pGGB003 pGGC266 pGGD046 pGGE001 pGGF001	pGGZ003	26.02.2018	02.03.2018
pMF143	RB_pMIOX2 :: B-dummy : N-C-MiniMeHAMΔbox : linker-mNeonGreen :: tMIOX2_pMAS :: BastaR :: tMAS_LB	pGGA052 pGGB003 pGGC266 pGGD046 pGGE026 pGGF001	pGGZ003	07.03.2018	13.03.2018
pMF144	RB_pWUS :: WOX13 : linker-mNeonGreen : HAM1 domain :: tWUS_pMAS :: BastaR :: tMAS_LB	pGGA003 pGGB064 pGGC229 pGGD056 pGGE002 pGGF001	pGGZ003	26.02.2018	02.03.2018
pMF145	RB_pWUS :: N-C-MiniMeAbox : linker-mNeonGreen : HAM1 domain :: tWUS_pMAS :: BastaR :: tMAS_LB	pGGA003 pGGB065 pGGC229 pGGD056 pGGE002 pGGF001	pGGZ003	26.02.2018	02.03.2018
pMF147	LB_pWUS :: B-dummy : WUS del1 (298-348bp replaced by GS-linker), Δbox : linker-mNeonGreen :: tWUS_pMAS :: BastaR :: tMAS_RB	pGGA003 pGGB003 pGGC193 pGGD046 pGGE002 pGGF001	pGGZ003	26.02.2018	02.03.2018
pMF148	LB_pWUS :: B-dummy :: WUS del2 (349-399bp replaced by GS-linker), Δbox : linker-mNeonGreen :: tWUS_pMAS :: BastaR :: tMAS_RB	pGGA003 pGGB003 pGGC194 pGGD046 pGGE002 pGGF001	pGGZ003	26.02.2018	02.03.2018
pMF149	LB_pWUS :: B-dummy : WUS del3 (400-450bp replaced by GS-linker), Δbox : linker-mNeonGreen :: tWUS_pMAS :: BastaR :: tMAS_RB	pGGA003 pGGB003 pGGC195 pGGD046 pGGE002 pGGF001	pGGZ003	26.02.2018	02.03.2018
pMF150	LB_pWUS :: B-dummy : WUS del4 (451-501bp replaced by GS-linker), Δbox : linker-mNeonGreen :: tWUS_pMAS :: BastaR :: tMAS_RB	pGGA003 pGGB003 pGGC196 pGGD046 pGGE002 pGGF001	pGGZ003	26.02.2018	02.03.2018
pMF151	LB_pWUS :: B-dummy : WUS del5 (502-552bp replaced by GS-linker), Δbox : linker-mNeonGreen :: tWUS_pMAS :: BastaR :: tMAS_RB	pGGA003 pGGB003 pGGC197 pGGD046 pGGE002 pGGF001	pGGZ003	26.02.2018	02.03.2018
pMF152	LB_pWUS :: B-dummy : WUS del6 (553-603bp replaced by GS-linker), Δbox : linker-mNeonGreen :: tWUS : pMAS :: BastaR :: tMAS_RB	pGGA003 pGGB003 pGGC198 pGGD046	pGGZ003	26.02.2018	02.03.2018

Destination vector	Content	Entry vectors used	Backbone	E. coli glycerol stock	Agrobacterium glycerol stock
		pGGE002 pGGF001			
pMF153	LB_pWUS :: B-dummy : WUS del7 (604-654bp replaced by GS-linker), Δbox : linker-mNeonGreen :: tWUS_pMAS :: BastaR :: tMAS_RB	pGGA003 pGGB003 pGGC199 pGGD046 pGGE002 pGGF001	pGGZ003	26.02.2018	02.03.2018
pMF154	LB_pWUS :: B-dummy : WUS del8 (655-705bp replaced by GS-linker), Δbox : linker-mNeonGreen :: tWUS_pMAS :: BastaR :: tMAS_RB	pGGA003 pGGB003 pGGC200 pGGD046 pGGE002 pGGF001	pGGZ003	26.02.2018	02.03.2018
pMF155	LB_pWUS :: B-dummy : WUS del9 (709-759bp replaced by GS-linker), Δbox : linker-mNeonGreen :: tWUS_pMAS :: BastaR :: tMAS_RB	pGGA003 pGGB003 pGGC201 pGGD046 pGGE002 pGGF001	pGGZ003	26.02.2018	02.03.2018
pMF156	RB_pWUS :: MiniMeΔbox : linker-mNeonGreen : HAM1 domain :: tWUS_pMAS :: BastaR :: tMAS_LB	pGGA003 pGGB063 pGGC229 pGGD056 pGGE002 pGGF001	pGGZ003	26.02.2018	02.03.2018
pMF157	RB_pWUS :: B-dummy : N-C-MiniMe : linker-GFP :: tWUS_pMAS :: BastaR :: tMAS_LB	pGGA003 pGGB003 pGGC285 pGGD045 pGGE002 pGGF001	pGGZ003	24.08.2018	24.10.2018
pMF158	RB_pWUS :: B-dummy : N-C-MiniMe : linker-mNeonGreen :: tWUS_pMAS :: BastaR :: tMAS_LB	pGGA003 pGGB003 pGGC285 pGGD046 pGGE002 pGGF001	pGGZ003	24.08.2018	24.10.2018
pMF159	RB_pWUS :: B-dummy : N-C-MiniMeHAM : linker-GFP :: tWUS_pMAS :: BastaR :: tMAS_LB	pGGA003 pGGB003 pGGC286 pGGD045 pGGE002 pGGF001	pGGZ003	24.08.2018	24.10.2018
pMF160	RB_pWUS :: B-dummy : N-C-MiniMeHAM : linker-mNeonGreen :: tWUS_pMAS :: BastaR :: tMAS_LB	pGGA003 pGGB003 pGGC286 pGGD046 pGGE002 pGGF001	pGGZ003	24.08.2018	24.10.2018
pMF161	RB_pWUS :: B-dummy : N-C-MiniMeΔbox : linker-GFP :: tWUS_pMAS :: BastaR :: tMAS_LB	pGGA003 pGGB003 pGGC251 pGGD045 pGGE002 pGGF001	pGGZ003	24.08.2018	24.10.2018
pMF162	RB_pML1 :: B-dummy : N-C-MiniMeΔbox : linker-GFP :: tRBCS_pMAS :: BastaR :: tMAS_LB	pGGA022 pGGB003 pGGC251 pGGD045 pGGE001 pGGF001	pGGZ003	24.08.2018	24.10.2018
pMF163	RB_pWUS :: B-dummy : XVE+STOP : D-dummy :: tWUS : FH-adaptor _	pGGM010 pGGG002	pGGZ003	02.09.2019	13.09.2019

## Appendix

Destination vector	Content	Entry vectors used	Backbone	E. coli glycerol stock	Agrobacterium glycerol stock
	HA-adaptor : pOlexTATA :: B-dummy : WUSΔbox : linker-mNeonGreen :: tHSP18.2-tUBQ5_pMAS :: BastaR :: tMAS_LB	pGGA044 pGGB003 pGGC181 pGGD046 pGGE015 pGGF001			
pMF164	RB_pWUS :: B-dummy : XVE+STOP : D-dummy :: tWUS : FH-adaptor_ HA-adaptor : pOlexTATA :: B-dummy : WUSΔbox : linker-GFP :: tHSP18.2-tUBQ5_pMAS :: BastaR :: tMAS_LB	pGGM010 pGGG002 pGGA044 pGGB003 pGGC181 pGGD045 pGGE015 pGGF001	pGGZ003	02.09.2019	13.09.2019
pMF165	RB_pWUS :: B-dummy : XVE+STOP : D-dummy :: tWUS : FH-adaptor_ HA-adaptor : pOlexTATA :: B-dummy : WUS : linker-mNeonGreen :: tHSP18.2-tUBQ5_pMAS :: BastaR :: tMAS_LB	pGGM010 pGGG002 pGGA044 pGGB003 pGGC180 pGGD046 pGGE015 pGGF001	pGGZ003	02.09.2019	13.09.2019
pMF166	RB_pWUS :: B-dummy : XVE+STOP : D-dummy :: tWUS : FH-adaptor_ HA-adaptor : pOlexTATA :: B-dummy : WUS : linker-GFP :: tHSP18.2-tUBQ5_pMAS :: BastaR :: tMAS_LB	pGGM010 pGGG002 pGGA044 pGGB003 pGGC180 pGGD045 pGGE015 pGGF001	pGGZ003	02.09.2019	13.09.2019
pMF167	RB_pWUS :: NES : WUSΔbox : linker-mNeonGreen :: tWUS_pMAS :: BastaR :: tMAS_LB	pGGA003 pGGB056 pGGC181 pGGD046 pGGE002 pGGF001	pGGZ003	02.09.2019	13.09.2019
pMF168	RB_pWUS :: NLS-linker : WUSΔbox : linker-mNeonGreen :: tRBCS_pMAS :: BastaR :: tMAS_LB	pGGA003 pGGB022 pGGC181 pGGD046 pGGE002 pGGF001	pGGZ003	02.09.2019	13.09.2019
pMF169	RB_pML1 :: NES : WUSΔbox : linker-mNeonGreen :: tRBCS_pMAS :: BastaR :: tMAS_LB	pGGA022 pGGB056 pGGC181 pGGD046 pGGE001 pGGF001	pGGZ003	02.09.2019	13.09.2019
pMF170	RB_pWUS :: B-dummy : WUSΔbox : linker-GFP :: tWUS_pMAS :: BastaR :: tMAS_LB	pGGA003 pGGB003 pGGC181 pGGD045 pGGE002 pGGF001	pGGZ003	02.09.2019	13.09.2019
pMF171	RB_pWUS :: B-dummy : GFP : linker-GFP :: tWUS_pMAS :: BastaR :: tMAS_LB	pGGA003 pGGB003 pGGC014 pGGD045 pGGE002 pGGF001	pGGZ003	02.09.2019	13.09.2019
pMF172	RB_pWUS :: GFP-linker : GFP : linker-N7 NLS :: tWUS_pMAS :: BastaR :: tMAS_LB	pGGA003 pGGB061 pGGC014 pGGD007	pGGZ003	02.09.2019	13.09.2019

Destination vector	Content	Entry vectors used	Backbone	E. coli glycerol stock	Agrobacterium glycerol stock
		pGGE002 pGGF001			
pMF173	RB_pML1 :: B-dummy : WUSΔbox : linker-GFP :: tRBCS_pMAS :: BastaR :: tMAS_LB	pGGA022 pGGB003 pGGC181 pGGD045 pGGE001 pGGF001	pGGZ003	02.09.2019	13.09.2019
pMF174	RB_pML1 :: B-dummy : GFP : linker-GFP :: tRBCS_pMAS :: BastaR :: tMAS_LB	pGGA022 pGGB003 pGGC014 pGGD045 pGGE001 pGGF001	pGGZ003	02.09.2019	13.09.2019
pMF175	RB_pML1 :: GFP-linker : GFP : linker-N7 NLS :: tRBCS_pMAS :: BastaR :: tMAS_LB	pGGA022 pGGB061 pGGC014 pGGD007 pGGE001 pGGF001	pGGZ003	02.09.2019	13.09.2019
pMF176	RB_pML1 :: NLS-linker : WUSΔbox : linker-mNeonGreen :: tRBCS_pMAS :: BastaR :: tMAS_LB	pGGA022 pGGB022 pGGC181 pGGD046 pGGE001 pGGF001	pGGZ003	04.09.2019	13.09.2019
pMF177	RB_pWUS :: B-dummy : MiniMe : linker-GFP :: tWUS_pMAS :: BastaR :: tMAS_LB	pGGA003 pGGB003 pGGC202 pGGD045 pGGE002 pGGF001	pGGZ003	27.09.2019	09.10.2019
pMF178	RB_pML1 :: B-dummy : WUSΔbox : linker-fastFT :: tRBCS_pMAS :: BastaR :: tMAS_LB	pGGA022 pGGB003 pGGC181 pGGD065 pGGE001 pGGF001	pGGZ003	27.09.2019	13.09.2019
pMF179	RB_pML1 :: B-dummy : MiniMeΔbox : linker-fastFT :: tRBCS_pMAS :: BastaR :: tMAS_LB	pGGA022 pGGB003 pGGC203 pGGD065 pGGE001 pGGF001	pGGZ003	27.09.2019	13.09.2019
pMF180	RB_pWUS :: B-dummy : WUS : linker-fastFT :: tWUS_pMAS :: BastaR :: tMAS_LB	pGGA003 pGGB003 pGGC180 pGGD065 pGGE002 pGGF001	pGGZ003	27.09.2019	13.09.2019
pMF181	RB_pWUS :: B-dummy : WUSΔbox : linker-fastFT :: tWUS_pMAS :: BastaR :: tMAS_LB	pGGA003 pGGB003 pGGC181 pGGD065 pGGE002 pGGF001	pGGZ003	27.09.2019	13.09.2019
pMF182	RB_pWUS :: B-dummy : MiniMeΔbox : linker-fastFT :: tWUS_pMAS :: BastaR :: tMAS_LB	pGGA003 pGGB003 pGGC203 pGGD065 pGGE002 pGGF001	pGGZ003	27.09.2019	13.09.2019

## Appendix

Destination vector	Content	Entry vectors used	Backbone	E. coli glycerol stock	Agrobacterium glycerol stock
pMF183	RB_pWUS :: B-dummy : WOX13 : linker-GFP :: tWUS_pMAS :: BastaR :: tMAS_LB	pGGA003 pGGB003 pGGC230 pGGD045 pGGE002 pGGF001	pGGZ003	27.09.2019	13.09.2019
pMF238	RB_pWUS :: B-dummy : MiniMe C-term, WUS del1 (298-348bp replaced by GS-linker), Δbox : linker-GFP :: tWUS_pMAS :: BastaR :: tMAS_LB	pGGA003 pGGB003 pGGC343 pGGD045 pGGE002 pGGF001	pGGZ003	08.07.2021	08.07.2021
pMF239	RB_pWUS :: B-dummy : MiniMe C-term, WUS del2 (349-399bp replaced by GS-linker), Δbox : linker-GFP :: tWUS_pMAS :: BastaR :: tMAS_LB	pGGA003 pGGB003 pGGC344 pGGD045 pGGE002 pGGF001	pGGZ003	08.07.2021	08.07.2021
pMF240	RB_pWUS :: B-dummy : MiniMe C-term, WUS del3 (400-450bp replaced by GS-linker), Δbox : linker-GFP :: tWUS_pMAS :: BastaR :: tMAS_LB	pGGA003 pGGB003 pGGC345 pGGD045 pGGE002 pGGF001	pGGZ003	08.07.2021	08.07.2021
pMF241	RB_pWUS :: B-dummy : MiniMe C-term, WUS del4 (451-501bp replaced by GS-linker), Δbox : linker-GFP :: tWUS_pMAS :: BastaR :: tMAS_LB	pGGA003 pGGB003 pGGC346 pGGD045 pGGE002 pGGF001	pGGZ003	08.07.2021	08.07.2021
pMF242	RB_pWUS :: B-dummy : MiniMe C-term, WUS del5 (502-552bp replaced by GS-linker), Δbox : linker-GFP :: tWUS_pMAS :: BastaR :: tMAS_LB	pGGA003 pGGB003 pGGC347 pGGD045 pGGE002 pGGF001	pGGZ003	08.07.2021	08.07.2021
pMF243	RB_pWUS :: B-dummy : MiniMe C-term, WUS del6 (553-603bp replaced by GS-linker), Δbox : linker-GFP :: tWUS_pMAS :: BastaR :: tMAS_LB	pGGA003 pGGB003 pGGC348 pGGD045 pGGE002 pGGF001	pGGZ003	08.07.2021	08.07.2021
pMF244	RB_pWUS :: B-dummy : MiniMe C-term, WUS del7 (604-654bp replaced by GS-linker), Δbox : linker-GFP :: tWUS_pMAS :: BastaR :: tMAS_LB	pGGA003 pGGB003 pGGC349 pGGD045 pGGE002 pGGF001	pGGZ003	08.07.2021	08.07.2021
pMF245	RB_pWUS :: B-dummy : MiniMe C-term, WUS del8 (655-705bp replaced by GS-linker), Δbox : linker-GFP :: tWUS_pMAS :: BastaR :: tMAS_LB	pGGA003 pGGB003 pGGC350 pGGD045 pGGE002 pGGF001	pGGZ003	08.07.2021	08.07.2021
pMF246	RB_pWUS :: B-dummy : MiniMe C-term, WUS del9 (709-759bp replaced by GS-linker), Δbox : linker-GFP :: tWUS_pMAS :: BastaR :: tMAS_LB	pGGA003 pGGB003 pGGC351 pGGD045 pGGE002 pGGF001	pGGZ003	08.07.2021	08.07.2021
pMF247	RB_pWUS :: NES : GFP : linker-GFP :: tWUS_pMAS :: BastaR :: tMAS_LB	pGGA003 pGGB056 pGGC014 pGGD045	pGGZ003	08.07.2021	08.07.2021

Destination vector	Content	Entry vectors used	Backbone	E. coli glycerol stock	Agrobacterium glycerol stock
		pGGE002 pGGF001			
pMF248	RB_pML1 :: NES : GFP : linker-GFP :: tRBCS_pMAS :: BastaR :: tMAS_ LB	pGGA022 pGGB056 pGGC014 pGGD045 pGGE001 pGGF001	pGGZ003	08.07.2021	08.07.2021
pMF249	RB_pWUS :: N7 NLS-linker : GFP : linker-GFP :: tWUS_pMAS :: BastaR :: tMAS_LB	pGGA003 pGGB022 pGGC014 pGGD045 pGGE002 pGGF001	pGGZ003	08.07.2021	08.07.2021
pMF250	RB_pML1 :: N7 NLS-linker : GFP : linker-GFP :: tWUS_pMAS :: BastaR :: tRBCS_LB	pGGA022 pGGB022 pGGC014 pGGD045 pGGE001 pGGF001	pGGZ003	08.07.2021	08.07.2021